Lawrence Berkeley National Laboratory
Recent Work

Title

Sum frequency generation (SFG) surface vibrational spectroscopy and atomic force microscopy (AFM) studies of the composition, structure, and mechanical behavior of polymers at interfaces

Permalink

Author

Opdahl, Aric M.

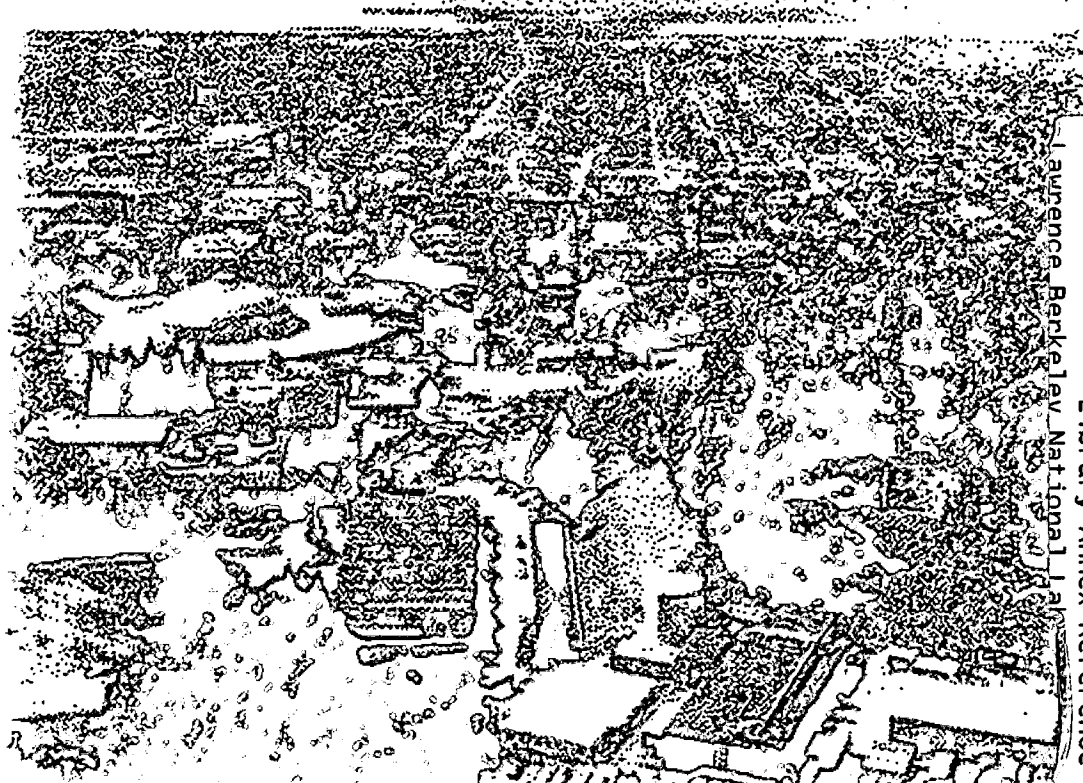**Publication Date**

2003-05-23

ERNEST ORLANDO LAWRENCE BERKELEY NATIONAL LABORATORY

Sum Frequency Generation (SFG) Surface Vibrational Spectroscopy and Atomic Force Microscopy (AFM) Studies of the Composition, Structure, and Mechanical Behavior of Polymers at Interfaces

Aric M. Opdahl

Materials Sciences Division

May 2003

Ph.D. Thesis

DISCLAIMER

Sum Frequency Generation (SFG) Surface Vibrational Spectroscopy and Atomic Force Microscopy (AFM) Studies of the Composition, Structure, and Mechanical Behavior of Polymers at Interfaces

Aric Martin Opdahl
Ph.D. Thesis

Department of Chemistry
University of California, Berkeley

and

Materials Sciences Division
Ernest Orlando Lawrence Berkeley National Laboratory
University of California
Berkeley, CA 94720

May 2003

Sum Frequency Generation (SFG) Surface Vibrational Spectroscopy and Atomic Force Microscopy (AFM) Studies of the Composition, Structure, and Mechanical Behavior of Polymers at Interfaces

Copyright © 2003

by

Aric Martin Opdahl

Sum frequency generation (SFG) surface vibrational spectroscopy and atomic force microscopy (AFM) studies of the composition, structure, and mechanical behavior of polymers at interfaces

by

Aric Martin Opdahl

B.S. (University of Wisconsin at Madison) 1996

A dissertation submitted in partial satisfaction of the

requirements for the degree of

Doctor of Philosophy

in

Chemistry

in the

GRADUATE DIVISION

of the

UNIVERSITY OF CALIFORNIA, BERKELEY

Committee in charge:

Professor Gabor A. Somorjai (Chair)
Professor Herbert L. Strauss
Professor Lisa A. Pruitt

Spring 2003

Abstract

Sum frequency generation (SFG) surface vibrational spectroscopy and

atomic force microscopy (AFM) studies of the composition, structure, and

mechanical behavior of polymers at interfaces

by

Aric Martin Opdahl

Doctor of Philosophy in Chemistry

University of California, Berkeley

Professor Gabor A. Somorjai (Chair)

Sum frequency generation (SFG) surface vibrational spectroscopy, x-ray

photoelectron spectroscopy (XPS), and atomic force microscopy (AFM) were used to

obtain experimental measurements of polymer surface composition, surface structure,

and surface mechanical behavior. The experiments described in this dissertation focus on

answering three questions: (1) How are polymers configured at interfaces? (2) How do

changes in environment (air vs. liquid vs. solid) affect polymer interface properties? (3)

How does the mechanical environment (i.e. stretching) affect the interface composition

and mechanical behavior of polymers?

It is well established that most polymers assume preferred configurations at

interfaces. At the polymer/air interface, the configuration and ordering of short methyl

side branches was quantified by analyzing SFG spectra obtained from a series of

aspecific poly(ethylene-co-propylene) copolymers (*a*EPR) with varying ethylene content.

Side branch ordering was also characterized at polymer/liquid interfaces. Immiscible

polymer and liquid pairs were shown to form ordered interfaces. In contrast, solvents were shown to disorder polymer/liquid interfaces.

The surface morphologies of polyolefin blends were characterized. In blends of atactic polypropylene (*a*PP) and *a*EPR, it was observed that *a*PP, the polymer with lower surface tension, was enriched at the polymer/air interface. The thickness of the *a*PP surface enrichment layer was shown to depend on the energy of mixing of the two components, with thicker enrichment layers measured from bulk immiscible blends. Similar results were obtained using isotactic polypropylene (*i*PP)/*a*EPR blends. It was found that the surface segregation tendencies of the *i*PP/*a*EPR blend could be reversed by exposing the blend to n-hexane vapor, which preferentially solvated *a*EPR component.

Changes in surface composition, texture, and mechanical behavior of polymers were characterized as a function of tensile elongation. The surfaces of low and high density polyethylene, which have spherulitic microstructures, were found to systematically roughen as the surface microstructure evolved into a fiber morphology. For a phase-separated polystyrene(butadiene)styrene triblock copolymer, at low tensile stress the more flexible component absorbs most of the strain in the bulk. The surface was shown to deform inhomogeneously as the polymer is elongated.

Finally, a method was developed, using AFM, to probe the surface mechanical properties of hydrogel materials, used as contact lenses. The surface mechanical properties of methacrylate hydrogels were shown to be highly dependent on hydration. It was found that the region near the hydrogel/air interface is significantly stiffer than the bulk, indicating the interface region is dehydrated, relative to the level of bulk hydration.

Table of Contents

Chapter 7: AFM measurement of the surface deformation and surface elastic properties of stretched polyethylene

Chapter 8: Surface deformation of a triblock poly(styrene-butadiene-styrene) copolymer as it is stretched

Chapter 9: Mechanical properties of contact lens surfaces exposed to controlled humidity

Acknowledgements

I have enjoyed my time as a graduate student at Berkeley. Many people have contributed to my growth during this period and have helped me to establish a foundation for a career in science. I acknowledge Professor Somorjai as the primary contributor to this foundation. I thank him for his encouragement and support, and for providing a stimulating and productive research environment.

In the Somorjai Group, two people, Steve Baldelli and Seong Kim, were more influential than most and deserve special mention. Steve and Seong joined the group as postdocs around the same time I began graduate school, and were excellent role models as I was learning how to succeed at experimental research. I would like to acknowledge others in the group that I had the opportunity to work with directly - David Gracias, Zhan Chen, Ella Amitay Sadovsky, Telly Koffas, Jamie Kim, and Sasha Kweskin, and also those I worked with indirectly including Keith McCrea, Saskia Hoffer, and Keng Chou. I would also like to thank the administrative staff – especially Inger Coble.

A portion of my research time was spent on collaborative projects with Basell Polyolefins and Ocular Sciences. These collaborations were an important part of shaping my perspective. In particular, I enjoyed working with Dr. Roger Phillips (Basell) and acknowledge contributions from him in Chapters 4, 5, and 6. I also acknowledge contributions from Dr. Chris Marmo (Ocular Sciences) in Chapter 9.

I would like to thank family and friends for the encouragement I have received during this process. My parents have always been supportive of me and of the choices I've made on my career path. I'd also like to thank Bryce Nelson for the encouragement

iv

Introduction

This experiments presented in this dissertation are focused on measurement of the interface properties of polymers, in particular on answering three questions: (1) How are polymers configured at interfaces? (2) How do changes in environment (in this case air vs. liquid vs. solid) affect polymer interface properties? (3) How does the mechanical environment (i.e. stretching) affect the interface composition and mechanical behavior of polymers? The physical properties of polymer interfaces, including adhesion, wettability, and friction, are influenced by the chemical composition and microstructure of the interfacial region. Under equilibrium conditions, polymer chains, like liquid molecules, will typically adapt preferred conformations at an interface. Polymer mixtures will typically be enriched in the component that lowers the overall surface energy of the system. As a practical matter, however, equilibrium is usually not attained, since many polymer systems contain a crystalline component, a glassy component, or are highly crosslinked. The interface region can easily be trapped in a state that is not equilibrated.

A specific example, treated in Chapter 6, focuses on the surface morphology of a high-impact polyolefin blend, a material used in automobile bumpers. The blend contains an isospecific polypropylene component, which is crystalline and contributes shape and

hardness to the material, and a rubbery amorphous material, which absorbs the stress from an impact. A major practical problem is that isospecific polypropylene requires pretreatment before paint will adhere to its surface. The paintability can be improved in blends containing an amorphous polymer, presumably due to a high concentration of the permeable amorphous polymer in the surface region. The degree to which paintability is improved varies depending on the specific blend components. Thus it is important to understand how compositional variables influence the blend surface morphology, and to connect that information to the paintability of the surface.

The mechanical environment can also affect a polymer surface morphology. Most polymers can be deformed/stretched to some extent. Stretching, discussed in Chapters 7 and 8, has the effect of increasing the surface to volume ratio of a polymer. Macroscopically, the dimensions of an initially flat polymer surface change as a result of stretching – the surface becomes longer and thinner. The macroscopic dimension changes of the surface can affect the microscopic and molecular organization of polymers at the surface. For multi-component polymers, changes in surface area/shape can potentially lead to changes in the surface composition, based on differences in mechanical properties of the individual components.

A final example, discussed in Chapter 9, focuses on the surface properties of cross-linked methacrylate hydrogels, used as contact lenses. It is generally believed that the useful lifetime and comfort of a contact lens hydrogel surface is directly related to high wettability and resistance to biofouling. To understand wettability, it is important to understand how the surface water content and the surface chemical composition are

affected by the bulk chemical composition of the hydrogel and by environmental variables such as changes in humidity.

A combination of three experimental techniques was used to probe the morphology and mechanical behavior of polymer surfaces: sum frequency generation (SFG) surface vibrational spectroscopy, x-ray photoelectron spectroscopy (XPS), and atomic force microscopy (AFM). The combination of these three experimental techniques can provide a robust description of the interface morphology. SFG vibrational spectroscopy is an optical technique that can be highly sensitive to the chemical composition, orientation, and ordering of molecular groups at interfaces. SFG experiments can be monolayer specific and can be designed to probe the structure of nearly any interface that is accessible by light. This makes SFG useful for *in situ* studies of phenomenon including adhesion and wetting, where the orientation of the molecular groups at the interface may play a critical role. XPS, based on the detection of photoelectrons, is sensitive to the composition of the 5-10nm of material nearest the polymer/vacuum interface. AFM can be used to probe lateral surface morphology and is sensitive to changes in mechanical properties of the surface.

Specifically, Chapter 1 is an introduction to SFG surface vibrational spectroscopy and AFM. Several examples of SFG spectra obtained from polymer/air interfaces are presented. At air interfaces, polymers configure themselves in a manner that lowers the total surface energy. In homopolymers, surface ordering of the structural component, backbone or side branch, with the lowest surface energy is observed. SFG spectra obtained from polymers with multiple bulky side branches per monomer repeat unit, like poly(alpha-methyl)styrene, suggest side branch ordering is sterically limited. The basic

principles of AFM and AFM imaging are discussed. A description of the AFM force vs. distance curve, which can be used to measure surface stiffness, viscoelasticity, and adhesion is also presented.

Chapter 2 presents results of an experiment designed to quantify side branch ordering at polymer/air interfaces. The relationship between the bulk number density of side branches and the number density of side branches ordered at the polymer/air interface is quantified using a series of random aspecific poly(ethylene-co-propylene) rubber copolymers (aEPR). All of the copolymers are found to preferentially orient side-branch methyl groups out of the surface. As the ethylene content of the copolymer increases, the number of methyl groups contributing to the sum frequency signal decreases. However, the percentage of methyl groups oriented out of the surface, relative to the bulk concentration of methyl groups, increases. This surface excess of oriented methyl groups is proposed to be a result of decreased steric hindrances between adjacent methyl groups in ethylene-rich copolymers.

Chapters 3 and 4 focus on the structure of polymer/liquid interfaces. In Chapter 3 SFG vibrational spectroscopy has been used to characterize the effect that toluene solvent vapor has on the surface structure of polystyrene films. SFG spectra show that low surface tension toluene molecules preferentially coat the surfaces of polystyrene films that are exposed to a saturated toluene vapor environment. The SFG spectra indicate that polystyrene phenyl side branches are well-ordered at the air/polystyrene interface prior to toluene exposure, and that the polystyrene/toluene interface is highly disordered. After exposure, as the toluene evaporates from the film, the partially solvated polystyrene surface rapidly reorders the phenyl side groups at the air/polystyrene interface.

The molecular structure of the interface between atactic polypropylene (*a*PP) and polar liquids and vapors, determined by SFG, is presented in Chapter 4. SFG spectra show that ordered interfaces are formed between *a*PP films and water, methanol, and acetonitrile. The interface structure of *a*PP in contact with methanol and acetonitrile is indistinguishable from the structure of the *a*PP/air interface. Interference effects in the SFG spectra suggest that the methyl ends of the acetonitrile and methanol molecules order at the *a*PP interface, and are oriented towards the methyl side branches of *a*PP. The *a*PP surface restructures when it is in contact with water. The *a*PP methyl side branches disorder or orient away from the liquid phase, presumably to minimize the interaction between the nonpolar side branches and water.

Chapter 5 discusses the composition of polyolefin mixtures at air interfaces. Surface composition profiles of bulk miscible and immiscible blends of atactic polypropylene (*a*PP) with aspecific poly(ethylene-co-propylene) rubber (*a*EPR) were studied by differential scanning calorimetry (DSC), sum frequency generation surface vibrational spectroscopy (SFG), and x-ray photoelectron spectroscopy (XPS). SFG spectra of blends of *a*PP and *a*EPR show that *a*PP preferentially segregates to the air/polymer interface, for both the bulk miscible and immiscible systems. Thicker enrichment layers were detected by XPS for bulk immiscible blends. The thickness of the surface enrichment layer measured in the bulk-miscible systems agrees with the thickness calculated using depth-profiling models based on Flory-Huggins energy of mixing.

Chapter 6 discusses the surface compositions and morphologies of melt-quenched blends of isotactic polypropylene (*i*PP) with aspecific poly(ethylene-co-propylene) rubber. This blend is a model for the industrial relevant isospecific PP/EPR blend used in

car bumpers. Surface morphologies and compositions formed in the melt are 'frozen-in' by crystallization of the iPP component and, depending on the processing conditions, are enriched in iPP, in aEPR, or contain a phase separated mix of iPP and aEPR. Enrichment of iPP is observed for blends melted in open air. Surface segregation of iPP is suppressed at confined interfaces. Blends melt-pressed between hydrophilic and between hydrophobic substrates have phase separated iPP and aEPR domains present at the surface, which grow in size as the melt time increases. Surface enrichment of aEPR is observed after exposing melt-pressed blends to n-hexane vapor, which preferentially solvates the aEPR and draws it to the surface.

The effects of mechanical environment on surface properties are discussed in Chapters 7 and 8. These chapters describe changes in surface morphology and surface mechanical properties that result from the application of tensile stress. The surface structure and surface mechanical properties of low and high density polyethylene were characterized by atomic force microscopy (AFM) as the polymers were elongated. The surfaces of both materials roughened as they were stretched. The roughening effect was attributed to deformation of nodular structures, related to bulk spherulites, at the surface. The surface roughening effect was completely reversible at tensile strains in the elastic regime and partially reversible at tensile strains in the plastic regime, until the polymers are irreversibly drawn into fibers.

The surface composition and morphology of a polystyrene(butadiene)styrene triblock copolymer was characterized by AFM and SFG as it was elongated. AFM friction and topography images indicate that when the copolymer is stretched, the deformation at the surface is highly localized by 'cracks', which become deeper and

wider as the polymer is elongated. The inhomogeneous deformation process leads to roughening of the surface. The deformed areas propagate and cover a larger fraction of the total surface area as the polymer is elongated. The deformation zones likely contain highly deformed polybutadiene, the rubbery component.

Finally, the surface mechanical behavior of hydrogels is discussed in Chapter 9. The surface mechanical properties of poly(hydroxyethyl)methacrylate (pHEMA) based hydrogels, used as contact lenses, were monitored as a function of humidity by atomic force microscopy (AFM). Surface mechanical properties were extracted from AFM force vs. distance interaction curves and were found to be strongly dependent on the bulk water content of the lens and on the relative humidity. At low relative humidity, the dehydration rate from the hydrogel surface is faster than the rehydration rate from the bulk, leading to a rigid surface region that has mechanical properties similar to those measured on totally dehydrated lenses. At relative humidity values >60%, the dehydration rate from the hydrogel surface rapidly decreases, leading to higher surface water content and a softer surface region. The results indicate that, in an ocular environment, although the bulk of a pHEMA contact lens is hydrated, the surface region may be in a transition between a dehydrated glassy state and a hydrated rubbery state.

Chapter 1

Application of sum frequency generation (SFG) vibrational spectroscopy and atomic force microscopy to the study of polymer interface structure

1.1 Introduction to SFG surface vibrational spectroscopy

SFG vibrational spectra of polymer interfaces are obtained by overlapping two input fields at a polymer interface and measuring the light generated from the interface at the sum frequency. Theoretical details beyond those presented here can be found in publications by Shen[1,2,3,4] and by Hirose[5]. The sum frequency polarization, $\vec{P}^{(2)}$, induced at the polymer interface is given by Eq. 1-1, where $\vec{\chi}^{(2)}$ is the second order nonlinear susceptibility of the polymer and $\vec{E}(\omega_1)$ and $\vec{E}(\omega_2)$ are the two input fields.

$$\vec{P}(\omega_s) = \vec{\chi}^{(2)}(\omega_s = \omega_1 + \omega_2) : \vec{E}(\omega_1)\vec{E}(\omega_2) \tag{1-1}$$

1

Each of the 27 elements of $\tilde{\chi}^{(2)}$ is equal to zero in materials that possess inversion symmetry. Additionally, the average value of $\tilde{\chi}^{(2)}$ is zero in randomly oriented materials. Elements of $\tilde{\chi}^{(2)}$ can be nonzero in materials that lack inversion symmetry. Often, a material that is randomly oriented in the bulk will assume a preferred orientation at an interface in order to reduce the surface energy, leading to broken symmetry in the surface plane. Thus, measurement of $\tilde{\chi}^{(2)}$ can be specifically sensitive to polar ordering of molecular groups at interfaces.

The intensity of the sum frequency signal is given by Eq. 1-2 and is proportional to the square of the effective surface nonlinear susceptibility, $\chi^{(2)}_{eff}$. The effective surface nonlinear susceptibility is given by Eq. 1-3 where $\hat{e}$ is the unit polarization vector and $\bar{L}(\omega)$ are Fresnel factors, which are dependent on the refractive indices of the two media forming the interface. In quantitatively comparing SFG signals generated from different types of interfaces (polymer/air vs. polymer/liquid) or SFG signals that were collected using different polarization combinations of light, it is necessary to account for these differences using Eq. 1-3 and the equations for the Fresnel factors presented in reference 2.

Different polarization combinations of s and p light probe different elements of the surface nonlinear susceptibility. If the molecular groups at an interface are polar ordered (z-direction) and if the molecular groups are isotropic in the surface x-y plane ($x=y=-x=-y$), then there are four unique elements of the surface nonlinear susceptibility: χ_{yyz} , χ_{yzy} , χ_{zyy} , and χ_{zzz}. In our experiments, we have primarily used the $s_{sum}s_{vis}p_{IR}$ and $s_{sum}p_{vis}s_{IR}$ polarization combinations and probed the χ_{yyz} and χ_{yzy}

components of the surface nonlinear susceptibility, respectively. In the second part of Eq. 1-3, the angle, β, refers to the angle of incidence of the p polarized input field.

$$I(\omega_s) \propto \left| \chi_{eff}^{(2)} \right|^2 \tag{1-2}$$

$$\chi_{eff}^{(2)} = \left[\hat{e}_s \cdot \bar{L}(\omega_s) \right] \bar{\chi}^{(2)} : \left[\hat{e}_1 \cdot \bar{L}(\omega_1) \right] \left[\hat{e}_2 \cdot \bar{L}(\omega_2) \right] \tag{1-3}$$

$$\chi_{eff}^{(2)}(ssp) = L_{yy}(\omega_s) L_{yy}(\omega_1) L_{zz}(\omega_2) \sin \beta_2 \chi_{yyz}^{(2)}$$

$$\chi_{eff}^{(2)}(sps) = L_{yy}(\omega_s) L_{zz}(\omega_1) L_{yy}(\omega_2) \sin \beta_1 \chi_{yzy}^{(2)}$$

In SFG surface *vibrational* spectroscopy, one of the input fields is a tunable infrared beam that is at or near resonance with one or more vibrational modes of the species at an interface. This situation is described by Eq. 1-4, where the surface nonlinear susceptibility contains a nonresonant contribution, $\chi_{NR}^{(2)}$, and a vibrationally resonant contribution, $n_s \left\langle \bar{\alpha}_R^{(2)} \right\rangle_f$. The resonant term is written as the product of the number density of contributing molecular groups at the surface, n_s, and the orientation averaged nonlinear polarizability of those groups (brackets denote an average over a distribution function, f). The resonant term is maximized when the infrared beam (ω_{IR}) is tuned near a vibrational mode belonging to one of the molecular groups at the interface (ω_q). $\bar{A}_q$ is the strength and Γ_q is the damping term associated with a vibrational mode, q.

$$\bar{\chi}^{(2)} = \bar{\chi}_{NR}^{(2)} + n_s \left\langle \bar{\alpha}_R^{(2)} \right\rangle_f = \bar{\chi}_{NR}^{(2)} + \sum_q \frac{\bar{A}_q}{\omega_2 - \omega_q + i\Gamma_q} \tag{1-4}$$

$$\bar{A}_q = n_s \left\langle \bar{a}_q \right\rangle_f$$

$$a_{q,lmn} \propto \left(\frac{\partial \alpha_{lm}}{\partial Q_q} \right) \left(\frac{\partial \mu_n}{\partial Q_q} \right) \qquad (1\text{-}5)$$

SFG spectra can be fit using Eq. 1-4 in order to extract the positions and strengths of vibrational modes. The nonlinear polarizability is defined by Eq. 1-5 and is directly proportional to the product of the polarizability and dipole derivatives of the vibrational mode. The two quantities, $\vec{A}_q$ and $\vec{a}_q$, are related to each other by the number density of contributing oscillators, n_s, and the orientation averaged coordinate transformation.

SFG spectra were primarily collected in the C-H (2700-3100cm^{-1}) stretching region using the $s_{sum}s_{vis}p_{IR}$ polarization combination, which is sensitive to A_{yyz}. This polarization combination is most sensitive to vibrations that have a component of the vibrational dipole (μ_n) along the surface normal, z, and a component of the polarizability tensor (α_{lm}) in the surface plane $(x\text{-}y)$. Spectra were also collected using the $s_{sum}p_{vis}s_{IR}$ polarization combination, which is sensitive to A_{yzy}. If the components of $\vec{a}_q$ for a vibrational resonance are known, then the fitted vibrational mode strengths, $\vec{A}_q$, can be used to determine changes in number density and orientation of the molecular group giving rise to the vibration in the surface region.

For example, for an isolated C-H vibration, the vibrational dipole is along the bond axis (the c-axis in Figure 1-1) and the polarizability derivative is strongest along the bond axis. This means that the largest component of the nonlinear polarizability tensor will be a_{ccc}. The orientation dependence of the SFG signal intensity arising from a collection of C-H groups measured by ssp SFG spectra is given by the

4

relationship, $A_{yyz} = \langle (\hat{y} \cdot \hat{c})(\hat{y} \cdot \hat{c})(\hat{z} \cdot \hat{c}) \rangle a_{ccc}$. The coordinate transformation in this

relationship involves the three Euler angles χ, θ, and ϕ defined in reference 5. The

angle χ is a rotation about the lab fixed z-axis. For an x-y isotropic surface containing

a collection of C-H groups, this angle is integrated over its full range of values. The

angle θ (referred to here as tilt angle) related the z-axis to the molecule frame c-axis.

The final rotation, ϕ, is about the new z-axis (c-axis).
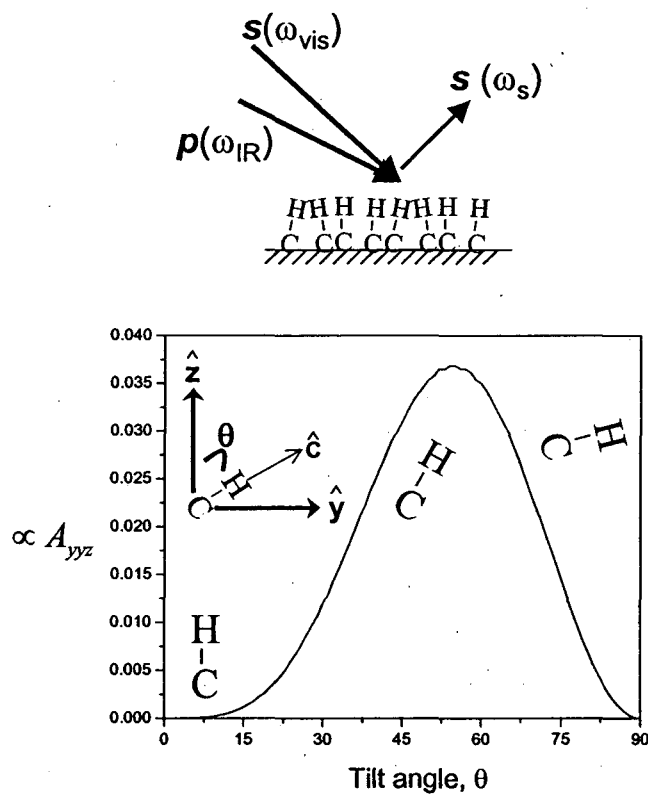
Figure 1-1: Simulated orientation dependence of the ssp SFG mode strength, A_{CH}, for

the C-H vibration.

Considering only the tilt angle, θ, between the lab fixed z-axis and the c-axis

of the bond, a plot of the SFG signal dependence vs. tilt angle is shown in Figure 1-1.

Qualitatively, if the C-H bond is along the z-axis (standing up), then $(\hat{y} \cdot \hat{c})$ will be zero and no SFG signal will be measured. If the bond is along the y-axis (lying flat on the surface) then $(\hat{z} \cdot \hat{c})$ will be zero and no SFG signal will be measured. However, if the bond is tilted with respect to the surface normal, then an SFG signal may be measured.

Similar types of arguments can be made for vibrations originating from CH_2 groups. The nonzero components of $\bar{a}_q$ and their relative values are given in reference 2 for the $CH_2(s)$ (a_{aac}, a_{bbc}, a_{ccc}) and $CH_2(a)$ (a_{aca} and a_{caa}) vibration, and can be estimated for any C-H vibration using the C-H bond additivity model presented in reference 5. The SFG vibrational mode strength dependences on the tilt angle, θ, (defined in Figure 1-2b) for the $CH_2(s)$ and $CH_2(a)$ stretches using a narrow distribution (2°, Gaussian) of tilt angles and a broad distribution (40°, Gaussian) of tilt angles are plotted in Figures 1-2a and 1-2b for the *ssp* and *sps* polarization combinations. In the *ssp* spectra, the $CH_2(s)$ vibration will be largest if the CH_2 groups are oriented with their symmetry axis along the surface normal. In *sps* spectra, the $CH_2(a)$ vibration will be largest if the molecular group is upright.

Simulated ssp SFG spectra generated from a surface made up of an x-y isotropic collection of CH_2 groups are presented in Figure 1-3. These plots compare SFG spectra expected to be measured from a collection of CH_2 groups at an interface that have tilt angle orientation distributions centered at 0°, 30°, 60°, and 90° and Gaussian distribution widths of 2°(narrow), 40°(wide), and 70°(very wide). From Figures 1-2 and 1-3, large ssp SFG signal intensities are expected from interfaces

where the CH_2 groups are upright oriented with a narrow distribution of orientations.

Smaller signal intensities are expected from more randomly oriented interfaces.
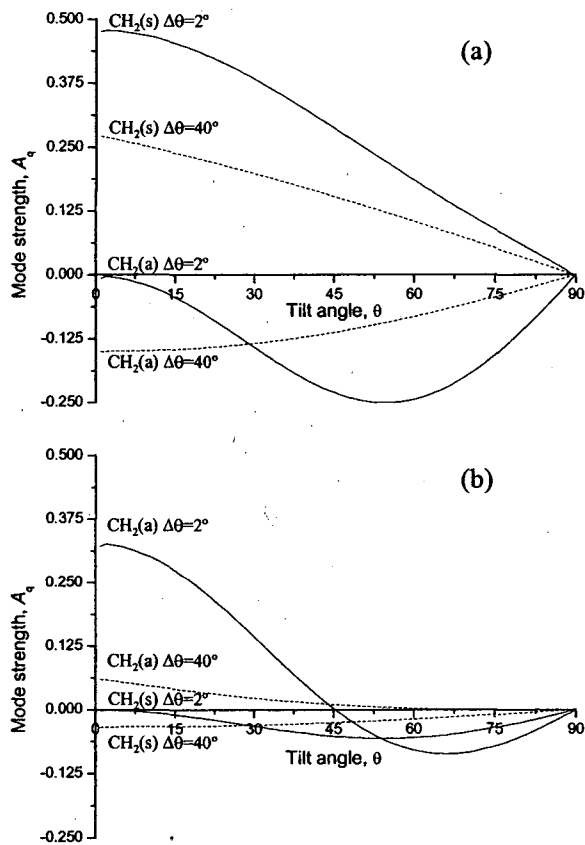
Figure 1-2: (a) Simulated orientation and ordering dependences of the ssp mode strengths for $CH_2(s)$ and $CH_2(a)$ vibrations and (b) simulated orientation and ordering dependences of the sps mode strengths for CH_2 vibrations. ($\phi_c=0°$, $\Delta\phi=5°$)

The ratio of the vibrational mode strengths obtained from *ssp* and *sps* spectra can be used to place restrictions on the orientation of species at an interface. For the CH_2 vibrations, the ratio of the $CH_2(s)/CH_2(a)$ amplitudes will be largest if the CH_2 groups are upright, and will be lower if the CH_2 groups are tilted away from the surface normal. The $CH_3(s)$ and $CH_3(a)$ vibrations qualitatively display the same behavior as the $CH_2(s)$ and $CH_2(a)$ vibrations.
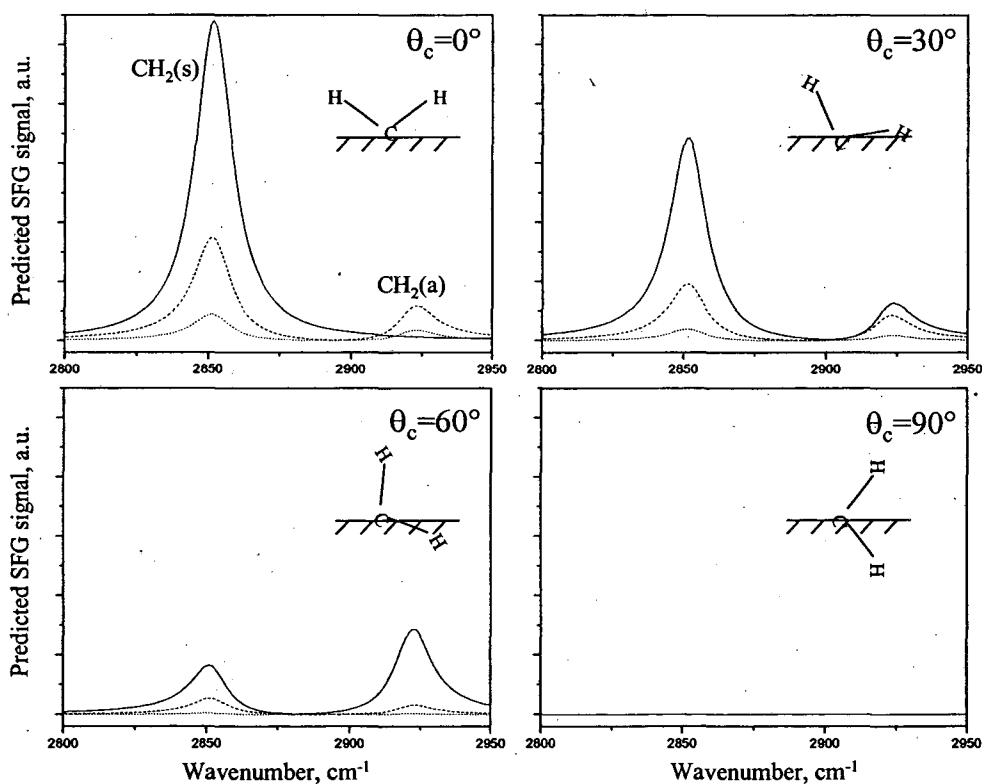
Figure 1-3 Simulated SFG spectra showing the $CH_2(s)$ and $CH_2(a)$ vibrations signal intensity dependences on tilt (θ_c) and randomness ($\Delta\theta$). Solid lines denote a narrow orientation distribution ($\Delta\theta=2°$, Gaussian), dashed lines denote a broad orientation distribution ($\Delta\theta=40°$, Gaussian) of dotted lines denote a very broad orientation distribution ($\Delta\theta=70°$, Gaussian). ($\phi_c=0°$, $\Delta\phi=5°$)

8

Additionally, Figure 1-3 shows that the ratio between the $CH_2(s)$ and $CH_2(a)$ peaks decreases as the distribution width increases. Thus spectra obtained from a surface where the species have a small θ_c and large $\Delta\theta$ may be qualitatively similar to spectra obtained from surfaces where the species have a larger θ_c but smaller $\Delta\theta$. In most cases, it is difficult to distinguish these two cases, especially after taking into account the additional variable of surface number density. It is generally not possible to define an exact average orientation, distribution, and concentration of molecular groups at an interface from SFG data. Often, however, the SFG spectra can be used to significantly restrict the orientation of the species at an interface to a narrow range of values.

1.2 SFG experimental setup

SFG vibrational spectra were obtained using the experimental setup shown schematically in Figure 1-4. A visible and a tunable infrared laser beam were overlapped on the surface of a polymer film at incident angles of 50° and 55° with respect to the z-axis shown in Figure 1-2, and the sum-frequency signal was measured in the reflected direction. The visible beam (ω_{vis}) is 532 nm light generated by frequency doubling the 1064 nm fundamental output from a Continuum Nd:YAG laser (generating ~20ps pulses at 20Hz and 35mJ) through a KTP crystal. The tunable infrared beam (ω_{IR}) is generated from a Laservision OPG/OPA (optical parametric generation)/(optical parametric amplification) system composed of two counter-rotating KTP crystals driven by a portion of the 532nm light. The output of the OPG/OPA stage (720-870nm) is mixed with some of the fundamental 1064nm light in a difference frequency mixing stage comprised of two counter rotating KTA

crystals to generate a tunable IR source from 2000 to 4000 cm^{-1}. Surface vibrational spectra were obtained by tuning the infrared beam and measuring the sum-frequency signal as a function of the infrared frequency. The sum-frequency output signal ($\omega_{sum}=\omega_{vis}+\omega_{IR}$) was collected by a gated integrator and photomultiplier tube.
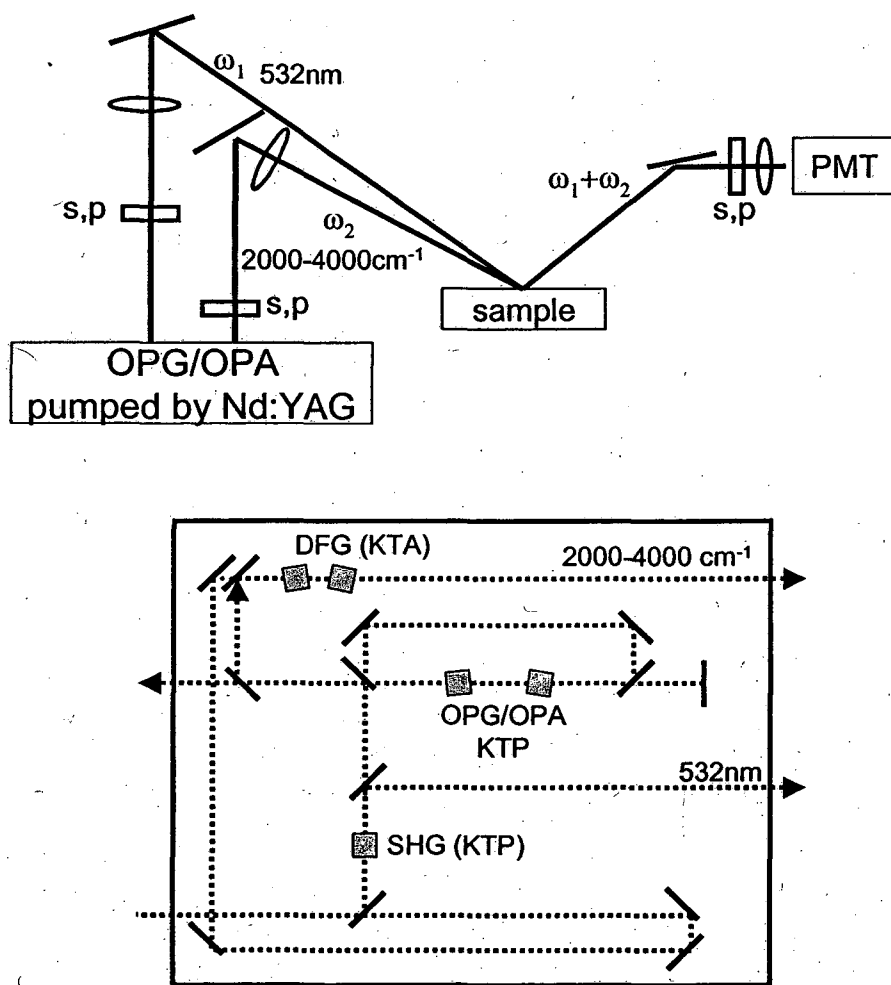
Figure 1-4: Schematic of the SFG experimental setup and the OPG/OPA system.

1.3 Examples of SFG spectra obtained from polymer/air interfaces

Polyethylene/air and polyethylene glycol/air interfaces

An SFG spectrum (*ssp* polarization combination) obtained from the surface of a polyethylene film (low density polyethylene, melt pressed at 120°C and quenched to room temperature) is shown in Figure 1-5a. The peak at $2850cm^{-1}$ has been assigned to the $CH_2(s)$ stretch and the feature at $2920cm^{-1}$ to the $CH_2(a)$ stretch.[6] An SFG spectrum of a polyethylene glycol film spin cast from methanol onto glass is also shown in Figure 1-5b. In this spectrum the peak at $2820cm^{-1}$ has been assigned as the $CH_2(s)$ stretch.[7]

The relatively large SFG signal measured from each of these polymers indicates that portions of the backbone are ordered at the polymer/air interface. In both spectra, the $CH_2(s)$ stretch is much larger than the $CH_2(a)$ stretch suggesting that the CH_2 units contributing to the measured SFG signal are oriented more or less out of the surface. However, for both of these polymers, adjacent CH_2 units that are in a *trans* configuration have local inversion symmetry and the SFG signals arising from them are expected to cancel one another.[8] Most of the CH_2 signal in these polymers is expected to arise from *gauche* defects in the chains. Although it is clear from these spectra that portions of the backbone are ordered at the interface, because of the possibility of cancellation of the *trans* segments, it is not reasonable to deduce the overall configuration of CH_2 units at the surface from the SFG spectrum.
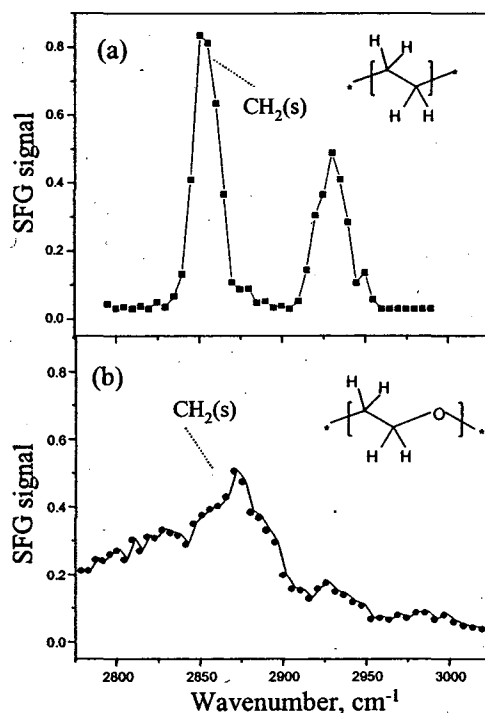
Figure 1-5: SFG spectra of (a) low density polyethylene and (b) polyethylene oxide.

Both spectra were generated using the *ssp* polarization combination

Atactic polypropylene/air, atactic polybutene/air, polystyrene/air and poly(4-methyl)styrene/air interfaces

Low surface energy side branches have a significant effect on SFG spectra measured at the polymer/air interface. SFG spectra obtained from atactic polypropylene (*a*PP) and from atactic polybutene (*a*PB) films spin cast from n-hexane onto glass are shown in Figure 1-6a and 1-6b. In these ssp spectra, the feature

at 2883cm^{-1} is the strongest feature in both the *a*PP and *a*PB spectra and is assigned as the CH$_3$(s) stretch from the side branches.[6,9]

For *a*PP, the features at 2850cm^{-1} and 2920cm^{-1} are assigned as the CH$_2$ symmetric (CH$_2$(s)) and antisymmetric (CH$_2$(a)) stretches, respectively, from the polymer backbone and are significantly smaller than the CH$_3$(s) stretch. The feature at 2968cm^{-1} is assigned to the CH$_3$ antisymmetric (CH$_3$(a)) stretch from the methyl side branch. The SFG spectrum of *a*PB is qualitatively similar to the spectra of *a*PP. For *a*PB, the broader peak at 2850-60cm^{-1} can be assigned as the CH$_2$(s) stretch arising from the CH$_2$ groups on the side branch and in the backbone.

Like the CH$_2$(s) stretch, the CH$_3$(s) stretch will be largest in the ssp spectra if the methyl groups are oriented upright. A large ratio of the CH$_3$(s)/CH$_3$(a) stretch can reflect an upright orientation. For *a*PB, this ratio is smaller than it is for *a*PP, indicating that the *a*PB methyl groups at the surface may be tilted at a higher angle than the *a*PP methyl groups – consistent with the extra degree of freedom afforded by the longer ethyl branch. Alternatively, the smaller CH$_3$(s):CH$_3$(a) ratio may indicate that the terminal CH$_3$ groups may be more randomly oriented than in *a*PP – also consistent with the extra degree of freedom afforded by the longer ethyl branch.
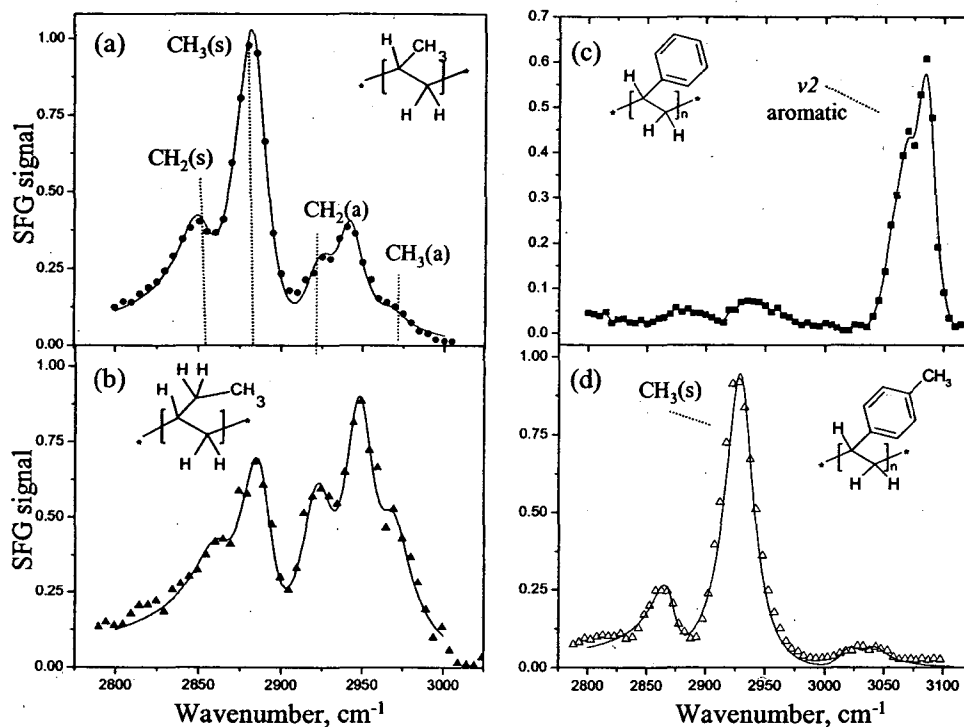
Figure 1-6: SFG spectra of (a) atactic polypropylene (*a*PP), (b) atactic polybutene (*a*PB), (c) polystyrene, and (d) poly(4-methyl) styrene. Each spectrum was generated using the ssp polarization combination

An SFG spectrum ($s_{sum}s_{vis}p_{ir}$ polarization combination) of a polystyrene film spin cast from toluene and then annealed at 110°C for 12 hours is shown in Figure 1-6c. The spectrum is qualitatively similar to previously published spectra where the dominant feature is the symmetric *v2* stretch from the aromatic side group at

~3060cm^{-1}.[10,11] The $v2$ stretch has the same symmetry as the CH$_2$(s) stretch and will also tend to be largest if the molecular group is oriented upright at the interface. This is in agreement with recent theoretical calculations predicting that the phenyl side branch should be oriented away from the polymer bulk at the surface.[12]

An SFG spectra of poly(4-methyl)styrene is shown in Figure 1-6d. The dominant feature in this spectrum is at 2920cm^{-1} and can be assigned as the CH$_3$(s) stretch from the methyl group indicating that the side branches are well ordered. The symmetric $v2$ aromatic stretch is not seen in this spectrum because although the $v2$ stretch is Raman active - for *para* substituted aromatics the mode is IR inactive, making the mode SFG inactive (Eq. 1-4).

These four examples show that large low surface energy side branches tend to order at the air interface. In contrast, if the polymer has a hydrophilic side branch instead of a hydrophobic branch, then the low surface tension backbone will tend to order at the air interface. Wei et al. have observed that for polyvinyl alcohol, which has hydroxyl side branches, that the CH$_2$ backbone of the polymer orders at the air interface.[13]

Poly(α-methyl)styrene/air and poly(hydroxyethyl)methacrylate/air

For polymers with more than one large side branch per monomer unit, steric restrictions are a factor when considering how the polymer orders at an interface. An SFG spectra of poly(α-methyl)styrene, which has a methyl branch and a phenyl branch attached to the same backbone carbon atom, is shown in Figure 1-7a. The spectrum is dramatically different from the SFG spectra of polypropylene and of

polystyrene. In particular, the overall intensity of the SFG signal is dramatically reduced. The peak attributed to the *v2* mode of the phenyl branch is visible at ~3060cm^{-1} however it is significantly weaker than the *v2* mode seen in the SFG spectra of pure polystyrene. Similarly, the peak associated with the $CH_3(s)$ mode at ~2880cm^{-1} is visible but is much weaker than the $CH_3(s)$ mode of polypropylene. These observations suggest that neither side branch is strongly oriented upright at the interface. In poly(α-methyl)styrene the methyl group is expected to have slightly lower surface tension than the aromatic side branch,[14] however, the aromatic branch is slightly larger, suggesting a competition between these two variables.

An SFG spectra of poly(hydroxyethyl)methacrylate, is shown in Figure 1-7b. The feature at 2880cm^{-1} can be assigned as the $CH_3(s)$ stretch and the feature at 2940cm^{-1} can be assigned as the $CH_3(a)$ stretch and methyl Fermi resonance.[15] There is very little intensity from the CH_2 groups of the hydroxyethyl branch indicating that it is not strongly ordered at the air interface. This indicates that the smaller methyl group orders at the air interface and suggests that surface tension differences of the individual side branched influences ordering at the interface. In contrast, SFG studies of poly(methyl)methacrylate (PMMA), which has a has a small methyl side branch and a much larger methyl methacrylate side branch, have shown that the dominant spectral feature arises from the terminal methyl branch of the larger ester side branch – indicating that the bulky, low surface tension branch is upright oriented at the interface.[16]
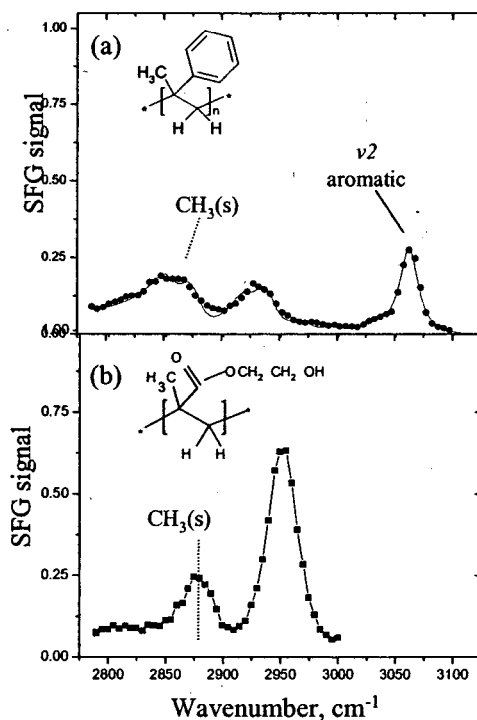
Figure 1-7: SFG spectra of polymers with two hydrophobic groups per monomer repeat unit (a) poly(α-methyl)styrene and (b) poly(hydroxyethyl)methacrylate. Each spectrum was generated using the ssp polarization combination

1.4 Atomic force microscopy (AFM)

The preceding examples show that SFG surface vibrational spectroscopy is highly sensitive to the average orientation of molecular groups at an interface, and as such, gives a restricted view of the overall structure of the surface. When data from SFG spectra can be analyzed alongside data obtained from other surface sensitive techniques, such as XPS or atomic force microscopy (AFM), the picture of the polymer surface behavior becomes more robust and the interpretation of data more

17

meaningful. AFM is a member of the family of scanned probe techniques, and was initially demonstrated by Binnig and Quate in the mid 1980's.[17] Since the mid 1990's, the popularity of AFM as an experimental technique has increased dramatically, and it is rare to find a lab that does not have or have access to a force microscope.

AFM is used in these experiments to measure the lateral structure of the interface, which SFG is insensitive to, and in some cases to measure the surface mechanical behavior. Several force microscopes were used to obtain the results presented in the following chapters and the specifics of the microscopes are discussed in later chapters. The basic principles of these microscopes are similar. A sharp (radius of curvature <20nm) or blunt (radius of curvature ~ 1 micron) tip is mounted on the underside of a flexible cantilever. This tip is brought into contact or near contact with the surface of interest by a stepper motor or other micron-scale approach mechanism. Fine control of the tip/cantilever position is achieved through the use of piezoelectric actuators. As the tip interacts with the surface either attractively or repulsively, the cantilever bends. The bending of the cantilever can be measured by monitoring the position of light (generated by a diode laser) reflected off the topside of the cantilever and into a position sensitive photodiode.

1.5 Application of AFM to polymer surfaces

The most common use of AFM is as an imaging tool. Topographic images can be recorded by placing the tip in a position where it presses against the surface of interest, and the cantilever bends by a defined amount (by a constant load). A feedback mechanism between the photodiode detector and piezoelectric actuator maintains the position of the cantilever, such that it always bends by the same

amount. The tip is then scanned and across the surface and a map of the surface topography is produced. Images can also be produced by recording the torsion (lateral force) of the cantilever as the tip slides across the surface.
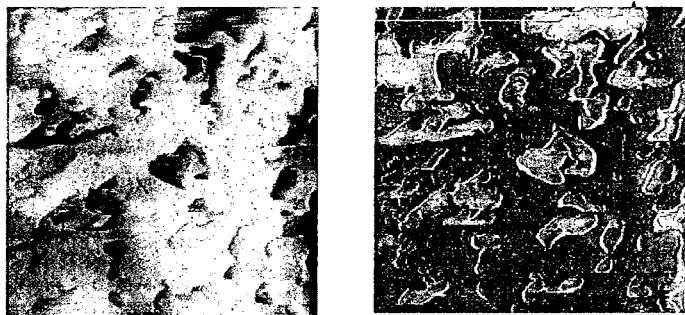
Figure 1-8: 25x25μm AFM contact mode topography image (left) and corresponding AFM friction image (right) of a blend of *i*PP and *a*EPR. The high friction regions (light) correspond to depressed regions on the topography image (dark) and are assigned as *a*EPR.

Many polymers are soft materials and the AFM tip can easily penetrate/push into the surface. This can be useful for distinguishing two polymers at an interface. An example, presented in more detail in Chapter 6, is shown in Figure 1-8. The image on the left is a topography image and the image on the right is a friction image obtained from the surface of a blend of isotactic polypropylene (*i*PP) and aspecific poly(ethylene-co-propylene)rubber. Mechanically, the *i*PP phase is crystalline and rigid. The *a*EPR phase is much softer. In the topography image, the *a*EPR phase shows up as depressed regions. If an image is made at higher loads, the depressions appear deeper. This phenomenon is also described in more detail in Chapter 6, but shows that soft surfaces can be deformed by the load of the cantilever. To obtain true images of the topography, it is necessary to scan the surface with low loads or in a

noncontact imaging mode. The friction image can also distinguish the two materials, based on their difference in mechanical properties. In the friction image, the *a*EPR domains appear bright (high friction). This is characteristic of soft materials, which can form much larger contact areas with the AFM tip and may have stronger adhesive interaction with the tip.

The force/displacement curves can be used to extract qualitative and sometimes quantitative behavior of the surface mechanical behavior. Two force-displacement curves, obtained from the surface of pHEMA, are shown in Figure 1-9. The force displacement curve measures the bending of the cantilever as it is pressed against a surface. Initially, the cantilever is far away from the surface. As the tip approaches the surface, there is an attractive interaction between the tip and sample. This leads to instability and the tip 'snaps into' the surface. As the tip presses against the surface, the cantilever bends and the polymer surface can be deformed. The tip is then retracted from the surface. In the two force curves shown, there is an adhesive interaction between the tip and the surface, leading to a strong 'pull off force'. The work of adhesion can estimated by projecting the pull off force over the area of contact between the tip and surface.

The relationship between the approach and retract curves can indicate if the surface was deformed elastically or plastically. If there is no deformation of the surface, or if the surface was deformed elastically, the approach and retract curves overlap one another. If there is plastic deformation, it can manifest itself as difference in the slopes of these two curves. In both situations, the initial slope of the retract curve is generally taken as the stiffness, and is assumed to be primarily dependent on

the elastic behavior of the cantilever and the sample. If this stiffness is projected onto a contact area, then the elastic modulus of the polymer surface can be estimated. More detail of the procedures and the assumptions involved for making this transformation are given in Chapters 7 and 9.
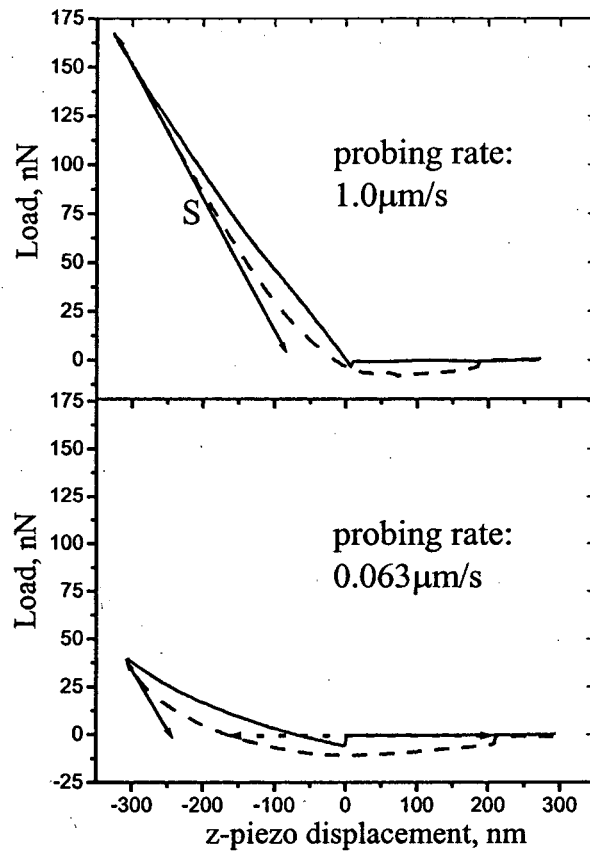
Figure 1-9: Comparison of AFM force vs. distance curves collected at 0.063μm/s and 10μm/s probing rates on the bulk-hydrated pHEMA contact lens. The solid line is the approach (loading) curve, the dashed line is the retraction (unloading) curve, and the solid arrow represents the best-fit slope of the initial part of the retraction curve (the stiffness).

Additionally, as will be shown in Chapter 9, hysteresis between the approach and retract curves can indicate polymer relaxation processes. In Chapter 9, humidity dependent surface relaxation processes were probed by obtaining force distance curves at various rates. The two curves shown in Figure 1-9 show that there is a measurement rate dependence of the force curves. The curve collected at a faster rate reaches a higher maximum load (the cantilever bends less) than the curve collected at a slower rate. The faster curve is insensitive to the relaxation process of the hydrogel and measures primarily elastic behavior. The slower rate allows the polymer to deform during the measurement and allow the tip to penetrate deeper into the surface for a given displacement of the z-piezo.

1.6 Conclusion

This chapter introduced SFG surface vibrational spectroscopy and atomic force microscopy. The concepts of SFG vibrational spectroscopy, relevant to understanding and interpreting SFG spectra obtained from polymer interfaces, have been presented. Examples were presented showing that SFG spectra obtained from polymer/air interfaces are strongly sensitive to ordering at the interface. The dependence of the SFG signal on ordering is also a limitation of SFG as a surface analysis technique. Although a species may be present at the interface in great quantity, if it is not well-ordered and if it does not have a vibrational mode that is both IR and Raman active, the species will not be detected by SFG. Additionally, even if the species is ordered at the interface and has an SFG active vibrational mode, unless it is oriented in an appropriate direction (see Fig. 1-1 to 1-3), the measured SFG peak intensity may very weak.

In spite of these limitations, the following chapters highlight some of the unique information that can be extracted from SFG spectra collected from polymer interfaces. Of special interest are the cases where SFG data can be correlated to data obtained using AFM. Particularly in Chapter 5, SFG has been used to determine the monolayer composition of the interface, while AFM is used as an imaging tool, to determine the lateral morphology. Other examples presented in this Chapters 7-9 highlight unique applications of AFM to study the surfaces of stretched (deformed) polymers) and to study the surface behavior of hydrogels.

References

[1] Shen, Y.R., *Principles of Nonlinear Optics*, John Wiley & Sons, New York, 1984.

[2] Wei, X.; Hong, S.C.; Zhuang, X.W.; Goto, T.; Shen, Y.R. *Phys. Rev. E* **2000**, *62*, 5160.

[3] Miranda, P.B.; Shen, Y.R. *J. Phys. Chem. B* **1999**, *103*, 3292.

[4] Zhuang, X.; Miranda, P.B.; Kim, D.; Shen, Y.R. *Phys. Rev. B* **1999**, *59*, 12632.

[5] Hirose, C.; Akamatsu, N.; Domen, K. *Appl. Spect.* **1992**, *46*, 1051.

[6] Zhang, D.; Shen, Y.R.; Somorjai, G.A. *Chem. Phys. Lett.* **1997**, *281*, 394.

[7] Chen, Z.; Ward R.; Baldelli S.; Opdahl, A; Shen, Y.R.; and Somorjai, G.A. *J. Am. Chem. Soc.* **2000**, *122*, 10615.

[8] Casson, B.D.; Bain, C.D. *J. Phys. Chem. B* **1999**, *103*, 4678.

[9] Opdahl, A.; Phillips, R. A.; Somorjai, G. A. *J. Phys. Chem. B.* **2002**, *106*, 5212.

[10] Gautam, K.S.; Schwab, A.D.; Dhinojwala, A.; Zhang, D.; Dougal, S.M.; Yeganeh, M.S. *Phys. Rev. Lett.* **2000**, *85*, 3854.

[11] Briggman, K. A.; Stephenson, J. C.; Wallace, W. E.; Richter, L. J. *J. Phys. Chem. B.,* **2001,** *105,* 2785.

[12] Clancy, T.C.; J. Hwan Jang, A. Dhinojwala, and W.L. Mattice, *J. Phys. Chem. B,* **2001,** *105,* 11493.

[13] Wei X. Zhuang XW. Hong SC. Goto T. Shen YR. *Phys. Rev. Lett.* **1999,** *82,* 4256.

[14] Brandup, J.; Immergut, E.H.; Grulke, E.A. *Polymer Handbook, 4th Edition* John Wiley & Sons, New York, 1999.

[15] Chen, Q.; Zhang, D.; Somorjai, G.; Bertozzi, C. R.; *J. Am. Chem. Soc.* **1999,** *121,* 446.

[16] Wang, J.; Chen, C.; Buck, S. M.; Chen, Z. *J. Phys. Chem. B.* **2001,** *105,* 12118.

[17] Binnig, G.; Quate, C.F.; Geber, C. *Phys. Rev. Letters,* **1986,** *56,* 930.

Chapter 2

Surface segregation of methyl branches in poly(ethylene-co-propylene) copolymers quantified by SFG

2.1 Introduction

Polyolefins represent model systems for studying the effects of chain architecture on surface structure, as variables including the number of short chain branches, the length of chain branches, and polymer tacticity can be isolated. The effect of short-chain branch content on surface structure is particularly interesting in the context of experimental studies, which suggest that species with higher branch content segregate to the air/polymer surface in polyolefin blends.[1] While enthalpic arguments have been made to explain the relative surface affinities, the details of the surface configuration as a function of branch content for the pure components has not been extensively explored and may give additional insights to the segregation behavior. In the experiments presented here,

the effect of the number density of methyl side branches on the surface structure has been studied.

A series of random aspecific poly(ethylene-co-propylene) copolymers *(aEPR)*, having the basic structure shown in Figure 2-1, was synthesized and the surface structures were characterized by sum frequency generation vibrational spectroscopy (SFG). The ethylene mole fraction randomly incorporated in the backbone was varied from 0% to 42% (increasing the ethylene content of the copolymer decreases the number density of methyl side branches). The aspecific placement of propylene monomers removes complications arising from crystallinity.
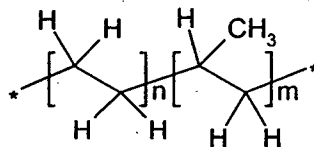
Figure 2-1: Structure of aspecific poly(ethylene-co-propylene) rubber (*a*EPR). The distribution of block lengths (n,m) is very nearly random and methyl group placement in the propylene units lack stereospecificity.

The examples presented in Chapter 1 showed that for polymers with low surface energy side branches, that the side branches preferentially order at the air/polymer interface. The tendency to order side branches out of the air surface interface has been observed for polypropylene[2] and for polystyrene.[3,4] Additionally, for branched polyimide derivatives, it has been found that hydrophobic side chains orient out of the surface.[5] For polypropylene it was also shown that tacticity is important in determining the surface configuration.[3] In this chapter, SFG spectra are used to quantify relative changes in

number density and orientation of CH_3 side branches and CH_2 backbone units at the air/polymer interface for the *a*EPR copolymers as the concentration of side branches in the polymer chain is varied.

Methyl side branches are found to preferentially order at the surface regardless of copolymer composition. The presence of ethylene units in the backbone does not change the methyl orientation at the surface significantly but does allow the CH_2 backbone to orient more upright. We are able to deduce relative changes in the number density of methyl groups at the surface and changes in the conformation of surface chain segments. In general, inserting ethylene units into the polymer backbone decreases the steric hindrances between adjacent methyl groups. This is proposed to allow the ethylene-rich copolymers to have more chain segments in *trans* configurations at the surface and to assume configurations that orient a relative surface excess of methyl groups out of the surface.

2.2 Experimental procedures

Polymers

Table 2-1 summarizes the samples used in this study. The results in Table 2-1 suggest that the distribution of block lengths (n,m) in Figure 2-1 is very nearly random and methyl group placement in the propylene units lacks stereospecificity. Dibutylsilylbis(9-fluorenyl)zirconium dichloride catalyst was used to prepare the atactic polypropylene homopolymer (*a*PP1) and aspecific ethylene/propylene copolymers/rubber (*a*EPR2-7) in hexane with a methylaluminoxane (MAO) activator at 70 °C polymerization temperature and a molar [Al]/[Zr] ratio of 2000-3000. Closely related analogs to this aspecific catalyst have been published previously.[6] The *a*EPR copolymers

were prepared by maintaining a constant monomer feed ratio. Differential Scanning Calorimetry analysis of the copolymers showed a single, composition dependent glass transition temperature with no evidence of crystallinity for each copolymer. The as-polymerized polymers were dissolved in hexane solutions, filtered to remove large-scale polymerization impurities, and recovered by evaporation of solvent.

Table 2-1: Structural characteristics of aPP1 and the aEPR copolymers.

Sample	M_w	M_w/M_n	wt. % ethylene	mole fct. ethylene	$[CH_2]/[CH_3]_{bulk}$	Sequence parameter[b]
aPP1[a]	54,000	2.0	0	0	1	-
aEPR2	48,000	2.0	4.7	0.069	1.15	1.0
aEPR3	54,000	2.0	7.1	0.103	1.23	1.0
aEPR4	54,000	2.0	13.5	0.190	1.47	1.1
aEPR5	48,000	2.0	20.3	0.277	1.76	1.3
aEPR6	54,000	2.0	25.9	0.344	2.05	1.3
aEPR7	54,000	2.0	32.3	0.417	2.43	1.4

[a]16%iso triads, 49%hetero triads, 35%syndio triads
[b]The sequence parameter, determined by NMR, is a measure of the randomness of the copolymer. It is 1 for a completely *random* distribution of comonomers, 2 for complete *alternation* of comonomers, and 0 for complete *block*-like sequencing.

The tacticity and composition of aPP and each aEPR copolymer was determined by ^{13}CNMR using a Varian UNITY-300 spectrometer at 75.4 MHz in 10% orthodichlorobenzene solutions at 130 °C. Ethylene content was determined from the compositional triads. The NMR sequence parameter (*s.p.*), determined from compositional diads, is given in Table 2-1 and has a value of 1 for a random distribution of comonomers, >1 for alternating sequencing (*s.p.*=2 for complete alternation), and <1 for block-like sequencing (*s.p.*=0 for complete blocks).[7] The weight average molecular weight (M_w) and polydispersity (M_w/M_n) were determined by high temperature gel

permeation chromatography in trichlorobenzene using a Waters 150-C GPC calibrated with polystyrene standards and converted to PP equivalents without further correction for ethylene content.

Thin films were prepared by spin casting 5% wt. polymer solutions in n-hexane onto IR grade fused silica substrates. After casting, the films were annealed at 70° C for 12 hours. Films were measured by AFM to have thickness between 200 and 300nm.

Sum Frequency Generation Vibrational Spectroscopy

Surface vibrational spectra were obtained by sum frequency generation (SFG) vibrational spectroscopy using the experimental setup described in Chapter 1. In addition to the information presented in Chapter 1, details relevant to the interpretation of spectra presented in this Chapter SFG can be found in references 8,9,10. After normalization, each spectrum was fit to Eq. 2-1 in order to extract values for the vibrationally resonant component, $\tilde{A}$, of the surface nonlinear polarizability. Spectra were collected in the C-H stretching region using the $s_{sum}s_{vis}p_{IR}$ polarization combination, which specifically probes the A_{yyz} component of $\tilde{A}$ and is most sensitive to vibrations that have a component of the vibrational dipole (μ_n) along the surface normal, z, and a component of the polarizability tensor (α_{lm}) in the surface plane $(x$-$y)$. Additional spectra were collected using the $s_{sum}p_{vis}s_{IR}$ polarization combination, which is sensitive to the A_{yzy} component of $\tilde{A}$. The components of the molecular nonlinear polarizability, $\tilde{a}$, for each vibrational resonance were used to determine changes in number density and orientation of CH_2 and CH_3 groups at the surface contributing to the sum frequency signal.

$$I_{SF} \propto \left| \tilde{\chi}_{NR}^{(2)} + \sum_q \frac{\tilde{A}_q}{\omega_2 - \omega_q + i\Gamma_q} \right|^2 \qquad (2\text{-}1)$$

$$\vec{A}_q = n_s \left\langle \vec{a}_q \right\rangle_f \qquad \qquad (2\text{-}2)$$

The internal coordinate systems used to describe the CH_2 group and the CH_3 group are defined in Fig. 2-2 as are the Euler angles θ and ϕ which relate the laboratory-fixed coordinate system to the molecular internal coordinate systems. In these experiments, the surface of the polymer films is assumed to be isotropic in the surface plane and the azimuthal Euler angle has been integrated over its full range of values.
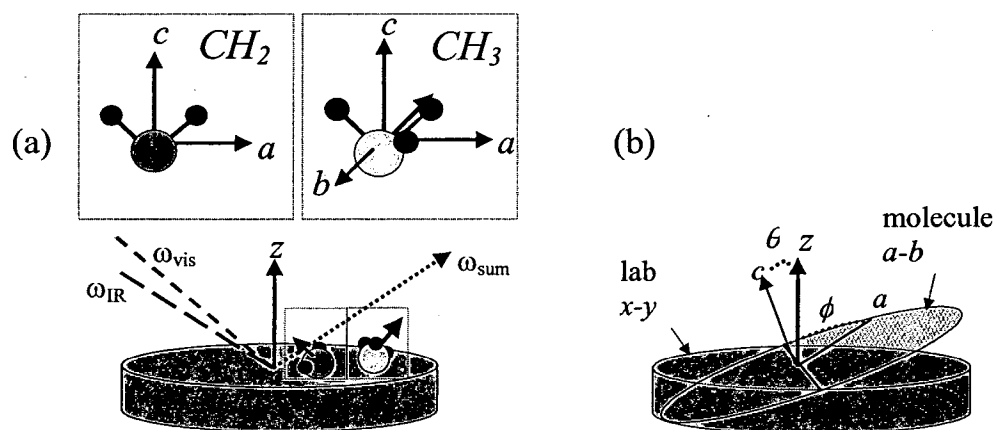
Figure 2-2: (a) Molecular (a,b,c) coordinate systems used in describing the CH_2 and the CH_3 groups, and (b) relationship between the molecular and lab fixed (x,y,z) coordinate systems.

2.3 SFG spectra of poly(ethylene-co-propylene) rubber (aEPR) series

SFG spectra for atactic polypropylene (aPP1) and three of the poly(ethylene-co-propylene) rubber copolymers (aEPR4, aEPR5, and aEPR7) using the ssp polarization combination are shown in Figure 2-3. The feature at 2883cm^{-1} in the aPP1 spectra is the strongest feature in the series. The SFG spectra of each of the other aEPR copolymers

have been normalized, using the peak at 2883cm^{-1} from *a*PP1 as a reference value. Thus in the analysis that follows, all chemical concentrations derived from the SFG spectra are relative to the surface composition of *a*PP1.
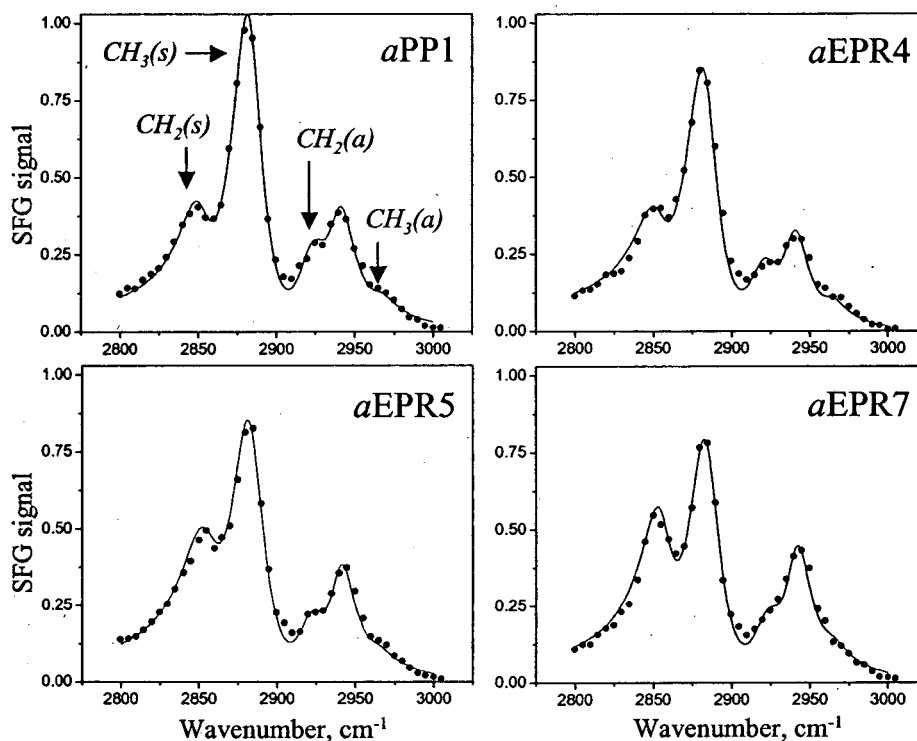
Figure 2-3: SFG spectra of *a*PP1 and *a*EPR4, 5, and 7 copolymers (*ssp* polarization combination). Each spectrum has been normalized using the peak at 2883cm^{-1} for *a*PP1 (the strongest peak in the series) as a reference. Solid lines represent best fits to Eq. 2-1.

As described in Chapter 1, the features at 2850cm^{-1} and 2920cm^{-1} are assigned as the CH$_2$ symmetric (CH$_2$(s)) and antisymmetric (CH$_2$(a)) stretches, respectively, from the polymer backbone. Features at 2883cm^{-1} and the shoulder at 2968cm^{-1} are assigned to the CH$_3$ symmetric (CH$_3$(s)) and antisymmetric (CH$_3$(a)) stretches from the methyl side

branch. An additional feature at 2940cm^{-1} arises from the Fermi resonance between the CH$_3$(s) and an overtone of the CH$_3$ antisymmetric bending mode.

The *ssp* spectra of the *a*EPR copolymers in the series contain the same features as *a*PP1, however the CH$_2$(s) and CH$_2$(a) stretches become more intense relative to the methyl stretches as the ethylene weight fraction increases. SFG spectra of *a*EPR2 and *a*EPR3 (not shown) are intermediate in character to the SFG spectra obtained from *a*PP1 and *a*EPR4 and the SFG spectrum of *a*EPR6 is intermediate to *a*EPR5 and *a*EPR7.
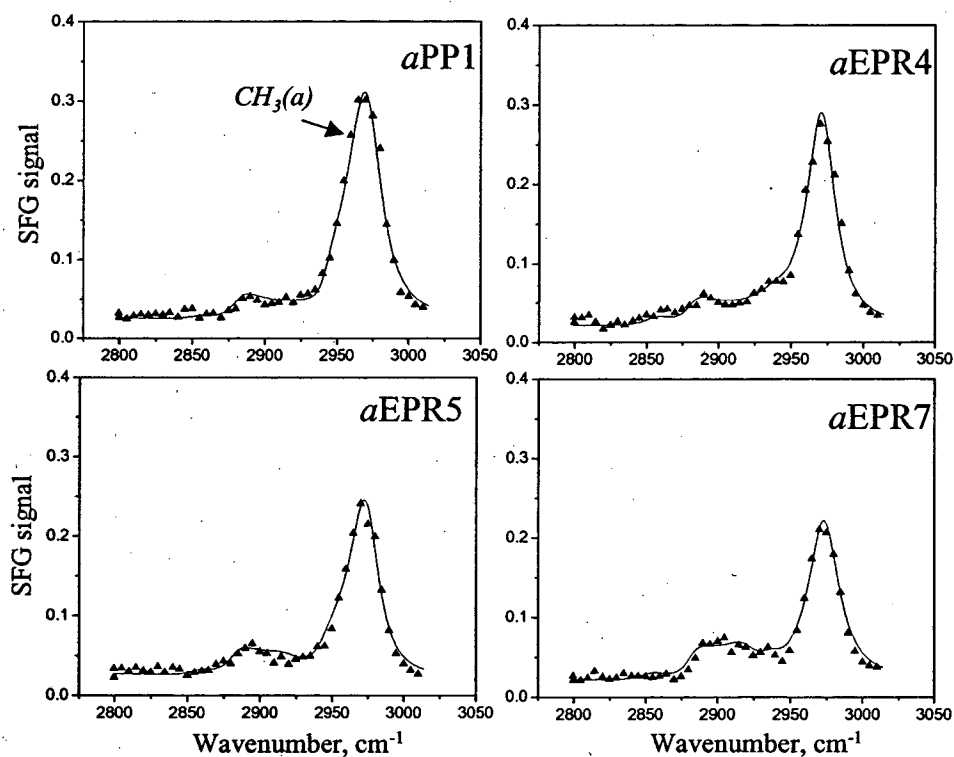
Figure 2-4: SFG spectra of *a*EPR copolymers (*sps* polarization combination). Solid lines represent best fits to Equation 1-1.

Figure 2-4 shows the SFG spectra for the copolymers using the *sps* polarization combination. In these spectra, the CH$_3$(a) peak is the dominant feature for each

copolymer. As the ethylene fraction increases, a broad region from 2890-2940cm^{-1} which contains contributions from the CH$_3$(s), CH$_2$(a), and methyl Fermi resonance increases in intensity. Solid lines on Figures 2-3 and 2-4 represent best fits to the data using Eq. 2-1 and fitting to five peaks where A_q is the normalized mode strength, ω_q is the position of the vibrational peak, and Γ_q is the damping factor for the vibration (between 11 and 13 cm^{-1} for all peaks). The fitted and normalized mode strengths are given in Table 2-2 for both polarization combinations (*ssp* and *sps*).

Comparing the two extremes in the copolymer series, *a*PP1 and *a*EPR7, there is an ~40% decrease in the bulk concentration of methyl groups. However, the SFG vibrational mode strengths for the *ssp* CH$_3$(s) and CH$_3$(a) peaks decrease by <20%. Additionally, the CH$_2$ bulk concentration increases by ~40% between *a*PP1 and *a*EPR7, but the CH$_2$(s) *ssp* mode strength increases by nearly 100%. From Eq. 2-1 and 2-2, it can be seen that in the absence of orientation changes, the SFG mode strengths are expected to vary linearly with number density. That the CH$_2$(s) and CH$_3$(s) vibrational mode strengths do not vary linearly with bulk concentration is a strong indication that there are significant changes in polymer composition, orientation, or ordering at the polymer/air interface as the bulk composition is varied.

Table 2-2: Relative vibrational mode strengths obtained from SFG spectra using Eq. 2-1. Magnitudes of the mode strengths have been normalized such that the $CH_3(s)$ stretch from aPP1 ($2883cm^{-1}$) has an SFG intensity of 1.

	mole fraction ethylene	$CH_2(s)$ $\sim 2850cm^{-1}$		$CH_3(s)$ $\sim 2883cm^{-1}$	
		ssp	sps	ssp	sps
aPP1	0	3.09±0.13	1.0±0.5	10.94±0.06	2.1±0.6
aEPR2	0.069	3.22±0.15		10.75±0.06	
aEPR3	0.103	3.17±0.15		10.75±0.06	
aEPR4	0.190	3.30±0.16	0.2±0.2	10.35±0.09	2.2±0.6
aEPR5	0.277	4.3±0.2	1.4±0.7	10.03±0.08	2.1±0.5
aEPR6	0.344	4.9±0.2		9.87±0.08	
aEPR7	0.417	5.5±0.2	1.1±0.5	9.55±0.08	2.0±0.6

	$CH_2(a)$ $\sim 2920cm^{-1}$		Fermi $\sim 2940cm^{-1}$		$CH_3(a)$ $\sim 2968cm^{-1}$	
	ssp	sps	ssp	sps	ssp	sps
APP1	3.8±0.2	1.3±0.6	3.8±0.2	1.7±0.8	0.7±0.2	-7,1±0.2
AEPR2	3.7±0.2				0.7±0.2	
AEPR3	3.6±0.2				0.7±0.2	
aEPR4	3.4±0.2	1.5±0.7	3.8±0.2	1.1±0.5	0.9±0.2	-6.6±0.2
aEPR5	3.6±0.2	-3.0±1.8	4.3±0.2	3.4±0.8	0.6±0.2	-6.2±0.2
aEPR6	3.5±0.2				0.6±0.2	
aEPR7	3.6±0.2	-3.5±1.6	4.6±0.2	3.2±1.2	0.6±0.2	-5.9±0.2

The ratio of A_{yyz} for the $CH_2(s)$ stretch ($\sim 2850cm^{-1}$) to A_{yyz} for the $CH_3(s)$ stretch ($\sim 2883cm^{-1}$) as a function of the bulk CH_2 to CH_3 mole ratio for the aPP and the aEPR series is plotted in Figure 2-5. This mode strength ratio increases with composition in a roughly linear fashion over the copolymer compositional range we have investigated. Because the individual mode strengths depend on both the number density and the orientation of the contributing molecules, the ratio of the CH_2 and CH_3 SFG mode strengths given in Eq. 2-3 is not simply related to the number concentration of CH_2 and

CH₃ groups at the surface, but represents a convolution of the ratios of the concentration

and orientation of those groups.

$$\frac{A_{yyz}\left(CH_2(s)\right)}{A_{yyz}\left(CH_3(s)\right)} = \left(\frac{n_{CH_2}\left\langle\tilde{a}_{CH_2,yyz}\right\rangle_f}{n_{CH_3}\left\langle\tilde{a}_{CH_3,yyz}\right\rangle_f}\right)_{surface}$$

(2-3)
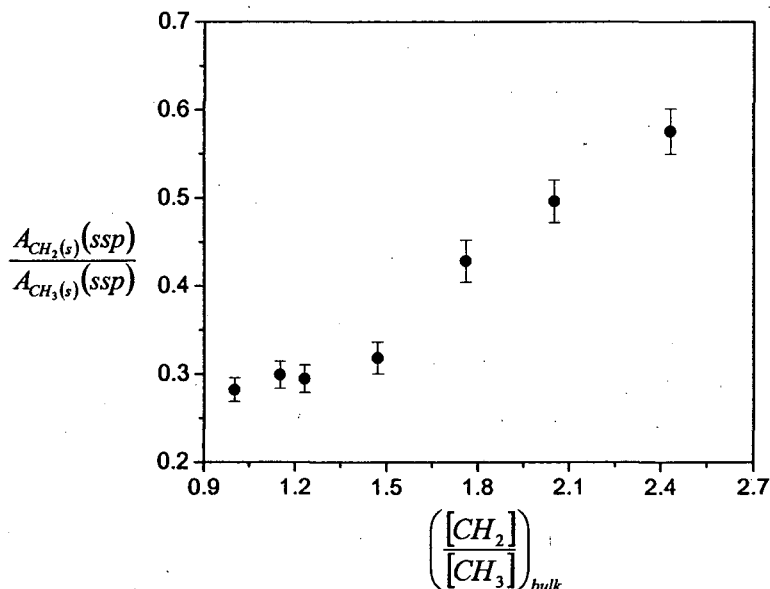
Figure 2-5: Ratio of $CH_2(s)/CH_3(s)$ ssp vibrational mode strengths (A_q) as a function of

the bulk $[CH_2]/[CH_3]$ ratio for aPP1 and the aEPR series.

In order to deconvolute the relative contributions from the number density of

molecules, n, and from the orientation average, $\langle\ \rangle$, it is necessary to understand how the

backbone CH_2 group orientation and the side branch CH_3 group orientation change as a

function of copolymer composition. The following two sections discuss these orientation

changes.

2.4 Orientation of backbone CH₂ groups

Figure 1-2 shows the expected dependence of the CH_2 vibrational mode strengths

on orientation and ordering. The mode strengths in Table 2-2 show that the ratio of the

35

the $CH_2(s)$ stretch increases relative to the $CH_2(a)$ mode stretch as ethylene concentration of the copolymer increases - an indication that the CH_2 c-axis becomes more oriented towards the surface normal as ethylene content increases. Similarly, in the *sps*, the $CH_2(s)$ mode strength increases in magnitude at high ethylene concentration supports the idea that the CH_2 symmetry c-axis orients towards the surface normal as ethylene concentration increases. The average orientation and orientation distribution of the CH_2 groups contributing to the sum frequency signal can be estimated using the $CH_2(s)$ and $CH_2(a)$ mode strengths from the *ssp* and *sps* spectra, and by knowing the relationships between the nonlinear polarizability tensor components, $\vec{a}$, for each vibrational stretch.

$$\frac{A_{CH_2(s)}(ssp)}{A_{CH_2(a)}(ssp)} = \frac{\langle \vec{a}_{CH_2(s),yyz} \rangle}{\langle \vec{a}_{CH_2(a),yyz} \rangle} = \dots \qquad (2\text{-}4)$$

$$\dots = \frac{\langle \hat{y} \cdot \hat{a} \rangle \langle \hat{y} \cdot \hat{a} \rangle \langle \hat{z} \cdot \hat{c} \rangle a_{aac} + \langle \hat{y} \cdot \hat{b} \rangle \langle \hat{y} \cdot \hat{b} \rangle \langle \hat{z} \cdot \hat{c} \rangle a_{bbc} + \langle \hat{y} \cdot \hat{c} \rangle \langle \hat{y} \cdot \hat{c} \rangle \langle \hat{z} \cdot \hat{c} \rangle a_{ccc}}{\langle \hat{y} \cdot \hat{a} \rangle \langle \hat{y} \cdot \hat{c} \rangle \langle \hat{z} \cdot \hat{a} \rangle a_{aca} + \langle \hat{y} \cdot \hat{c} \rangle \langle \hat{y} \cdot \hat{a} \rangle \langle \hat{z} \cdot \hat{a} \rangle a_{caa}}$$

For the $CH_2(s)$ stretch the nonlinear polarizability tensor has three components $(a_{aac}, a_{bbc}, \text{ and } a_{ccc})$. The nonlinear polarizability tensor for the $CH_2(a)$ stretch has two terms $(a_{aca}=a_{caa})$ which have been shown to satisfy the following relationships: [10]

$$a_{aac} \approx 5.13 a_{bbc} \approx 1.64 a_{ccc} \approx 1.24 a_{aca}$$

Using the method outlined by Hirose in reference 11 and the values for $\vec{a}$, Eq. 2-4, to a good approximation, can be shown to reduce, for the *ssp* polarization combination, to:

$$\frac{A_{CH_2(s)}(ssp)}{A_{CH_2(a)}(ssp)} = \frac{12 \cdot \langle \cos\theta \rangle + \langle \cos 2\phi \rangle (\langle \cos\theta \rangle - \langle \cos 3\theta \rangle)}{2(\langle \cos\theta \rangle - \langle \cos 3\theta \rangle)(1 + \langle \cos 2\phi \rangle)} \qquad (2\text{-}5)$$

36

Similar relationships are formed for the mode strengths from *sps* spectra and that compare the *ssp* and *sps* mode strengths. These relationships allow us to place restrictions on the average orientation and orientation distribution of CH_2 groups. In each of these expressions, the dependence on ϕ is weak, and consequently there is significant error in the determination of this angle. However, for small values of θ, the angle ϕ has little physical meaning. The angle ϕ only has physical meaning when the tilt angle θ is large. In this situation (large θ) only small SFG signals are expected. Thus in our analysis we have chosen to assume a narrow distribution for ϕ centered at 0° and we note that this assumption is less valid for large θ. This small value of ϕ constrains the average CH_2 plane perpendicular to the surface plane and maintains the average chain backbone parallel to the surface plane. Under this constraint, using Gaussian functions to describe the distribution, the remaining parameters, θ_o and $\Delta\theta$, are found to vary from 62°±8° with distribution width of 15°±7° for *a*PP1 (the copolymer with no ethylene), to 30°±11° with a distribution width of 20°±15°for *a*EPR7 (the copolymer with the highest ethylene content).

Best-fit orientation parameters for all of the copolymers are given in Table 2-3. For higher ethylenene content copolymers, the average CH_2 symmetry axis *(c)* id calculated to become more oriented towards the surface normal *(z)*. From the calculated orientation parameters, it is possible to ascertain how the *relative* value of $\langle \bar{a}_{CH_2(s),yyz} \rangle$ varies from *a*PP1 to *a*EPR7. These values are also given in Table 2-3.

Table 2-3: Best fit average orientation parameters of the CH_2 unit for the aEPR series.

	Mole fct. Ethylene	θ_o, $^\circ$	$\Delta\theta$, $^\circ$	$\left\langle \tilde{a}_{CH_2(s),yyz} \right\rangle$
aPP1	0	62±8	15±7	0.16±0.03
aEPR2	0.069	59±8	15±7	0.17±0.03
aEPR3	0.103	58±8	15±8	0.18±0.04
aEPR4	0.190	56±9	20±8	0.20±0.05
aEPR5	0.277	52±15	20±15	0.22±0.08
aEPR6	0.344	40±20	25±15	0.26±0.08
aEPR7	0.417	30±11	20±15	0.32±0.05

2.5 Orientation of side branch CH_3 groups

The analysis of the average orientation and orientation distribution of the side-branch CH_3 group is similar to the analysis of the CH_2 unit. The vibrational dipole for the $CH_3(s)$ stretch lies along the molecule symmetry c-axis, and the dipole for the $CH_3(a)$ stretch lies perpendicular to it along the molecule fixed a-axis. In the ssp spectra, the $CH_3(s)$ stretch is much larger than the $CH_3(a)$ stretch for each copolymer, thus we can infer that the average methyl symmetry axis lies more or less along the surface normal. The sps spectra supports the interpretation of an upright methyl group since the $CH_3(a)$ stretch is much larger in this polarization combination than the $CH_3(s)$ stretch. Changes in the methyl group orientation can be qualitatively assessed from ratios of the $CH_3(s)$ to $CH_3(a)$ mode strengths as a function of copolymer composition for both polarization combinations. These two ratios remain relatively unchanged as a function of ethylene concentration – which suggests that the CH_3 orientation does not dramatically change as the copolymer composition is varied.

2.6 Surface composition of aEPR series

Knowing how the CH_2 and CH_3 orientations change with bulk composition, the relationship between the $CH_2(s)$ and $CH_3(s)$ mode strengths can be evaluated. Inserting

the relative values of $\langle \tilde{a}_{q,yyz} \rangle$ into Eq. 2-3 removes orientation effects from the mode strength ratio and shows that changing the bulk ethylene mole fraction does not significantly change the ratio of CH_2 to CH_3 units *contributing to the sum frequency signal*. This indicates that as the bulk ethylene content increases, there is either an excess of CH_3 units or a depletion of CH_2 units contributing to the sum frequency signal, relative to the bulk compositions.

Relative changes in concentration of CH_3 groups contributing to the sum frequency signal as a function of bulk composition can be deduced from a direct comparison of the methyl mode strengths from Table 2-2. Since the data presented in Table 2-2 shows that the methyl orientation does not measurably change as the bulk composition varies, the change in magnitude of the CH_3 mode strengths between *a*PP1 and *a*EPR7 is assumed to arise primarily from changes in number density of CH_3 groups ordered at the interface.

Table 2-4 summarizes the *a*EPR copolymer surface methyl compositions relative to *a*PP1. The relative CH_3 concentrations are generated from the simple ratio of the $A_{CH_3(s),ssp}$ between the *a*EPR samples and the *a*PP1 reference sample. Relative surface excess values are calculated by normalizing the relative surface concentrations to the corresponding bulk composition ratio (Eq. 2-6). Relative to *a*PP1, *a*EPR7 orients ~13% fewer methyl side branches at the surface. After taking into account differences in bulk composition, however, *a*EPR7 orients a ~50% excess of methyl side branches compared to *a*PP1.

$$\left(\frac{n_{CH_3,surface}}{[CH_3]_{bulk}}\right)_{\substack{relative \\ to\ aPP1}} = \frac{\left(A_{CH_3(s)}(ssp)\Big/[CH_3]_{bulk}\right)_{aEPR}}{\left(A_{CH_3(s)}(ssp)\Big/[CH_3]_{bulk}\right)_{aPP1}} \qquad (2\text{-}6)$$

Table 2-4: Concentrations of CH_3 and CH_2 groups *contributing to the sum frequency signal*, relative to $aPP1$ (2rd and 4th columns) and surface excess/depletion values obtained after normalizing to the bulk compositions (3th and 5th columns).

Sample	CH_3 surface concentration $\left(\dfrac{n_{CH_3}(aEPRx)}{n_{CH_3}(aPP1)}\right)_{surface}$	CH_3 surface excess $\left(\dfrac{n_{CH_3(surface)}}{[CH_3]_{bulk}}\right)_{\substack{relative \\ aPP1}}$	CH_2 surface concentration $\left(\dfrac{n_{CH_2}(aEPRx)}{n_{CH_2}(aPP1)}\right)_{surface}$	CH_2 surface depletion $\left(\dfrac{n_{CH_2(surface)}}{[CH_2]_{bulk}}\right)_{\substack{relative \\ aPP1}}$
$APP1$	1	1	1	1
$aEPR2$	0.983±0.011	1.056±0.012	1.0±0.2	0.9±0.2
$aEPR3$	0.983±0.011	1.092±0.012	0.9±0.2	0.86±0.2
$aEPR4$	0.946±0.013	1.168±0.017	0.9±0.3	0.7±0.2
$aEPR5$	0.917±0.012	1.273±0.017	0.9±0.3	0.7±0.3
$aEPR6$	0.902±0.012	1.367±0.019	0.9±0.3	0.7±0.2
$aEPR7$	0.873±0.012	1.48±0.02	0.89±0.17	0.63±0.12

An excess of surface ordered methyl groups only partially accounts for the overall depletion of the $(n_{CH_2}/n_{CH_3})_{surface}$ ratio. To account for the trend in the ratio, there must also be a relative decrease in the number of backbone CH_2 units contributing to the signal. Relative CH_2 concentrations and depletions for the $aEPR$ copolymers are calculated in the same way as the CH_3 surface excesses are also presented in Table 2-4. The table shows that in addition to the CH_3 surface excess, $aEPR7$ has a relative depletion of about 30% of CH_2 groups contributing to the sum frequency signal.

This does not necessarily mean that there are fewer CH_2 units present at the surface. A decrease in CH_2 units contributing to the SFG signal can also be accounted for by *trans* cancellation of neighboring CH_2 groups. Because the CH_2 units become more ordered with the c-axis towards the surface normal, indicates that the chain backbones

tend to lie somewhat in the surface plane. Thus many of the chain segments at the surface are likely in a *trans* configuration, and it is more possible that there is a depletion of contributing CH_2 groups as a result of some sort of cancellation process.

In the extreme case, where every ethylene unit at the surface is in a *trans* configuration, and complete *trans* cancellation occurs, all of the SFG signal from the ethylene units would cancel and only SFG signal arising from the propylene units at the surface would be measured. If this were the case and the surface were comprised of a statistical mixture of CH_2 and CH_3 groups, n_{CH_2} contributing to the sum frequency signal would be invariant with respect to bulk composition. Taking into account the surface excess of n_{CH_3} as the bulk ethylene concentration increases, would lead to an overall negative dependence of $\left(n_{CH_2} / n_{CH_3} \right)_{surface}$ on the bulk composition. That this is not observed in indicates that at most there can be only a partial cancellation of ordered CH_2 groups at the surface leading to a slightly reduced CH_2 intensity for the ethylene containing copolymers.

2.7 Discussion

The preceding analysis of the SFG spectra places significant restrictions on the average orientation of CH_2 and CH_3 units at the surface and thus on the possible conformations of the *a*EPR chain segments at the air-polymer interface. A schematic, showing the primary differences in surface chain segment configurations for *a*PP1 and *a*EPR7, is presented in Figure 2-6.

41
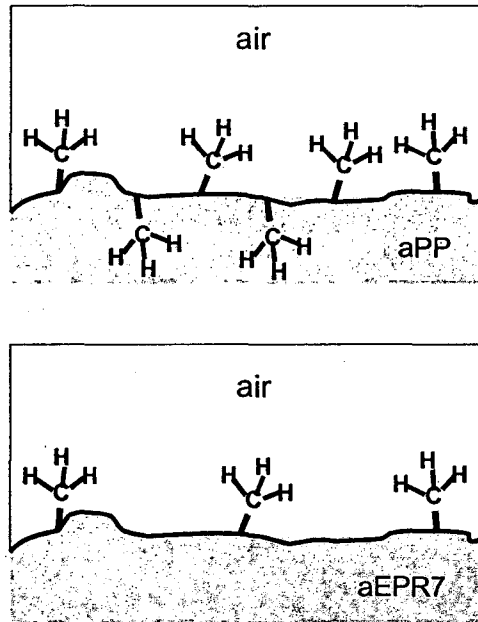
Figure 2-6: Schematic of proposed structures of *a*PP1 and *a*EPR7 surfaces.

Although *a*PP1 has more methyl branches ordered at the interface than *a*EPR7, steric hindrances between adjacent methyl branches may prevent *a*PP1 from orienting every methyl branch away from the surface. In the *a*PP polymer segment shown, we have oriented four of the six methyl branches out of the surface. The two remaining methyl branches are randomly oriented or oriented towards the bulk. By preferentially ordering the methyl branches, the orientation of the CH_2 backbone units is restricted. The backbone CH_2 groups are required to orient with larger, possibly more random, tilt angles. Steric hindrances between adjacent methyl groups are reduced by the incorporation of ethylene in the backbone, and the *a*EPR polymers can order a higher percentage of methyl groups at the surface. In the schematic *a*EPR7 polymer segment shown, all of the methyl groups are oriented away from the surface.

These surface configurations are supported by simulations of the atactic polypropylene (*a*PP) surface performed by Mansfield and Theodorou,[12] and of the

polyethylene (PE) surface performed by Mattice.[13] Both simulations predict that chain backbones near the surface (top 5-10 Å) tend to lay in the surface plane, maximizing the cohesive energy between the polymer units at the surface and in the bulk. For *a*PP, the simulations also predicted that the methyl side groups are oriented upright at the interface. Comparing between the two polymers, the calculated order parameter for the backbone C-C bond direction is smaller for *a*PP than PE. This may indicate that PE has longer runs of chain segments in the surface plane and that it may have a higher number density of chain segments in a *trans* configuration at the surface than *a*PP.

The phenomenon of orienting methyl groups away from the surface has several possible explanations. The first is that air is generally considered a hydrophobic media, and thus the more hydrophobic methyl groups should be attracted to the interface. The second is that the low density on the air-side of the interface may favor a configuration where the polymers extend bulky side groups away from the surface. The effect may be suppressed at solid interfaces. Theoretical calculations of aPP at the air/graphite interface suggest that the ordering of methyl groups at this interface is much lower than the air/polymer interface.[14] The results presented in Chapter 4 suggest that methyl branches restructure at the aPP/water interface. Experimental evidence on the polymethacrylate polymers[15] and polystyrene[4] also suggests that preferential ordering of side groups can be suppressed at the polymer/liquid and polymer/solid interfaces.

The tendency to order side branches out of the surface may also give some additional insight into the higher surface activity of branched polyolefins. In blends of branched polyolefins, presented in Chapter 5 and 6. There is typically an enrichment of the component with the higher degree of branching at the air/polymer interface.[1,16]

Explanations have been given based on the lower cohesive energy (and lower surface tension) of the higher branched component.[1] The results of this Chapter give additional physical insight into the specific interactions at the air/polymer interface that tend to order the side branches out of the surface.

2.8 Conclusion

Sum frequency generation vibrational spectroscopy has been used to quantify the effect of branching on the surface chain conformation of a series of aspecific ethylene-propylene copolymers. The results show that methyl side branches prefer to orient away from the surface regardless of copolymer composition. The incorporation of ethylene units decreases the steric hindrance between adjacent methyl groups. The reduced steric effects are proposed to allow ethylene-rich copolymers to assume configurations that orient a surface excess of methyl groups away from the surface. Increasing the number of ethylene units in the backbone also allows the CH_2 units in the backbone to orient with their symmetry axis along the surface normal.

Acknowledgment

References

[1] F. Scheffold, A. Budkowski, U. Steiner, E. Eiser, J. Klein, L.J. Fetters *J. Chem. Phys.* 1996, *104*, 8795.

[2] Zhang, D.; Shen, Y.R.; Somorjai, G.A. *Chem. Phys. Lett.* 1997, *281*, 394.

[3] Gautam, K.S.; Schwab, A.D.; Dhinojwala, A.; Zhang, D.; Dougal, S.M.; Yeganeh, M.S. *Phys. Rev. Lett.* **2000**, *85*, 3854.

[4] Briggman, K.A.; Stephenson, J.C.; Wallace, W.E.; Richter, L.J. *J. Phys. Chem. B* **2001**, *105*, 2785.

[5] Oh-e, M.; Lvovsky, A.I.; Wei, X.; Shen, Y.R. *J. Chem. Phys.* **2000**, *113*, 8827.

[6] Resconi, L.; Jones, R.L.; Rheingold, A.L.; Yap, G.P. *Organometallics* **1996**, *15*, 998.

[7] Koenig, J.L.; <u>Chemical Microstructure of Polymer Chains</u>, John Wiley & Sons, New York, **1982**.

[8] Wei, X.; Hong, S.C.; Zhuang, X.W.; Goto, T.; Shen, Y.R. *Phys. Rev. E* **2000**, *62*, 5160.

[9] Miranda, P.B.; Shen, Y.R. *J. Phys. Chem. B* **1999**, *103*, 3292.

[10] Zhuang, X.; Miranda, P.B.; Kim, D.; Shen, Y.R. *Phys. Rev. B* **1999**, *59*, 12632.

[11] Hirose, C.; Akamatsu, N.; Domen, K. *Appl. Spect.* **1992**, *46*, 1051.

[12] Mansfield, K.F.; Theodorou D.N. *Macromolecules* **1990**, *23*, 4430.

[13] He, D.Y.; Reneker, D.H.; Mattice, W.L. *Polymer* **1997**, *38*, A19.

[14] Mansfield, K.F.; Theodorou, D.N. *Macromolecules* **1991**, *24*, 4295.

[15] Wang, J.; Woodcock, S.E.; Buck, S.M.; Chen, C.; Chen, Z. *JACS* **2001**, *ASAP Article*.

[16] Opdahl, A.; Phillips, R.A.; Somorjai, G.A.; *Macromolecules* **2002**, 35, 4387.

Chapter 3

Solvent vapor induced ordering and disordering of polymer interface studied by SFG

3.1 Introduction

Chapters 3 and 4 describe experiments aimed at understanding the structure of polymer/liquid interfaces. This chapter explores the effects that the absorption of toluene vapor into polystyrene has on the ordering of phenyl side-branches at the polystyrene/toluene vapor interface. The mobility of the surface region of a polymer is particularly important when considering how a polymer surface responds to changes in environment. Experimental research on polystyrene and polystyrene derivatives by AFM[1], Brillouin light scattering[2], and contact angle experiments[3] report enhanced mobility at the air/polymer interface; most notable is the phenomenon of a depressed glass transition temperature (T_g) in the surface region (T_g bulk ~110°C). Recent studies indicate that when placed in contact with water, that on

a short time scale, rubbery methacrylate polymers reconfigure themselves in response to the liquid, while glassy methacrylate polymers do not.[4] In addition, when polymer blends and block copolymers are exposed to solvent, preferential solvation has been shown to affect the chemical composition of the surface region.[5]

Chapters 1 and 2 presented many examples of SFG spectra obtained from polymer/air interfaces showing that the spectra are highly sensitive to ordering of side branches at an interface.[6] At the air interface, a number of SFG studies have shown that hydrophobic side branches are well-ordered and are oriented away from the polymer bulk.[6,7,8,9,10,11] Two factors are related to this observation: (1) air is considered hydrophobic, thus hydrophobic side branches should be favored and (2) the low density air interface (an increase in free volume) may favor a large concentration of bulky side branches in the top few Angstroms of the interface region.[12] At the polymer/liquid interface, the change in density between the polymer phase and the liquid phase is not as great as at the polymer/air interface, so density effects may not play as large a role. Additionally, interactions between the liquid and the polymer may become important. This is relevant for the case of polystyrene exposed to toluene vapor, where the toluene vapor is expected to swell the glassy polystyrene film and increase the mobility of the polymer chains.

3.2 Experimental procedures

Polystyrene films were prepared by spin casting 5% weight solutions of polystyrene (M.W. 550,000; polydispersity 1.01; Scientific Polymer) in toluene (Aldrich, 99.5% spec grade) and in deuterated (d_8) toluene (Aldrich, 99.5% spec grade) onto IR grade fused silica substrates. After casting, the films were annealed at

110°C for 12 hours and cooled at ~1°C/min back to room temperature. All SFG measurements were made within 12 hours after the films were annealed.

Surface vibrational spectra were obtained using the experimental setup described in Chapter 1. The intensity of the sum-frequency signal is described by Equation 3-1 and is proportional to the square of the second order non-linear susceptibility of the excited medium, $\chi^{(2)}$ (Eq.1).[13] For vibrationally resonant SFG - resonant enhancement (A_q) occurs when the infrared source (ω_{IR}) is tuned near a vibrational mode(ω_q). Spectra were collected using the $s_{sum}s_{vis}p_{ir}$ polarization combination, which probes the lab-fixed yyz component of A_q. This polarization combination is most sensitive to vibrations that have a component of the vibrational dipole (μ_k) along the surface normal, z, and a component of the polarizability tensor (α_{ij}) in the surface plane (x-y). SFG spectra were collected in air and under saturated solvent vapor using the configuration shown in Figure 3-1.
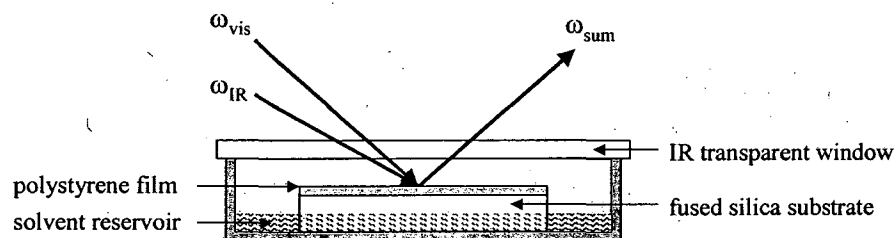
Figure 3-1: Schematic of experimental setup showing a polystyrene film elevated above a solvent reservoir in an enclosed cell. The incoming beams (ω_{vis} and ω_{IR}) pass through the window and mix on the polymer film to generate ω_{sum}, which is measured in a reflection geometry.

3.3 Results and Discussion

An SFG spectrum ($s_{sum}s_{vis}p_{ir}$ polarization combination, normalized to IR power) of a polystyrene film spin cast from toluene and then annealed at 110°C for 12 hours is shown in Figure 3-2a. The spectrum is qualitatively similar to those presented by Zhang[8], Gautam[9], Briggman[10], and Oh-e[11] where the dominant feature is the symmetric $v2$ stretch from the aromatic side group at ~3060cm^{-1}. Although there has been some discrepancy as to the exact orientation of the phenyl side branch at the surface, at a basic level this SFG spectrum indicates that the phenyl side branches are preferentially ordered with an upright orientation at the polystyrene/air interface. This is in agreement with recent theoretical calculations predicting that the phenyl side branch should be oriented away from the polymer bulk at the surface.[14]

Figure 3-2b shows an SFG spectrum of the surface of liquid toluene – a good solvent for polystyrene. This spectrum is quite different from the SFG spectrum of polystyrene. In particular, the intensity of the phenyl peak at 3060cm^{-1} is dramatically reduced. Additionally, there is a feature at 2925cm^{-1}, which can be assigned as the $CH_3(s)$ stretch.[15] Because the methyl group and phenyl group of toluene share the same C_v symmetry axis - if the $CH_3(s)$ stretch is present in the SFG spectra, then the symmetric $v2$ stretch from the aromatic group should also be present.

For both of these vibrational modes (the methyl $CH_3(s)$[6] and the phenyl $v2$ [9] modes), the SFG signal will be strongest in the $s_{sum}s_{vis}p_{ir}$ spectra if the toluene C_v symmetry axis is along the surface normal z-axis (in either orientation: phenyl pointed up or methyl pointed up). The strong $CH_3(s)$ mode relative to the $CH_3(a)$ mode (~2970cm^{-1}) indicates that the average orientation of C_v axis of the ordered

toluene molecules is along the surface normal. However, the absolute intensities of the $CH_3(s)$ and the aromatic $v2$ modes are relatively weak, suggesting that the toluene molecules are much more randomly oriented at the air interface as compared to polystyrene.[16]
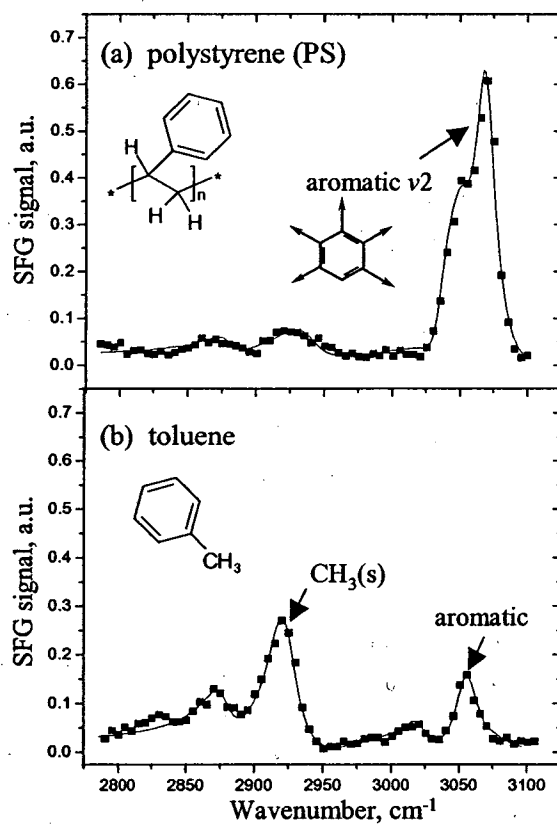
Figure 3-2: SFG spectra ($s_{sum}s_{vis}p_{ir}$ polarization) of (a) a spin-cast polystyrene film annealed for 12 h at 110°C and (b) the surface of liquid toluene.

To study the effect that toluene solvent vapor has on the surface of polystyrene, polystyrene films were placed under a vapor pressure of toluene (22 torr at 20°C) using the setup described in Figure 3-1 and then given at least 30 minutes for the solvent vapor to penetrate the film.[17] Figure 3-3a shows the SFG spectrum of the polystyrene film exposed to toluene vapor. This SFG spectrum is similar to the SFG spectrum of pure toluene shown in Figure 3-2b indicating that it is likely that toluene is ordered at the interface. Most of the spectral features of toluene overlap with the features of polystyrene, however, making it difficult to separate the SFG signal contributions coming from the toluene and from the polystyrene.

Figure 3-3b shows the SFG spectrum of a polystyrene film exposed to fully deuterated (d_8) toluene. The use of deuterated toluene removes the spectral interferences with polystyrene. In this situation very little sum-frequency signal is generated in the C-H stretching region, indicating that the deuterated toluene preferentially coats the surface and disrupts the ordering of the polystyrene molecules. This spectrum also indicates that the majority of the signal in Figure 3-3a comes from the toluene and that toluene covers the surface of polystyrene in all cases. Figure 3-3c shows the SFG spectrum of a polystyrene film taken after allowing the toluene to evaporate from the film at room temperature and pressure. Interestingly, the SFG spectrum of the polystyrene film taken after the toluene evaporated is very similar to that of the annealed polystyrene film shown in Figure 3-2a. This indicates that phenyl side groups from the polystyrene rapidly reorder at the air-polymer interface as the solvent molecules leave the film. There is no evidence of residual solvent at the interface, meaning that the interaction between the solvent and the

polymer is not strong enough to keep a significant quantity of the solvent around at the surface.
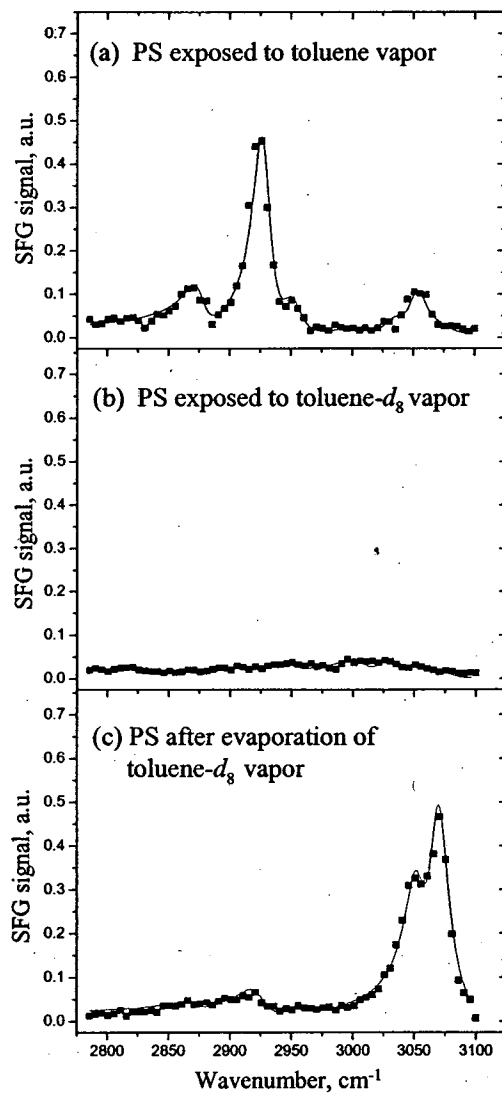
Figure 3-3: SFG spectra ($s_{sum}s_{vis}p_{ir}$ polarization) of (a) a polystyrene film exposed to toluene vapor, (b) a polystyrene film exposed to d_8-toluene vapor and (c) a polystyrene film after the deuterated toluene is allowed to evaporate.

A schematic representation comparing the polystyrene/air interface to the solvated polystyrene/toluene vapor interface is shown in Figure 3-4. The observation that the toluene molecules preferentially order at the polystyrene/toluene vapor interface can be understood by the relative difference in surface tension of the two components - the toluene solvent molecules have a much lower surface tension than polystyrene (27dyne/cm[18] vs. 40dyne/cm[19]). Thus the system can be thought of as a miscible blend where the low surface tension toluene component wets the surface of the polystyrene. The toluene molecules penetrate and solvate the polystyrene surface and bulk, and the ordering of the polystyrene phenyl groups that were originally at the air interface is lost.

We have observed the same disordering effect using chloroform vapor, which is also a good solvent for polystyrene, but has a higher vapor pressure at room temperature (160 torr at 20°C). A similar type of solvent induced disordering effect has been published by Zolk[20], which is focused on the interactions of a hydrophilic-capped, alkane self-assembled monolayer with water and with carbon tetrachloride. In that example, the authors observe that water solvates the hydrophilic end group, while carbon tetrachloride penetrates into the hydrophobic backbone and disrupts the ordering of the entire chain.
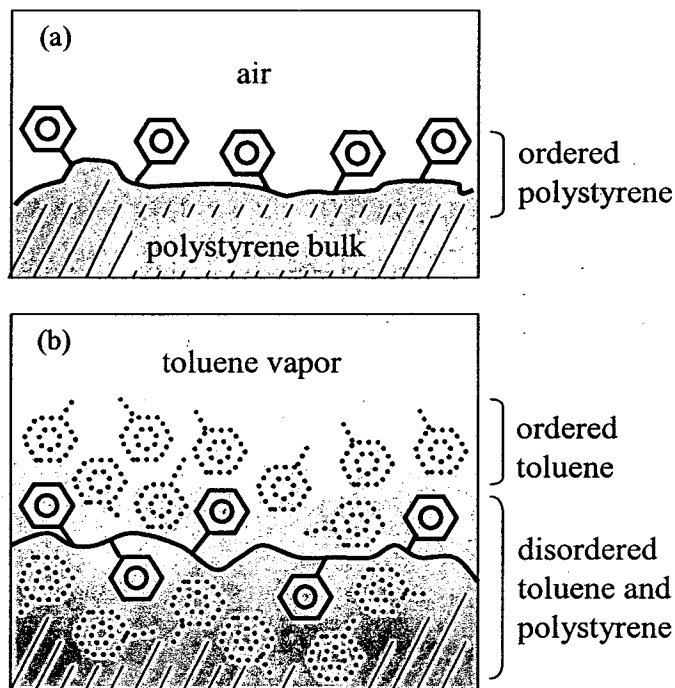
Figure 3-4: Schematic representations of (a) the polystyrene/air interface and (b) the solvated polystyrene/toluene vapor interface showing toluene (dotted) coating the surface and disordering the underlying polymer.

An interesting observation is that when the solvent evaporates, the polystyrene phenyl side-branches immediately reconfigure at the surface into a conformation that is identical, by SFG, to the surface conformation of the initial annealed film - even though the bulk structures of the annealed and solvent evaporated films are different. The solvent evaporated film is expected to have a more expanded chain conformation than the annealed film.[21] For bulk polystyrene, full restructuring of the side branches at the surface would be associated with T_g, behavior (long range coordinated motions) although partial reconstruction could be associated with T_β behavior (short range

coordinated motions). Both transitions are above room temperature for bulk polystyrene (~100°C and ~50°C, respectively).[22]

An explanation for the observed reordering is that as the solvent evaporates, the polystyrene surface is partially solvated and is highly mobile. Another possibility is that T_g and T_β for the polystyrene chains at the interface may be significantly low enough to allow for restructuring to occur under ambient conditions. Initial experiments on vacuum dehydrated polystyrene, where the solvent evaporation time is greatly reduced, show much more random surfaces at room temperature, suggesting that the restructuring effect we have measured is due primarily to enhanced mobility from the solvent and that the surface T_g and T_β transitions are not reduced enough to allow complete surface restructuring at room temperature.

The polystyrene/toluene vapor system represents the extreme case of a polymer in contact with a liquid, where the liquid completely solvates the interface. The next Chapter investigates interactions between polymer surfaces and vapors/liquids that are poor solvents (atactic polypropylene exposed to methanol for example), where an ordered interface is formed between the molecules in the liquid phase and the polymer surface.

3.4 Conclusion

Sum Frequency Generation (SFG) vibrational spectroscopy has been used to characterize the effect that solvent vapor has on the surface structure of polystyrene films. SFG spectra indicate that, in a saturated toluene vapor environment, low surface-tension toluene molecules preferentially coat and solvate/disorder the polystyrene films. The SFG spectra indicate that phenyl side branches are well-

ordered at the air/polystyrene interface prior to toluene exposure, and reorder when removed from the solvent vapor - due to high mobility of the partially solvated surface.

References

[1] Takana, K.; Takahara, A.; Kajiyama, T. *Macromolecules*, **2000**, *33*, 7588.

[2] Forrest, J.A.; Dalnokiveress, K.; Dutcher, J.R. *Phys. Rev. E*, **1997**, *56*, 5705.

[3] Rouse, J.H.; Twaddle, P.L.; Ferguson, G.S. *Macromolecules*, **1999**, *32*, 1665 and Tretinnikov, O.N. *Langmuir*, **2000**, *16*, 2751.

[4] Wang, J.; Woodcock, S.E.; Buck, S.M.; Chen, C.; Chen, Z. *J. Amer. Chem. Soc.*, **2001**, *123*, 9470.

[5] Chen, J.X.; Zhuang, H.Z.; Zhao, J.; Gardella, J.A. *Surf. and Int. Anal.*, **2001**, *31*, 713.

[6] Opdahl, A.; Phillips, R.A.; Somorjai, G.A. *J. Phys. Chem B*, **2002**, *106*, 5212.

[7] Wang, J.; Chen, C.; Buck, S.M.; Chen, Z. *J. Phys. Chem. B*, **2001**, *105*, 12118.

[8] Zhang, D.; Dougal, S.M.; Yeganeh, M.S. *Langmuir*, **2000**, *16*, 4528.

[9] Gautam, K.S., Schwab, A.D.; Dhinojwala, A.; Zhang, D.; Dougal, S.M.; Yeganeh, M.S. *Phys. Rev. Lett.*, **2000**, *85*, 3854.

[10] Briggman, K.A.; Stephenson, J.C.; Wallace, W.E.; Richter, L.J. *J. Phys.Chem. B*, **2001**, *105*, 2785.

[11] Oh-e, M.; Hong, S.C.; Shen, Y.R. *Appl. Phys. Lett.*, **2002**, *80*, 784.

[12] Mansfield, K.F.; Theodorou, D.N. *Macromolecules* **1990**, *23*, 4430.

[13] Wei, X.; Hong, S.C.; Zhuang, X.W.; Goto, T.; Shen, Y.R. *Phys. Rev E*, **2000**, *62*, 5160.

[14] Clancy, T.C.; Hwan Jang, J.; Dhinojwala, A.; Mattice,W.L. *J. Phys. Chem. B*, **2001**, *105*, 11493.

[15] Xie, Y.; Boggs, J.E. *J. Comp. Chem.*, **1986**, *7*, 158.

[16] To quantitatively compare the intensities of the toluene and the polystyrene SFG spectra, differences in Fresnel coefficients must be accounted for (see ref. 13). However, since the refractive index of toluene (n=1.4961; *CRC Handbook of Chemistry and Physics*, 80th ed, CRC Press, OH) is similar to that of polystyrene (n=1.5129; V. Galiatsatos et al., in *Physical Properties of Polymers Handbook*, ed. by J.E. Mark, AIP Press, NY, Chapter 39, **1996**) the correction is small – direct comparison of intensities for qualitative purposes is reasonable.

[17] The 30 min equilibration period is based on an estimate of 0.1nm/s rate of diffusion of toluene in polystyrene. For discussion of diffusion rates see: Gall T.P.; Kramer, E.J. *Polymer*, **1991**, *32*, 265.

[18] Froba, A.P.; Leipertz, A. *Int. J. Thermophys.*, **2001**, *22*, 41.

[19] Wu, S. in *Polymer Handbook - 4th edition*, ed. by J. Brandup, E.H. Immergut, and E.A. Grulke, John Wiley and Sons Inc., New York, 521, **1999**.

[20] Zolk, M.; Eisert, F.; Pipper, J.; Herrwerth, S.; Eck, W.; Buck, M.; Grunze, M. *Langmuir*, **2000**, *16*, 5849.

[21] Sasaki, T.; Tanaka, M.; Takahashi, T. *Polymer*, **1998**, *39*, 3853.

[22] Fried, J.R. in *Physical Properties of Polymers Handbook*, ed. by J.E. Mark, AIP Press, Woodbury, NY, Chapter 13, 161, **1996**.

Chapter 4

Ordered interfaces formed between atactic polypropylene (*a*PP) surfaces and polar vapors and liquids

4.1 Introduction

This chapter expands on the observation that solvents disrupt ordering at polymer interfaces, and uses SFG vibrational spectroscopy to characterize the structure of well-defined interfaces formed between atactic polypropylene (*a*PP), which is nonpolar and is rubbery at room temperature, and polar liquids which are not miscible with *a*PP. Detailed knowledge of the variables that influence the molecular structure of buried polymer/liquid interfaces is important for understanding interface specific processes including adhesion, wetting, and adsorption. One example is the commonly observed 'contact angle hysteresis' between the advancing and retreating angles of a liquid droplet on a solid surface. Many factors are thought to contribute to contact angle hysteresis including surface roughness, surface chemical heterogeneity, mechanical properties, and

miscibility of the two contacting materials.[1,2,3] For polymers, it is also generally believed that molecular restructuring events between the polymer/air and polymer/liquid interfaces play a role in this phenomenon. In order to determine the degree to which restructuring influences a phenomenon like contact angle hysteresis, it is necessary to have experimental measurements of the structures of polymers at both air and liquid interfaces. Many experimental techniques exist for studying buried polymer/liquid interfaces - few are capable of providing direct molecular level information of the interaction between the polymer and liquid phases. Sum frequency generation (SFG) vibrational spectroscopy has developed as an experimental technique capable of providing molecular structure information of both open and buried polymer interfaces.[4]

For many polymers, SFG vibrational spectroscopy has been shown to be highly sensitive to ordering of polymer side branches at an interface.[5,6,7,8,9,10] At open air interfaces, studies have shown that bulky hydrophobic side branches are generally ordered and oriented away from the polymer bulk - in agreement with theoretical predictions.[11,12] Efforts have been made to study the behavior of polymers at solid and liquid interfaces using SFG vibrational spectroscopy.[13,14] Wilson et al. have shown that polystyrene adapts different configurations when it is in contact with hydrophobic and with hydrophilic solids.[14] Polymer mobility has been shown to be an important parameter when considering how quickly a polymer surface responds when it is placed in contact with a liquid. Wang et al. have shown that when placed in contact with water, that on a short time scale, the surfaces of rubbery methacrylate polymers restructure in response to the water, while the surfaces of glassy methacrylate polymers do not.[15]

Miscibility of the polymer and liquid phases affects the interface structure. When polymer blends and block copolymers are exposed to solvent, preferential solvation can affect the chemical composition of the surface region.[16] An example is presented in Chapter 6. The previous chapter showed results indicating that polymer surfaces disorder when they are exposed to solvent vapor.[17] In this chapter SFG vibrational spectroscopy has been used to characterize the structure of well-defined interfaces formed between aPP and polar liquids (methanol, acetonitrile, and water) - using the experimental geometry shown in Figure 4-1.

4.2 Experimental procedures

Polymer films Atactic polypropylene (aPP) films were prepared by spin casting 5% weight solutions of polypropylene (M.W. 50,000; polydispersity ~2.0; Basell Polyolefins) in n-hexane (Aldrich, 99.5% spec grade) onto IR grade fused silica substrates. Further description of the physical properties of the aPP used in this study is given in Chapter 2. After casting, the films were annealed at 70°C for 12 hours and slowly cooled to room temperature. The methanol, deuterated methanol (99.8% deuterated), acetonitrile, and deuterated acetonitrile (99.8% deuterated) were purchased from Aldrich.

SFG vibrational spectroscopy Surface vibrational spectra of aPP films were obtained at the polymer/saturated vapor and polymer/liquid interfaces using the experimental setup described in Chapter 1 and the configuration shown in Figure 4-1. In this geometry, the incidence angles of the co-propagating visible and tunable infrared laser pulses overlapped at the polymer/air(liquid) interface were ~30° and 35°, respectively, from the surface normal and the induced sum-frequency signal was

measured in the reflected direction. The intensity of the sum-frequency signal is described by Equation 4-1 and is proportional to the square of the second order non-linear susceptibility of the excited medium, $\chi^{(2)}$.

$$I(\omega_{sum}) \propto \left| \chi^{(2)} \right|^2 = \left| \chi_{NR} + \sum_q \frac{A_q}{\omega_{IR} - \omega_q + i\Gamma_q} \right|^2 \qquad (4\text{-}1)$$
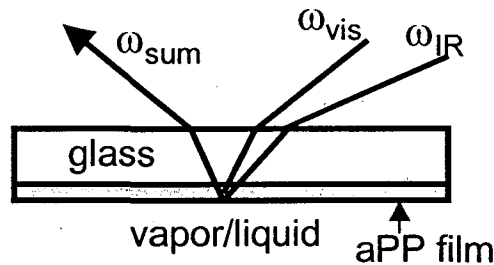
Figure 4-1: Schematic of setup used for the SFG experiments showing a polypropylene film exposed to vapor or liquid molecules. The incoming beams (ω_{vis} and ω_{IR}) pass through the glass window and mix at the polypropylene/liquid (or vapor) interface to generate ω_{sum}, which is measured in a reflection geometry.

Experiments similar to those described in reference 15, comparing the SFG signal generated from thick polymer films to the SFG signal generated from thin polymer films, were carried out in order to determine the origin of the SFG signal using the setup shown in Figure 4-1. Thick films (several microns) attenuate much of the intensity of the infrared beam as the light passes through it, and any measured SFG signal should originate from the polymer/glass interface and the polymer bulk. In our experiments, we measure very little SFG signal using thick films, indicating that the dominant SFG signal we are measuring originates from the polypropylene/air(liquid) interface. Additionally,

for the vapor experiments, qualitatively similar results are obtained if the sample is face up as presented in the previous chapter.

4.3 Results

Polypropylene/air The SFG spectrum ($s_{sum}s_{vis}p_{iR}$ polarization combination, normalized to IR power) of a polypropylene film spin cast from *n*-hexane (same as that presented in Chapter 2) is shown in Figure 4-2a. The spectrum has been fit to Eq. 4-1 using 5 vibrationally resonant features. The features at ~2850cm^{-1} and ~2920cm^{-1} are assigned as the CH_2 symmetric ($CH_2(s)$) and antisymmetric ($CH_2(a)$) stretches, respectively, from the polymer backbone. Features at ~2880cm^{-1} and the shoulder at ~2965cm^{-1} are assigned to the CH_3 symmetric ($CH_3(s)$) and antisymmetric ($CH_3(a)$) stretches from the methyl side branch. An additional feature at ~2940cm^{-1} has been attributed to a Fermi resonance between the $CH_3(s)$ and an overtone of the CH_3 antisymmetric bending mode. The large $CH_3(s)$ vibration relative to the $CH_3(a)$ vibration was interpreted as indicating that side branch methyl groups are preferentially ordered at the interface and that the ordered side branches are oriented more or less directly out of the interface.

Polypropylene/methanol interface Figure 4-2b shows an SFG spectrum of the methanol liquid/vapor interface. The feature at 2830cm^{-1} has been assigned as the $CH_3(s)$ and the features at 2920cm^{-1} and 2940cm^{-1} have been assigned as Fermi resonances between the $CH_3(s)$ stretch and overtones of the CH_3 bending vibrations.[18] Previous SFG studies of methanol have determined that the methanol molecules at the liquid/vapor interface are oriented with the methyl group pointing towards the vapor phase. Methanol is a poor solvent for polypropylene. To study the structure of the *a*PP/methanol interface,

*a*PP films were exposed to a vapor pressure of methanol (~150torr) at room temperature and spectra were collected using the setup described by Figure 4-1. Figure 4-2c shows the SFG spectrum of an *a*PP film exposed to methanol vapor. Solid lines in the spectra represent the result of a best fit to Eq. 4-1.
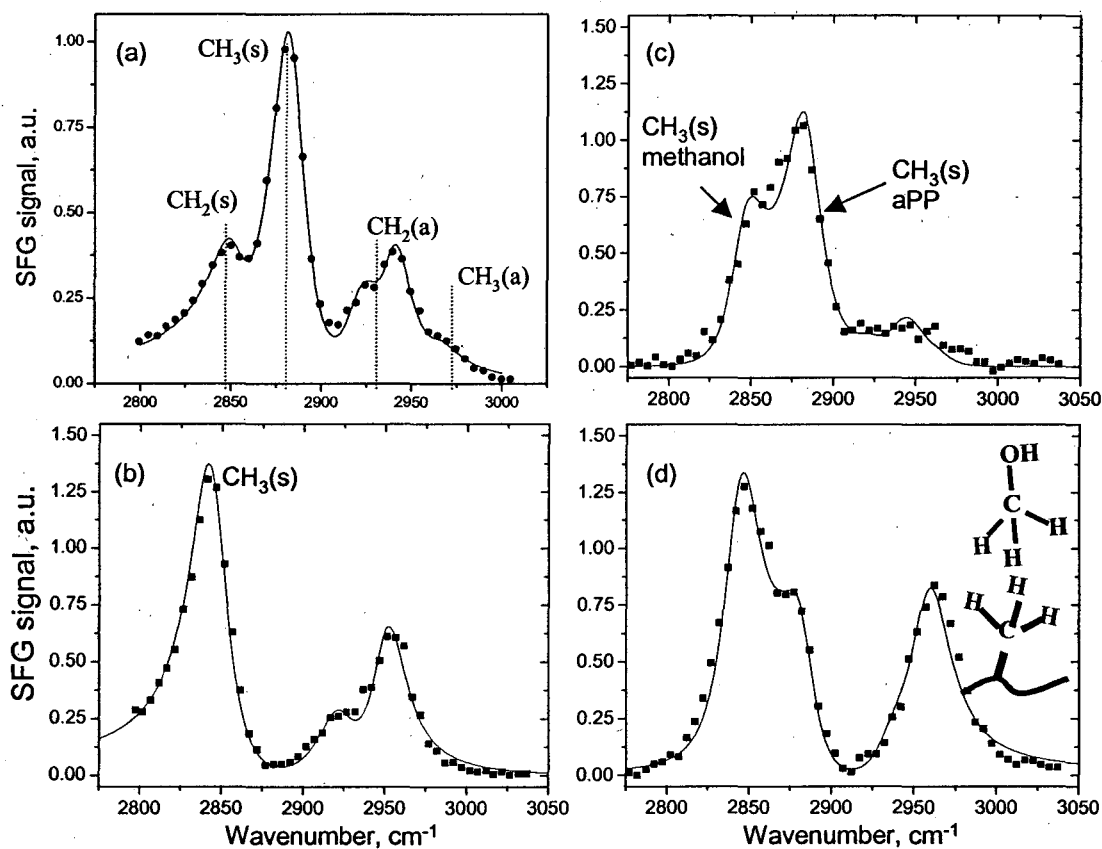
Figure 4-2: SFG spectra of (a) *a*PP/air interface (b) methanol liquid/vapor interface (c) *a*PP/methanol vapor interface (d) *a*PP/methanol liquid interface. All spectra were collected using the *ssp* polarization combination. Solid lines represent the results of a best fit of the data to Eq. 4-1.

For the spectrum of *a*PP exposed to methanol, the best fit is obtained using a combination of the peak assignments from *a*PP and from methanol. The mode

63

amplitudes, A_q, in Eq. 4-1 can have a positive or a negative value, depending on the orientation of the molecular group, and the resonant features in an SFG spectrum can constructively or destructively interfere with one another. Interferences between modes can be a useful way of determining the relative orientations of different species at an interface. For $CH_3(s)$ vibrations measured using the *ssp* polarization combination, the mode amplitude will change sign depending on whether the CH_3 groups are oriented towards or away from the surface. Using the fit parameters for aPP obtained from the aPP/deuterated methanol interface, the best fit spectra in Figure 4-2c is obtained if A_q for the $CH_3(s)$ stretch from methanol has *opposite* sign as A_q for the $CH_2(s)$ and $CH_3(s)$ stretches from the aPP. Unfortunately, we do not know the thickness of the adsorbed layer (monolayer, mulitlayer, or thick condensed layer) in this situation. If it is a thin multilayer of methanol we expect partial cancellation of the SFG signal arising from the methanol oriented at the aPP in contact with the aPP and from the methanol in contact with air. If it is a thick multilayer (>20nm), we expect thickness dependent interference effects between the two interfaces. Based on the lower surface tension of methanol, compared to aPP, and that we are under saturated vapor conditions, we expect a condensed layer.

Analysis of SFG spectra obtained from the aPP/methanol liquid interface is less ambiguous. An SFG spectrum collected from aPP in direct contact with methanol liquid is shown in Figure 4-2d. In this spectrum, the contribution from methanol is larger, relative to the aPP/methanol vapor spectrum in Figure 4-2c. The solid line in Figure 4-2d represents the result of a best fit to Eq. 4-1 obtained by giving the A_q from the methanol $CH_3(s)$ stretch opposite sign as the A_q from the $CH_2(s)$ and $CH_3(s)$ vibrations from aPP.

The lower intensity of the CH_3 stretch from aPP relative to the aPP/methanol vapor spectra in Figure 4-2c can be reasonably accounted for by the differences in Fresnel coefficients (see Chapter 1) for the polymer/vapor and polymer/liquid interfaces. This result confirms that at the aPP/methanol liquid interface, the CH_3 groups from methanol are oriented towards the CH_3 side branches from aPP. The relative fit parameters for aPP are similar for both SFG spectra (Figure 4-3b and 4-3d) indicating that the configuration of aPP at the interface does not measurably change under exposure to methanol vapor and liquid.

Polypropylene/acetonitrile interface Figures 4-3a shows an SFG spectrum of the acetonitrile liquid/vapor interface. Acetonitrile is also a poor solvent for polypropylene. Previous SFG studies of the acetonitrile liquid/vapor interface have shown that the methyl ends are ordered at the interface.[19] For acetonitrile, the peak at ~2950cm^{-1} has been assigned as the CH_3(s) stretch. SFG spectra of aPP in contact with acetonitrile vapor, with deuterated acetonitrile vapor, and with acetonitrile liquid are shown in Figures 4-3b, 4-3c, and 4-3d, respectively. The SFG spectrum of the aPP film exposed to deuterated acetonitrile vapor is similar to the spectra of aPP at the air interface, showing that the structure of aPP does not measurably change from its structure in air when it is placed in contact with acetonitrile.

The spectrum of acetonitrile vapor in contact with aPP, Figure 4-3b, shows an increase in the feature at 2950cm^{-1}, indicating that acetonitrile and aPP form an ordered interface. Interference between the CH_3(s) vibration from aPP and the CH_3(s) vibration from acetonitrile is less obvious than it is for the aPP/methanol spectra, largely because the CH_3(s) vibrations from aPP and acetonitrile are well separated. However, the solid

lines in Figures 4-3c and 4-3d represent best fits and are generated using opposite signs for the amplitudes of the $CH_3(s)$ mode strength from aPP and the $CH_3(s)$ mode strength from acetonitrile, indicating that the methyl groups from aPP and acetonitrile face one another at the interface. When placed in direct contact with liquid acetonitrile, the $CH_3(s)$ stretch from acetonitrile dominates the spectra. The acetonitrile $CH_3(a)$ stretch is absent in both vapor and liquid spectra, indicating that there is no measurable orientation change in the acetonitrile molecules at the interface.
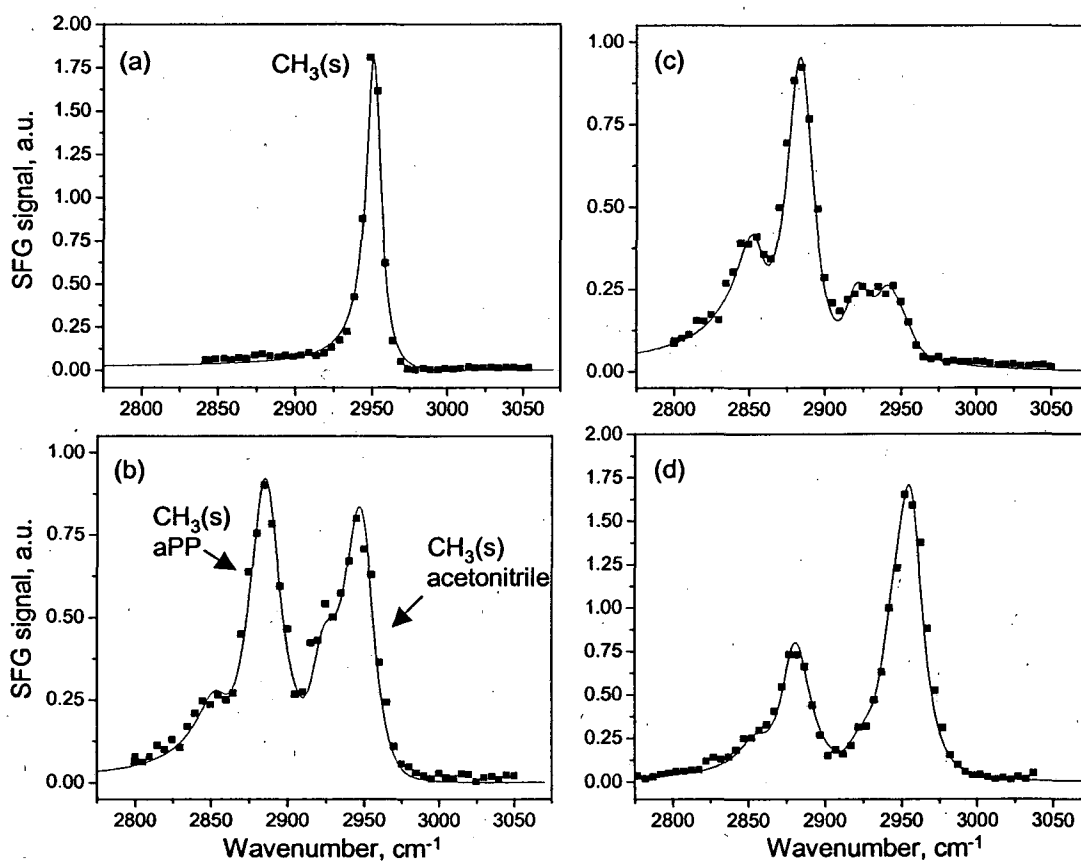
Figure 4-3: SFG spectra of (a) acetonitrile liquid/vapor interface (b) aPP/acetonitrile vapor interface (c) aPP/deuterated acetonitrile vapor interface and (d) aPP/acetonitrile liquid interface.

Polypropylene/water interface Water is also a poor solvent for polypropylene. An obvious difference between water and the other two liquids is that water has no large nonpolar groups to interact with the aPP. When aPP is exposed to water vapor (17.5 torr at 20 C) there is no measurable change in the SFG spectra. An SFG spectrum collected from an aPP in direct contact with water is shown in Figures 4-4. The overall intensity of the $CH_3(s)$ vibration is significantly lower than it is in the spectrum collected from the aPP/air interface. Additionally, the amplitude of the $CH_3(s)$ stretch relative to the $CH_3(a)$ stretch decreases in magnitude. Part of the decrease in spectral intensity at the liquid interface can again be attributed to Fresnel factors.
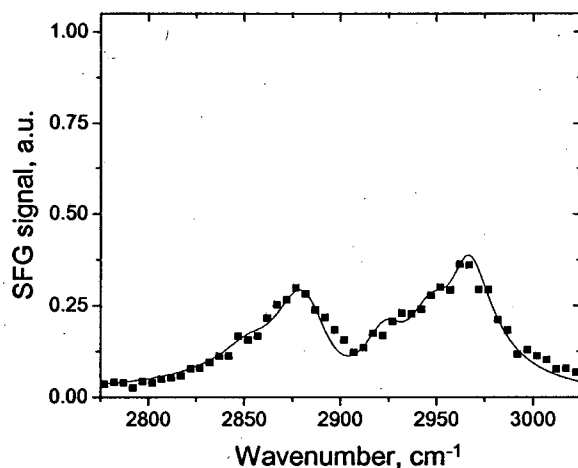
Figure 4-4: SFG spectrum of the aPP/water interface. The lower ratio of the $CH_3(s)/CH_3(a)$ vibrational stretches suggests that the methyl side branches restructure and are not upright oriented at the interface.

Qualitatively, a decrease in the $CH_3(s)/CH_3(a)$ peak ratio indicates that the aPP methyl branches are not well-oriented towards the liquid phase, as compared to the aPP/methanol and aPP/acetonitrile interfaces. The methyl groups at the interface are either more randomly distributed or are tilted away from the liquid phase. The orientation

and distribution of the methyl groups at the aPP/water interface can be quantitatively obtained using methods outlined in Chapter 1, however, the uncertainty in the orientation estimate increases dramatically as the overall intensity of the SFG signal decreases and as the ratio of the $CH_3(s)/CH_3(a)$ peaks decreases. All of the spectral changes we have observed are reversible, and when the aPP is removed from the methanol, acetonitrile, or water environments, SFG spectra consistent with the aPP/air interface are recovered.

4.4 Discussion

The results of these experiments show that ordered interfaces can form between immiscible polymer and liquid pairs, and contrast the results obtained from polymer surfaces exposed to solvent molecules. For example, when aPP was exposed to n-hexane vapor, we measured no SFG signal from the aPP/vapor interface, indicating that the interface became solvated and disordered - similar to the data reported in the previous chapter showing a disordering effect at the polystyrene/toluene interface.

It is interesting to note that the configuration of aPP methyl side branches is measurably the same at the aPP/air, aPP/methanol, and aPP/acetonitrile interfaces. Air is generally considered hydrophobic. Since the methanol and acetonitrile molecules align with their methyl groups oriented towards the interfaces, suggests that these are also 'hydrophobic' interfaces. Recent studies of polystyrene/solid interfaces (hydrophobic and hydrophilic) indicate that the configuration of the polystyrene phenyl side branches is similar at air interfaces and at solid hydrophobic interfaces.[14] At hydrophilic substrates, the phenyl branches were shown to adapt a different orientation. From those results, it was suggested that polystyrene side branches adapt a general 'hydrophobic' and 'hydrophilic' configuration. Our results support the notion that hydrophobicity of the

interface plays a key role in influencing the configuration of polymer side branches at an interface.

Our observations for the aPP interface structure can be compared to SFG results obtained from self-assembled monolayer/liquid interfaces, which have been more extensively studied. At one extreme, solvent-induced disordering has been observed by Zolk et al. for a hydrophilic-capped, alkane self-assembled monolayer placed in contact with water and with carbon tetrachloride.[20] In that example, the authors observe that water solvates the hydrophilic end group, while carbon tetrachloride penetrates into the hydrophobic backbone and disrupts the ordering of the entire chain.

Ward et al. studied the structure of ODT/liquid interfaces.[21,22] ODT forms a tightly packed monolayer on gold substrates where the terminal methyl group is oriented away from the substrate. Spectra obtained from the ODT/water and ODT/surfactant interfaces indicated that the ODT interface structure was qualitatively insensitive to environment. The ODT oriented its terminal methyl group oriented away from the gold in water. Amphiphilic surfactants were shown to orient with their hydrophobic ends oriented towards the monolayer. Miranda et al. studied a less tightly packed DOAC self assembled monolayer.[23,24] In contrast to the results obtained from the ODT layers, it was observed that the conformation of the DOAC monolayer is more sensitive to environment. In water, the DOAC interface disordered and was explained by the higher mobility of the loosely packed monolayer chain.

Returning to polymers, the aPP surface is nonpolar, uncharged, and is not expected to hydrogen bond with the polar molecules in the liquid or vapor phase. To an extent, the aPP surface behaves like the tightly packed ODT self assembled monolayer at

69

the polymer/air and at the polymer/amphiphile interface. At the aPP/methanol liquid interface, orienting the methyl end of methanol towards the aPP surface allows the –OH group to hydrogen bond with the bulk methanol, similar to the SFG results obtained by Ward et al. on the configuration of the ODT/dodecanol interface.

The aPP methyl side branches restructure when the polymer is exposed to water. The side branches tilt/disorder, but do not completely disorder. This result is intermediate to the qualitative results reported for the tightly packed ODT self assembled monolayers (no change) and the total disordering reported for the DOAC monolayer. Presumably, the restructuring minimizes interactions with the water molecules. The restructuring is feasible considering the aPP is rubbery at room temperature and capable of at least local reconstruction. The result obtained from the aPP/water interface can be placed in the context of recent results published by Wang et al. on the poly(butyl)methacrylate (PBMA) surface in contact with water, which showed that the orientation of the ester side branch changes when the PBMA is placed in water. An important distinction between PBMA and aPP is that the ester side branch of PBMA is capable of hydrogen bonding with the water. Thus the PBMA side branches may restructure due to favorable interactions at the polymer/water interface.

4.5 Conclusion

Well-defined and ordered interfaces are formed between immiscible polymer-liquid(vapor) pairs, and both the polymer and the liquid/vapor components can exhibit ordering. In the cases of polypropylene in contact with either methanol or acetonitrile, the methyl side branch of polypropylene and the methyl group of the liquid/vapor orient towards each other, forming an ordered interface. However, when polypropylene is

placed into contact with water, interactions between polypropylene and water cause polypropylene side branches to be less oriented towards the liquid phase.

With respect to contact angle hysteresis, our results show that rubbery aPP, containing only nonpolar components, can restructure in response to its environment, even if there is limited penetration by the liquid phase. Thus it is reasonable to believe that a portion of the contact angle hysteresis measured for homopolymers is due to local restructuring of molecular groups. In addition to changing the chemical environment at the interface, restructuring may also lead to a change in texture at the molecular level. Molecular level texture has been shown to influence the contact angle of self assembled monolayers. Ongoing experiments involve studying restructuring of polymer surfaces upon adsorption of surfactant polymers from aqueous solution.

References

[1] Israelachvili, J. *Intermolecular and Surface Forces, 2nd Edition*, Academic Press Inc., **1992**.

[2] Fadeev, A.Y.; McCarthy, T.J. *Langmuir*, **1999**, *15*, 3759.

[3] Lam, C.N.C.; Wu, R.; Li, D.; Hair, M.L.; Neumann, A.W. *Adv. Coll. & Int. Sci.*, **2002**, *96*, 169.

[4] Chen, Z.; Shen, Y.R.; Somorjai, G.A. *Ann. Rev. of Phys. Chem.*, **2002**, *53*, 437.

[5] Opdahl, A.; Phillips, R.A.; Somorjai, G.A. *J. Phys. Chem B*, **2002**, *106*, 5212.

[6] Wang, J.; Chen, C.; Buck, S.M.; Chen, Z. *J. Phys. Chem. B*, **2001**, *105*, 12118.

[7] Zhang, D.; Dougal, S.M.; Yeganeh, M.S. *Langmuir*, **2000**, *16*, 4528.

[8] Gautam, K.S.; Schwab, A.D.; Dhinojwala, A.; Zhang, D.; Dougal, S.M.; Yeganeh, M.S. *Phys. Rev. Lett.*, **2000**, *85*, 3854.

[9] Briggman, K.A.; Stephenson, J.C.; Wallace, W.E.; Richter, L.J. *J. Phys.Chem. B*, **2001**, *105*, 2785.

[10] Oh-e, M.; Hong, S.C.; Shen, Y.R. *Appl. Phys. Lett.*, **2002**, *80*, 784.

[11] Mansfield, K.F.; Theodorou, D.N. *Macromolecules*, **1991**, *24*, 6283.

[12] Clancy, T.C.; Hwan Jang, J.; Dhinojwala, A.; Mattice, W.L. *J. Phys. Chem. B*, **2001**, *105*, 11493.

[13] Harp, G.P.; Gautam, K.S.; Dhinojwala, A. *J. Amer. Chem. Soc.*, **2002**, *124*, 7908.

[14] Wilson, P.T.; Richter, L.J.; Wallace, W.E.; Briggman, K.A.; Stephenson, J.C. *Chem. Phys. Lett.*, **2002**, *363*, 161.

[15] Wang, J.; Woodcock, S.E.; Buck, S.M.; Chen, C.; Chen, Z. *J. Amer. Chem. Soc.*, **2001**, *123*, 9470.

[16] Chen, J.X.; Zhuang, H.Z.; Zhao, J.; Gardella, J.A. *Surf. and Int. Anal.*, **2001**, *31*, 713.

[17] Opdahl, A.; Somorjai, G.A. *Langmuir*, **2002**, *18*, 9409.

[18] Superfine, R.; Huang, J.Y.; Shen, Y.R. *Phys. Rev. Lett.*, **1991**, *66*, 1066.

[19] Kim, J.; Chou, K.C.; Somorjai, G.A. *J. Phys. Chem. B*, **2003**, *107*, 1592.

[20] Zolk, M.; Eisert, F.; Pipper, J.; Herrwerth, S.; Eck, W.; Buck, M.; Grunze, M. *Langmuir*, **2000**, *16*, 5849.

[21] Ward, R.N.; Duffy, D.C.; Bain, C.D. *J. Phys. Chem.*, **1993**, *97*, 7141.

[22] Ward, R.N.; Duffy, D.C.; Davies, P.B.; Bain, C.D. *J. Phys. Chem.*, **1994**, *98*, 8536.

[23] Miranda, P.; Pflumio, V.; Saijo, H.; Shen, Y.R. *J. Am. Chem. Soc.*, **1998**, *120*, 12092.

[24] Miranda, P.; Shen, Y.R. *J. Phys. Chem. B.*, **1999**, *103*, 3292.

Chapter 5

Polyolefin blend surfaces: Effect of bulk miscibility on the surface composition of *a*PP/*a*EPR blends

5.1 Introduction

The surface and bulk phase behavior of polyolefin copolymers and blends has received considerable attention in recent years in large part because of their continued commercial importance. Polyolefin synthesis also enables the careful control of architectural variables, such as short-chain branching and tacticity, with similar hydrophobic units. This control has lead to the use of polyolefins as model systems for studying the underlying molecular phenomena governing the fundamental properties of polymers including surface segregation and bulk phase behavior.

Many experimental[1,2,3] and theoretical[4,5,6,7] studies have been made in an attempt to better understand surface segregation in polyolefin blends. Side branches have been found to be a key variable in determining the surface activity of polyolefins. Depth

profiling measurements have shown that for blends of polyolefin copolymers with different number densities of ethyl side branches, the more branched copolymer has a tendency to segregate to the air/polymer interface.[1,2] For ethyl branched polyolefin blends and polystyrene blends,[2,8,9,10] the theory developed by Schmidt and Binder, incorporating the Flory-Huggins interaction parameter, χ_{ab}, and the difference in surface chemical potentials of the blend components has been applied to describe the shape of experimentally measured depth profiles.[4]

For miscible and partially miscible blends, it is generally accepted that the enthalpic cohesive energy of the individual components plays a large role in determining the surface composition at the air-polymer interface, with the component having the lowest cohesive energy, or surface tension, being favored at that interface. The extent that entropy controls the surface conformation is less understood.[3,5] Theoretical results suggest that conformational entropy, related to the size of the random coil, and packing entropy related to the configuration of the polymer at the interface play competing roles in mixtures of branched polyolefins at the air interface.

The results presented in Chapters 1 and 2 showed that, at the molecular level, many polyolefins assume specific conformations at the air interface.[11,12,13] In particular, the aspecific poly(ethylene-co-propylene) copolymers (aEPR) were shown to configure in a way that preferentially orients methyl side branches upright at the air/polymer interface.[13] These specific types of molecular interactions at the air/polymer interface may also affect the surface segregation properties for blends of aEPR copolymers.

The segregation thermodynamics for bulk immiscible polymers are not as well understood as the miscible case. At the surface, a wetting transition from complete to

partial wetting has been predicted for the immiscible case, and is predicted to be dependent on the degree of immiscibility as well as the difference in surface activities of the blend components.[14]   This transition to partial wetting is expected to occur by lowering the temperature of the blend far below the critical temperature, increasing the molecular weight of the blend components, or by decreasing the relative surface affinities of the blend components.

In this chapter, SFG, XPS, and differential scanning calorimetry (DSC) have been used to examine the surface molecular structure, the chemical morphology of the surface region, and the bulk phase behavior of miscible and immiscible blends of atactic polypropylene (aPP) with aspecific poly(ethylene-co-propylene) rubber (aEPR). Each of the blend components has the basic structure given in Figure 5-1 and is comprised of similar CH_2 and CH_3 units. Blend miscibility is controlled by varying the molecular weight of the aPP component.
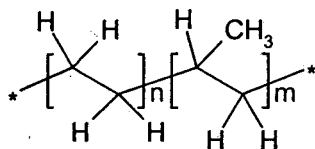
Figure 5-1: Structure of aspecific poly(ethylene-co-propylene) rubber (aEPR). The distribution of block lengths (n,m) is very nearly random and methyl group placement in the propylene units lack stereospecificity

These model blends mimic the important commercial blend of isotactic PP/EPR, without complications due to crystallinity, through the use of an aspecific polymerization catalyst. SFG and XPS are both surface sensitive techniques and can distinguish between the CH_3 unit in propylene and the CH_2 unit, which is present in both the ethylene and propylene repeat units.[13,15] Additionally, SFG and XPS, applied to aPP/aEPR blends, do

not require isotopic labeling, and because SFG is a photon based technique and XPS is an electron based technique, each technique is sensitive to a different depth of the surface and gives a different type of chemical information.

SFG is specifically sensitive to the molecular composition and orientation of the surface monolayer. The surface sensitivity of XPS is limited by the mean-free-path of photoelectrons generated in the polymer, typically a few nanometers, and can be controlled to some extent by varying the detection angle with respect to the surface plane. Thus, SFG can be used to determine the composition of the surface monolayer, and XPS can be used to integrate the chemical composition of the top few nanometers of the surface. SFG spectra of *a*PP/*a*EPR blends show that *a*PP, the component with the lower surface tension, preferentially segregates to the air/polymer interface for both the bulk miscible and bulk immiscible blends. The thickness of the *a*PP enrichment layer is detected by XPS and is shown to increase for the bulk immiscible blend.

5.2 Experimental procedures

Polymers

Table 5-1 summarizes the polymers used in this study. Further description of the synthesis of the *a*PP and *a*EPR polymers is described in Chapter 2. The *a*PP homopolymers, *a*PP1 and *a*PP2, differ only in their molecular weight. Solutions containing 5% wt. polymer were prepared in n-hexane and allowed to equilibrate for at least 2 days. The primary blend systems were blends of *a*PP1 and *a*EPR7 and blends of *a*PP2 and *a*EPR7. Blends were prepared by mixing appropriate amounts of each solution and were allowed to equilibrate for an additional 2 days. Films for SFG and XPS analysis were prepared by spin casting solutions onto IR grade fused silica substrates. After

casting, the films were annealed at 70°C for 12 hours. Films were measured by atomic

force microscopy to have thickness between 200 and 300nm. Both SFG and XPS

measurements were made at room temperature, above the glass transition temperature of

each of the blend components. Samples (15mg) for DSC analysis were prepared by

solvent evaporation.

Table 5-1 Structural characteristics of the aEPR copolymers.

Sample	M_w	M_w/M_n	wt. % ethylene	Mole % ethylene	$[CH_2]/[CH_3]_{bulk}$	Sequence parameter[b]
aPP1[a]	54,000	2.0	0	0	1	-
aPP2[a]	210,000	2.0	0	0	1	-
aEPR2	48,000	2.0	4.7	6.9	1.15	1.0
aEPR3	54,000	2.0	7.1	10.3	1.23	1.0
aEPR4	54,000	2.0	13.5	19.0	1.47	1.1
aEPR5	48,000	2.1	20.3	27.7	1.76	1.3
aEPR6	54,000	2.0	25.9	34.4	2.05	1.3
aEPR7	54,000	1.9	32.3	41.7	2.43	1.4

[a]16% iso triads, 49%hetero triads, 35%syndio triads
[b]The sequence parameter, determined by NMR, is a measure of the randomness of the copolymer. It is 1 for a completely *random* distribution of comonomers, 2 for complete *alternation* of comonomers, and 0 for complete *block*-like sequencing.

Differential Scanning Calorimetry (DSC)

Baseline subtracted DSC scans were performed from -110°C to 120°C at

20°C/min in a Perkin-Elmer DSC-7 calorimeter with liquid nitrogen cooling and helium

purge using 15mg samples taken from the as-cast films. Additional experiments applied

a melt cycle by heating (20°C/min) the as-cast films to 200 °C for 2min, quenching

(320°C/min) to -110°C for 10min, and reheating (20°C/min). The as-cast films were also

annealed at various temperatures by sealing the samples in DSC pans and placing the

pans in sealed vials and annealing in a thermostatted oil bath for 16 hours at temperatures

ranging from 50-150°C. The annealed samples were characterized by DSC in an identical manner as the as-cast films.

Sum Frequency Generation Vibrational Spectroscopy (SFG)

Surface vibrational spectra were obtained by sum frequency generation (SFG) vibrational spectroscopy using the experimental setup described in Chapter 1. Additional details regarding SFG are available in references 16 and 17. Experimental data has been fit to Eq. 5-1 in order to extract $\tilde{A}_q$ for each vibrational mode. Spectra were collected using the $s_{sum}s_{vis}p_{ir}$ polarization combination.

$$I(\omega_{sum}) \propto |\chi^{(2)}|^2 = \left| \tilde{\chi}_{NR} + \sum_q \frac{\tilde{A}_q}{\omega_{IR} - \omega_q + i\Gamma_q} \right|^2 \qquad (5\text{-}1)$$

X-Ray Photoelectron Spectroscopy (XPS)

XPS experiments were performed on a Perkin-Elmer PHI 5300 XPS spectrometer with a position sensitive detector and a hemispherical electron energy analyzer. The Mg Kα x-ray emission (1253.6eV) was used as the probe and was generated with 400W (15 kV acceleration voltage) at the Mg cathode. A pass energy of 178eV was used for survey spectra with a 45 degree takeoff angle and a pass energy of 35eV was used for spectra of the valence band region at a 45 degree takeoff angle. The sampling depth of the XPS experiments is based on an attenuation length of 2.9±0.4nm measured by Roberts et al. for photoelectrons ejected from PMMA having a kinetic energy of 1200eV.[18] Using this value as an approximation for the attenuation length of valence band photoelectrons generated by the Kα x-ray source (kinetic energy of photoelectrons ~1240eV) leads to a 95% sampling depth of 6.1±0.8nm.[19]

5.3 Bulk phase behavior of aPP/aEPR blend (DSC)

Figure 5-2a shows DSC scans of films of low molecular weight polypropylene (aPP1), the ethylene/propylene copolymer with the highest ethylene content (aEPR7), and a 50:50 weight percent aPP1/aEPR7 blend of the two components cast from heptane. Figure 5-2a shows that the 50:50 blend has a single glass transition temperature (T_g) at $-30°C$, intermediate between the aPP1 (T_g 0°C) and aEPR7 (T_g $-46°C$) components. The breadth of the transition region is greater in the blend than the individual components. This behavior is typical of a miscible blend and indicates that blends of low molecular weight aPP1 and aEPR7 solution cast from heptane (or solvents with increased volatility) are in a single miscible phase as measured by glass transition measurements. The aPP1 and aEPR7 components will be in a single phase at room temperature for all blend compositions, since the 50:50 weight percent blends are very near the critical composition, which will have the strongest tendency for phase separation.

In contrast to Figure 5-2a, Figure 5-2b shows DSC scans of as-cast films (from hexane) of high molecular weight polypropylene (aPP2), the ethylene/propylene copolymer with the highest ethylene content (aEPR7), and a 50:50 weight percent aPP2/aEPR7 blend of the two components. The aPP2 sample has the same tacticity microstructure as aPP1 but with higher molecular weight (Table 5-1). Two T_g's are visible on the DSC trace of the blend, showing clear phase separation of the aEPR7 and aPP2 components. Although not shown, phase separation is stable to a melt cycle (see Experimental), where the individual T_g's in the blend become sharper. This observation is consistent with an immiscible melt in the 50:50 weight percent aPP2/aEPR7 blend.

The blend T_g's are shifted somewhat relative to the parent polymers, most prominently for the aPP2-rich phase.
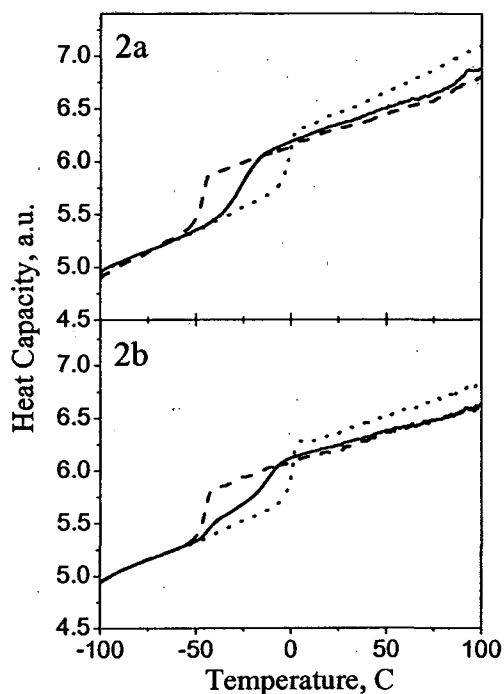
Figure 5-2: DSC scans (20°C/min) of individual components and blends: (a) aPP1 (dotted); aEPR7 (dashed); and 50:50 wt. percent aPP1/aEPR7 blend (solid). (b) aPP2 (dotted); aEPR7 (dashed); and 50:50 wt. percent aPP2/aEPR7 blend (solid).

5.4 Surface monolayer composition of aPP/aEPR blends

SFG spectra of poly(ethylene-co-propylene) rubber series

Surface monolayer compositions and configurations were characterized by SFG. The aEPR copolymers presented in Chpater 2 used as a calibration series for estimating the surface composition of the blends. SFG spectra collected using the ssp polarization combination of aPP1, aEPR4, and aEPR7 are shown in Figure 5-3. As described in Chapter 5, the features at 2883cm^{-1} and the weak shoulder at 2965cm^{-1} are assigned as the

CH$_3$ symmetric and antisymmetric stretches, respectively. The features at 2850cm^{-1} and 2920cm^{-1} are assigned as the CH$_2$ symmetric and antisymmetric stretches, respectively, from the CH$_2$ backbone.
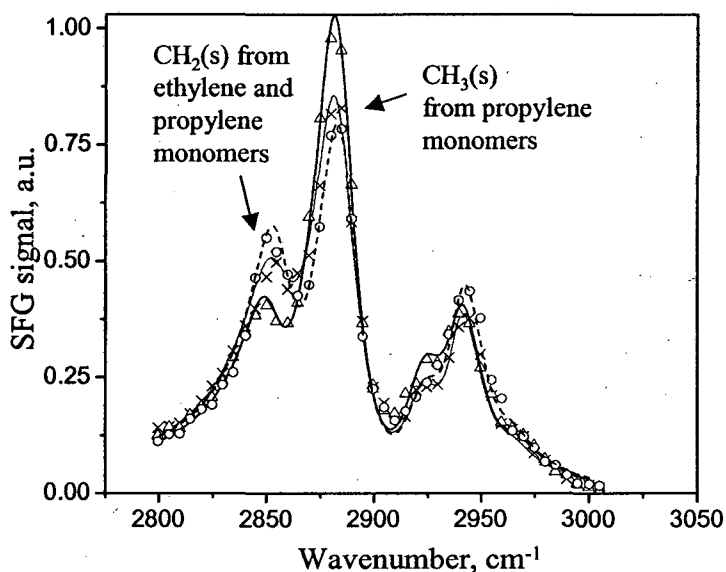
Figure 5-3: SFG spectra of *a*PP1(triangle); *a*EPR5(*x*); and *a*EPR7(circle) - *ssp* polarization combination. Solid lines represent the best fit to Equation 5-1.

Each spectrum has been fit to Equation 5-1 using five peaks. The ratio of the fitted mode strengths, A_q, of the methylene CH$_2$(s) stretch (2855cm^{-1}) to the methyl CH$_3$(s) stretch (2883cm^{-1}) as a function of bulk composition for the *a*EPR series was presented in Chapter 2. The dependence is roughly linear over the concentration range we have investigated, qualitatively consistent with the changes in bulk composition. However, because the SFG mode strengths represent a convolution of concentration and orientation, the trend in the mode strength ratio reflects changes in the total configuration of each of the polymers at the interface.

Analysis of the SFG spectra, presented in Chapter 2, suggested that the different $CH_2(s):CH_3(s)$ mode strength ratios measured for aPP and aEPR is related to significant differences in orientation of the polymer backbone between the two polymers. Both aPP1 and the aEPR7 copolymer tend to preferentially order methyl groups upright at the air/polymer interface. Qualitatively, this is evident by the large $CH_3(s)$ peak for both the aPP and the aEPR7 spectra shown in Figure 5-3. The tendency to extend bulky hydrophobic side branches into the air or vacuum is an effect that has been observed both experimentally[20,21,22] and theoretically[23,24] for several different polymers. Quantitatively, aEPR7 orients fewer methyl groups per unit surface area compared to aPP1, however, after taking into account differences in the bulk concentrations of methyl branches aEPR7 orients a large surface excess of methyl side branches relative to aPP1.

Although the ratio of the $CH_2(s)$ to $CH_3(s)$ mode strengths reflects differences in chain configuration, the ratio of the $CH_2(s)$ to $CH_3(s)$ mode strengths is used in this analysis as an indicator of the surface composition. Under the assumption that in a blend of aPP and aEPR7, the surface configurations of the individual components do not change significantly, a high value of the $CH_2(s)/CH_3(s)$ mode strength ratio denotes an aEPR7-rich surface whereas a low value denotes an aPP-rich surface.

SFG spectra of blend systems

Figure 5-4 compares an SFG spectrum taken from a 50:50 weight percent bulk miscible aPP1/aEPR7 blend film immediately after spin casting from n-hexane to a spectrum obtained from an identical film after it was annealed for 15 hours at 50°C. The $CH_2(s)$ and $CH_3(s)$ features present in the spectrum of the as-cast film are intermediate to the $CH_2(s)$ and $CH_3(s)$ features of aPP1 and aEPR7 presented in Figure 5-3, indicating

that immediately after casting the blend film, both components are present at the surface, and that segregation due to effects of the solvent evaporation are not a major concern.

After annealing, the $CH_2(s)$ peak decreases and the $CH_3(s)$ peak increases in magnitude showing that the blend surface was not in its equilibrium state after it was spin-cast. SFG spectra collected after an additional 15 hour 50°C annealing period and a third set collected three weeks later after a final 15 hour annealing period at 50°C yielded indistinguishable results indicating that after the initial 15 hour anneal, an equilibrium surface coverage had been reached.
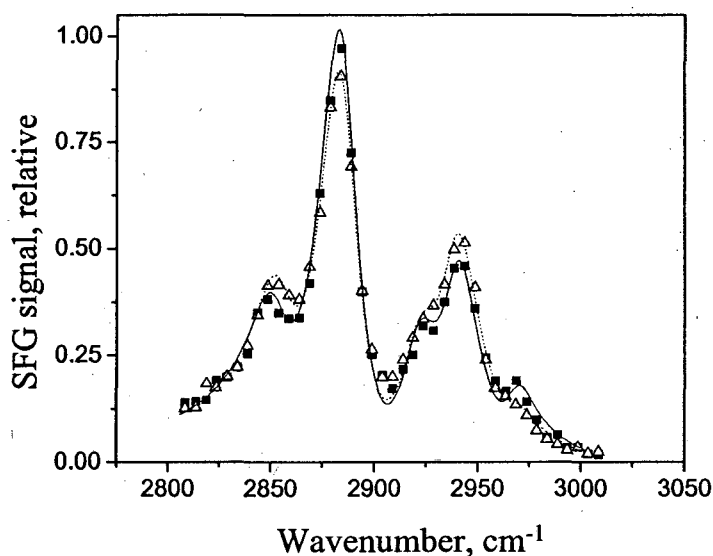
Figure 5-4: SFG spectra of an "as-cast" 50:50 weight percent aPP1/aEPR7 blend (triangle) and 50:50 weight percent aPP2/aEPR7 blend annealed for 15 hours at 50°C (square). - *ssp* polarization combination. Solid lines represent the best fit to Eq. 5-1.

The $CH_2(s)$ and $CH_3(s)$ features of the annealed film are much more "aPP1-like" than the as-cast blend, showing that there is a preference for aPP1 to segregate to the

surface. SFG spectra of low molecular weight aPP1, aEPR7, and a 50:50 weight percent aPP1/aEPR7 blend sample annealed at 50°C for 15 hours are shown in Figure 5-5. Qualitatively, the spectrum of the 50:50 aPP1/aEPR7 blend is nearly identical to the aPP1 spectra – indicating preferential segregation of aPP1 to the surface. The ratio of the CH_2(s) mode strength to the CH_3(s) mode strength for the annealed 50:50 weight percent blend and other blend compositions, an aPP1-rich 85:15 weight percent and an aEPR7-rich 85:15 weight percent blend, are plotted in Figure 5-6 along with the ratios for the aEPR calibration series. For the 50:50 blend and for the 85:15 aPP1 rich compositional blend, the ratio of the CH_2(s) mode strength to CH_3(s) mode strength is, within our experimental uncertainty, identical to the ratio for aPP ($[CH_2]/[CH_3]=1$), indicating a large surface excess of aPP. For the aEPR7-rich 15:85 blend, the mode strength ratio is slightly higher than the ratio of pure aPP indicating that, for this composition, the surface may contain both components, with the majority component being aPP.

SFG spectra of high molecular weight aPP2, aEPR7, and a 50:50 weight percent aPP2/aEPR7 blend are shown in Figure 5-5b. The spectrum of the blend is also nearly identical to the spectra of aPP2, indicating preferential segregation of polypropylene at the monolayer level. The SFG CH_2:CH_3 mode strength ratio for aPP2 and for the 50:50 weight percent aPP2/aEPR7 blend is plotted in Figure 5-6. The mode strength ratio for the blend strongly favors aPP2, suggesting that aPP2 covers the surface and that partial wetting of aPP is not an issue for the 50:50 weight percent blend under the experimental conditions.
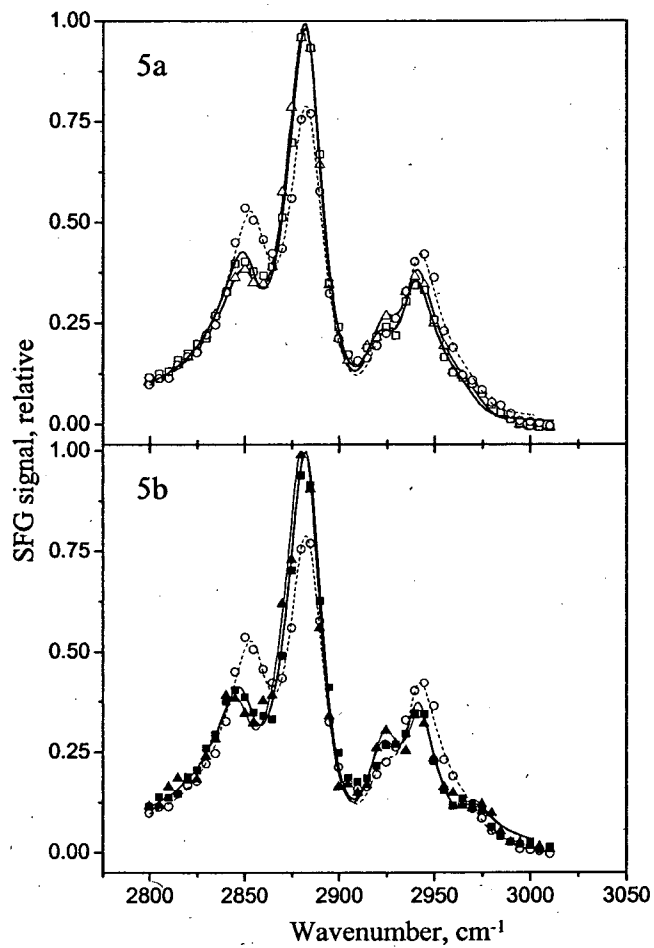
Figure 5-5: (a) SFG spectra of *a*PP1(r); *a*EPR7( ); and 50:50 weight percent *a*PP1/*a*EPR7 blend(£): (b) SFG spectra of *a*PP2(p); *a*EPR7( ); and 50:50 weight percent *a*PP2/*a*EPR7 blend(¢) - *ssp* polarization combination. Solid lines represent the best fit to Eq. 5-1.
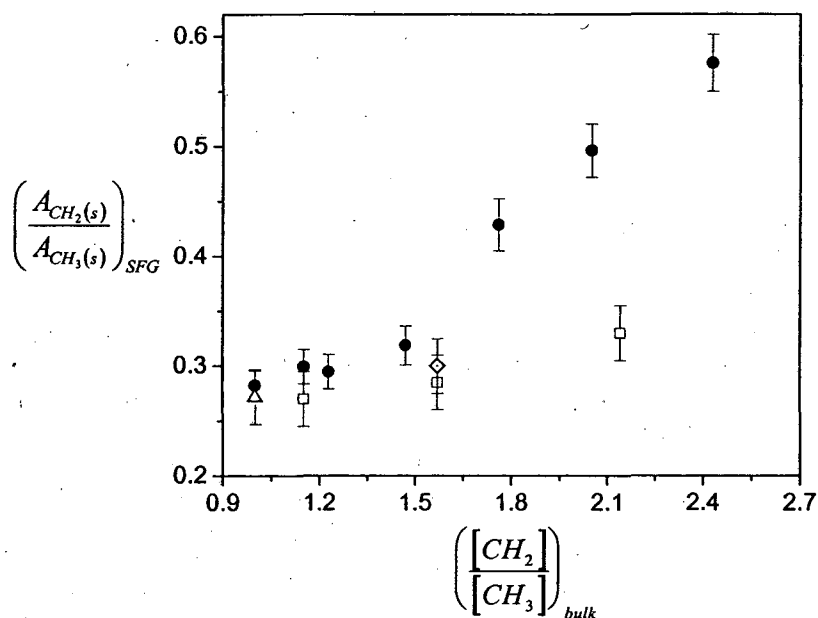
Figure 5-6: $CH_2(s)/CH_3(s)$ SFG vibrational mode strength ratio (Aq) vs. bulk $[CH_2]/[CH_3]$ composition for aPP1 and the aEPR copolymer series ($\bullet$); aPP1/aEPR7 blends ($\square$); aPP2 ($\triangle$); and aPP2/aEPR7 blends ($\diamond$).

5.5 Surface composition of the top 6-8 nm of aPP/aEPR blends

XPS spectra of poly(ethylene-co-propylene) rubber series

XPS has been used to integrate the composition of the top 6.1 ± 0.8nm of the films. The aEPR series is used again as a calibration set. XPS spectra of the carbon 1s core peak at 285eV for aPP and aEPR are virtually identical. The valence band spectra, shown in Figure 5-7, however, show significant differences. Both polymers have peaks at 15eV and at 21eV that are assigned to the 2s bonding and antibonding orbitals from the $-CH_2-$ backbone units of the polymers.[15] Both polymers have an additional feature at 18eV that

is 2 overlapping peaks, assigned to the 2s bonding and antibonding orbitals of the pendant CH_3 group. The broad feature at 9eV arises from the carbon 2p band.
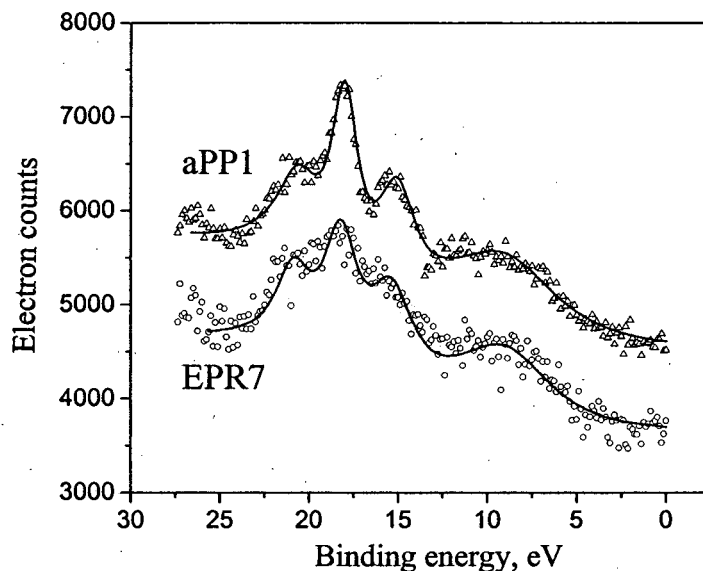
Figure 5-7: Valence XPS spectra of aPP1 and aEPR7. Spectra are vertically offset for clarity of presentation. Solid lines represent the best-fit results. The ratio of the CH_2 peaks at 15eV and 21eV to the CH_3 peak at 18eV increases as the ethylene content of the copolymer increases.

The valence band XPS spectra of aEPR7, which contains both ethylene and propylene monomers, has smaller CH_3 features relative to the CH_2 features compared to similar ratios in the valence band spectra of aPP. To quantify this result, after background subtraction, each aEPR valence band spectra has been fit to four peaks. The fitted spectra for aPP and aEPR7 are represented by the solid lines in Figure 5-7. A plot of the ratio of the CH_2 fitted peak areas to the CH_3 fitted peak area as a function of the bulk

[CH$_2$]/[CH$_3$] ratio for the aEPR series (Figure 5-8) yields a linear relationship –
consistent with the random nature of the aEPR copolymers. As the technique is sensitive
to a much greater depth than SFG, it is insensitive to the orientation effects seen in the
SFG data. The ratio of fitted peak areas is used here to characterize the relative methyl
group concentration of the top few nanometers of the blend films.

XPS of blend systems

The CH$_2$/CH$_3$ XPS peak area ratios vs. the bulk [CH$_2$]/[CH$_3$] ratios for aEPR7
blends with low molecular weight aPP1 are shown in Figure 5-8 along with the ratios for
the aEPR calibration series. The CH$_2$/CH$_3$ peak area ratio for each low molecular weight
blend sample (33:67, 50:50, and 67:33 weight percent aPP1/aEPR7) fits nearly
identically to the peak area ratios for the copolymer series. This indicates that the aPP1
enrichment that is observable by SFG for this sample is not detectable at the level of
resolution of XPS. Since the depth that the XPS is integrating over is estimated at
6.1±0.8nm, this indicates that the aPP1 enrichment layer is very thin – the top 5-7nm
contains significant quantities of each of the two components. Considering the sampling
depth and the signal to noise of the measurement, it is likely that the highest levels of aPP
in the surface enrichment layer are restricted to the top 2-3nm of the film. The aEPR7
blend system with high molecular weight aPP2 behaves quite differently. The CH$_2$/CH$_3$
peak area ratio for the 50:50 weight percent blend is also shown in Figure 5-8. For this
blend composition, the spectra shows a significant depletion of the CH$_2$/CH$_3$ ratio relative
to the bulk [CH$_2$]/[CH$_3$] ratio. This indicates that the top 6.1±0.8nm of the high molecular
weight blend is strongly enriched in aPP2.
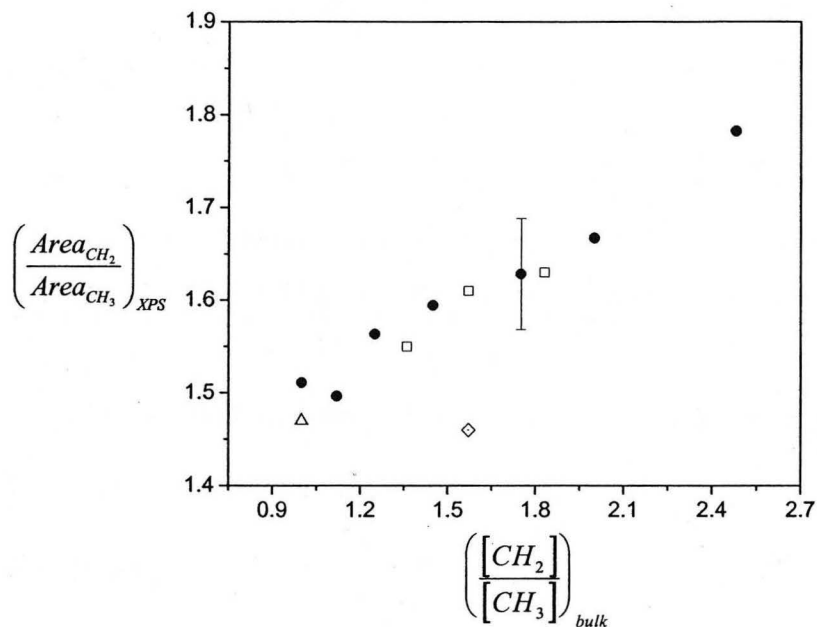
Figure 5-8: Valence XPS CH_2/CH_3 peak area ratio, , vs. bulk $[CH_2]/[CH_3]$ composition for aPP1 and the aEPR copolymers (●); aPP1/aEPR7 blends (□); aPP2 (△); and aPP2/aEPR7 blends (◇).

5.6 Discussion

The bulk phase behaviors observed by DSC and the corresponding surface compositions observed by SFG and XPS for the two blend systems are summarized in Table 5-2. For both blend systems, aPP preferentially coats the surface at a monolayer level. The low molecular weight miscible blend (aPP1/aEPR7) has an enrichment layer less than ~3nm thick - beyond the resolution of our XPS experiment. The high molecular weight bulk immiscible system (aPP2/aEPR7) has a much thicker enrichment layer, which is detectable by XPS. The *minimum* thickness of this layer is ~6.1±0.8nm.

Table 5-2 Summary of bulk phase behavior measured by DSC and surface compositions measured by SFG and XPS for the 50:50 *a*PP1/*a*EPR7 system and the 50:50 *a*PP2/*a*EPR7 blend systems.

Bulk composition	DSC (bulk)	SFG (surface monolayer)	XPS (top 6.1±0.8nm)
*50:50 a*PP1/*a*EPR7	single phase	*a*PP1 enriched	mixed *a*PP1/*a*EPR7
*50:50 a*PP2/*a*EPR7	Phase separated	*a*PP2 enriched	*a*PP2 enriched

AFM has been used to monitor the *a*PP wetting process. Figure 5-9 shows a series of AFM topography and lateral force images obtained from the surface of a 50:50 weight percent *a*PP2:*a*EPR7 blend at various stages of the annealing process. Immediately after casting, the surface of the blend is rough. The lateral force image shows the presence of 'low friction' (dark) and 'high friction' (light) phases. Since the *a*EPR is much softer than the *a*PP component, it is reasonable to suggest that the 'high friction' regions are aEPR7-rich. As the blend is annealed, the surface becomes smoother and the 'high friction' *a*EPR regions cover less surface area. In contrast, AFM images obtained form low molecular weight *a*PP1:*a*EPR7 blends are homogeneous at all stages of annealing.

The results of these experiments are qualitatively similar to the studies on surface segregation of blends of polyolefin copolymers with ethyl side branches, and show another case where highly branched copolymers tend to segregate to the air/polymer surface.[1,2,3] The enrichment layer for the ethyl branched copolymers has been proposed to have its origins in the enthalpic cohesive energy. That is, polymer chains with higher branch ratios don't tend to pack as well as less branched chains and tend to have fewer interactions with other chains, leading to a low cohesive energy. By being at the surface, a highly branched chain loses fewer enthalpic interchain interactions than a less branched

chain. It has also been argued that conformational entropy is an important consideration, with the component having the lower value of β^2 ($\beta^2 = R_g^2/V$; R_g is radius of gyration and V is chain volume) favored at the surface.[5] For most polyolefins, this also happens to be the more branched component.
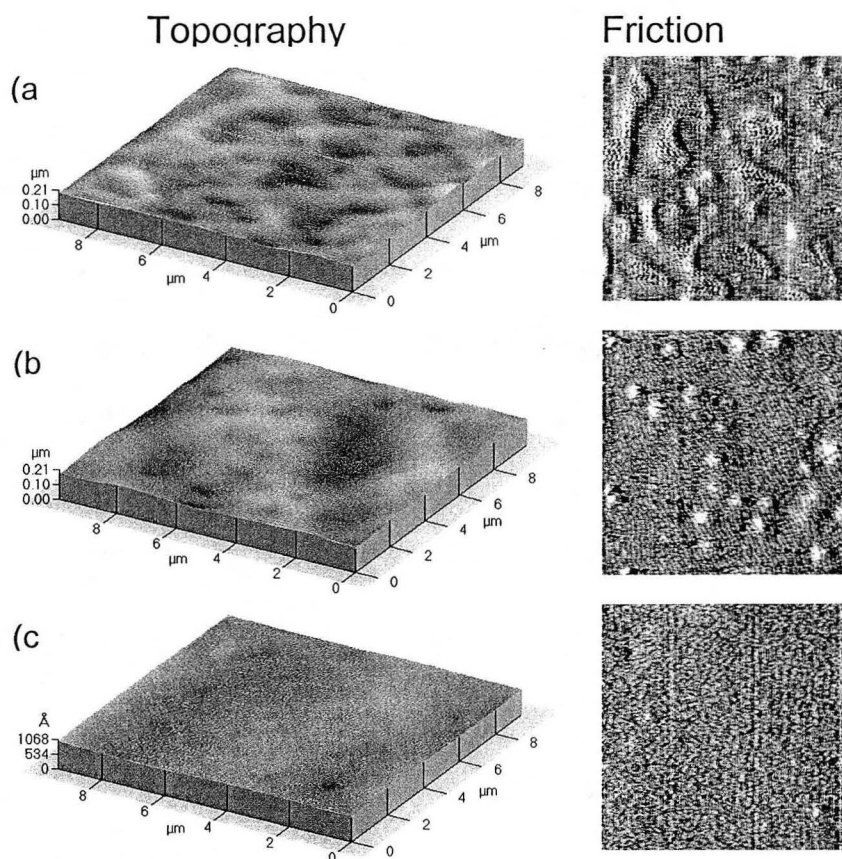
Figure 5-9: AFM topography and corresponding lateral force images obtained from an *a*PP2:*a*EPR7 blend film (a) immediately after casting from n-hexane (b) after annealing for 4 hours at 100C and (c) after annealing for 12 hours at 100C.

Our results support the previous experimental evidence that a high density of side branches leads to enhanced surface activity. Additionally, the *a*EPR copolymers have

91

been shown to preferentially orient methyl groups upright at the interface. This may mean that at least part of the surface segregation tendency of higher branched polymers may be due to specific interactions between the polymer and the low density air interface. Since aPP was shown to have a larger number density of methyl groups orienting away from the surface than aEPR,[13] aPP should be the more surface-active component on these grounds.

The SFG analysis presented in Chapter 2 also suggests that both aPP and aEPR7 polymer backbone segments at the interface are oriented parallel to the air interface, and that aEPR7 assumes has longer chain segments at the surface than aPP. This indicates that the ethylene rich aEPR7 copolymer backbone pack better at the interface than the aPP backbone. This experimental evidence along with the SFG results for the aPP/aEPR7 blend suggests that the packing entropy contributions based on the orientation of the chain backbone at the interface do not significantly affect the surface segregation properties at the air/polymer interface. The packing entropy may an important factor at a high density confined interface.

5.7 Comparison between measured and calculated aPP surface enrichment layer thickness

Models based on a Flory-Huggins energy of mixing, namely the Schmidt-Binder model and the exponential approximation to the Schmidt-Binder model, have recently been shown to give reliable results for modeling composition profiles of bulk miscible polymer blends with submicron thick surface enrichment layers.[2,4] Applying the exponential approximation model to the aPP1/aEPR7 system, it is assumed that the

surface concentration of aPP1 ($\phi_{aPP,0}$) decays to the bulk concentration of aPP1, $\phi_{aPP1,\infty}$, through the exponential shown in Equation 5-2 where z is the depth from the surface.

$$\phi_{aPP,z} = \phi_{aPP,\infty} + \left(\phi_{aPP,0} - \phi_{aPP,\infty}\right) \cdot e^{-\frac{z}{\varepsilon_b}} \tag{5-2}$$

The decay length of the aPP enrichment, ε_{aPP}, is given by Equation 3 and depends on the first two terms on the right hand side which contain combinatorial contributions and the third term which contains contributions from specific pair-wise interactions between aPP and aEPR7 characterized by the bulk interaction parameter, $\chi_{aPP/aEPR7}$, of the two components.

$$\varepsilon_{aPP} = \frac{a}{6} \cdot \left[\frac{\phi_{aPP}}{2 \cdot n_{aPP}} + \frac{\phi_{aEPR7}}{2 \cdot n_{aEPR7}} - \chi_{aPP/aEPR7} \cdot \phi_{aPP} \cdot \phi_{aEPR7} \right]^{-\frac{1}{2}} \tag{5-3}$$

In Equation 3, a is the weighted statistical segment length of aPP and aEPR7, n_{aPP} and n_{aEPR7} are the degrees of polymerization for aPP and aEPR, ϕ_{aPP} is the volume fraction of aPP in the blend, and ϕ_{aEPR7} is the volume fraction of aEPR7. The decay length, ε, and thus the thickness of the enrichment layer is greater for high molecular weight blends (large n) and for blends that have a large interaction parameter, χ_{ab}. As discussed earlier, the 50:50 weight percent aPP1/aEPR7 blend is miscible and should be amenable to treatment by Equation 5-2, provided $\chi_{aPP/aEPR7}$ is known. The procedure used to estimate $\chi_{aPP/aEPR7}$ is given in the appendix.

The compositional depth profile of the bulk miscible system estimated using Equations 2 and 3 with $\chi_{aPP/aEPR7}$ set to 0.00102 and a value of 0.55nm for a, the weighted segment length of aPP and aEPR7[25], is shown in Figure 10. Since the SFG data showed that aPP1 completely coated the surface, the monolayer aPP1 composition (ϕ_o)

was set at 1. The resulting curve in Figure 5-10 shows that the *a*PP1 enrichment at the uppermost monolayer (as measured by SFG) should decay to 90% of the bulk composition at a depth of 10nm. This estimate is reasonable in the context of the XPS experiment. The XPS measured composition is shown by the bracketed region. The shaded region represents the error in the XPS measurement. Since XPS integrates over ~6-8nm of the surface, the model predictions of a depletion of *a*EPR7 within the top 2-3nm is likely outside the resolution of the XPS experiment.
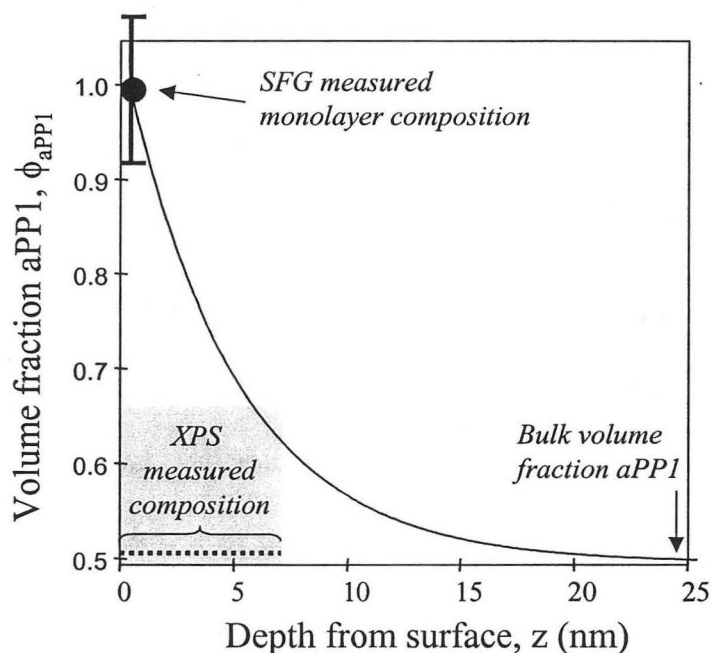
Figure 5-10: Comparison between calculated (solid curve) compositional profile and SFG and XPS determined composition profile for miscible *a*PP1/*a*EPR7 blend system.

The higher molecular weight *a*PP2/*a*EPR7 blend is bulk immiscible. For this case the *a*EPR7 depletion is observed by both SFG and XPS, indicating a much stronger enrichment of the *a*PP in the immiscible blend. This is consistent with literature thin film studies which show that equilibrium bilayers can develop in immiscible polymer blends with the surface active component (*a*PP) at the air-polymer interface.[2] This suggests the

94

possibility of much larger penetration depths of aPP2 and is consistent with the observed enrichment of aPP2 by both SFG and XPS. Interestingly, we still observe nearly pure aPP2 by SFG in the immiscible blend despite the fact that the DSC results indicates some mixing of aEPR7 in the bulk aPP-rich phase (see Appendix 1). This indicates preferential wetting of aPP2 at the surface monolayer within the aPP-rich surface region.

5.8 Conclusion

The surface monolayer composition of miscible and immiscible blends of atactic polypropylene (aPP) with aspecific poly(ethylene-co-propylene) rubber (aEPR) was characterized by SFG and XPS. SFG showed that polypropylene homopolymer segregated to the air/polymer interface for all blend compositions studied – consistent with the high surface activity of branched copolymers. X-ray photoelectron spectroscopy was used to estimate the thickness of the aPP enrichment layer. Low molecular weight aPP/aEPR blend systems, which were shown by DSC to be bulk miscible, have a surface enrichment layer which is not detectable by XPS. This places the maximum thickness of ~3 nm for the enrichment layer. In aPP/aEPR blend system with higher molecular weight aPP2, the blends were shown by DSC to be bulk immiscible, and a surface excess of aPP2 was detectable by XPS, placing a minimum thickness of 6.1±0.8nm for the excess layer. These results show that while differences in the surface activities of the individual components controls the surface monolayer composition of aPP/aEPR blends, the interaction parameter (χ_{ab},) and the bulk miscibility control the thickness of the surface enrichment layer.

5.9 Appendix 1: Estimate of aPP/aEPR7 interaction parameter, $\chi_{a\text{PP}/a\text{EPR7}}$

Our estimate of the interaction parameter between aPP and aEPR7, $\chi_{aPP/aEPR7}$, is based on the DSC observation that the aPP1/aEPR7 blend is in a single bulk phase and that the aPP2/aEPR7 blend is phase separated in the bulk. Equation 5-4, the standard free energy of mixing from Flory-Huggins theory is used as a first approximation to describe the aPP/aEPR7 blends. The first two terms on the right hand side represent combinatorial contributions to the mixing energy and the third term represents contributions from specific pair-wise interactions between aPP and aEPR7.

$$\frac{\Delta G}{RT} = \frac{\phi_{aPP}}{\left(n_{aPP} v_{aPP} / v_0\right)} \ln\left(\phi_{aPP}\right) + \frac{\phi_{aEPR7}}{\left(n_{aEPR7} v_{aEPR7} / v_0\right)} \ln\left(\phi_{aEPR7}\right) + \phi_{aPP} \phi_{aEPR7} \chi_{aPP/aEPR7} \qquad (5\text{-}4)$$

In Equation 5-4, ΔG is the molar free energy of mixing, $\phi_{aPP,aEPR7}$ are the volume fractions of aPP and aEPR7 in the blend, $v_{aPP,aEPR}$ are the molar volumes of aPP and aEPR, v_o is a reference volume (taken as $v_o = (v_{aPP} v_{aEPR7})^{1/2}$) and $n_{aPP,aEPR7}$ are the degrees of polymerization of the two polymers. Evaluation of the binodal, spinodal, and critical conditions for binary mixtures followed standard procedures and the results are given in Figure 5-12a and 5-12b for the aPP1/aEPR7 and aPP2/aEPR7 blends, respectively, as a function of the interaction parameter, $\chi_{aPP/aEPR7}$.[26] The critical composition ($\phi_{aPP,c}$), the blend composition with the highest tendency to phase separate and the corresponding critical value of the interaction parameter, χ_c, are given by:

$$\phi_{aPP,c} = \frac{\left(n_{aEPR7} v_{aEPR7} / v_0\right)^{1/2}}{\left(n_{aPP} v_{aPP} / v_0\right)^{1/2} + \left(n_{aEPR7} v_{aEPR7} / v_0\right)^{1/2}} \qquad (5\text{-}5)$$

$$\chi_c = \frac{\left\{\left(n_{aPP} v_{aPP} / v_0\right)^{1/2} + \left(n_{aEPR7} v_{aEPR7} / v_0\right)^{1/2}\right\}^2}{2\left(n_{aPP} v_{aPP} / v_0\right)\left(n_{aEPR7} v_{aEPR7} / v_0\right)} \qquad (5\text{-}6)$$

Based on Equation 5-5 and 5-6, $\phi_{aPP,c}$ and χ_c are calculated to be 0.500 and 0.00145, respectively, for the *aPP1/aEPR7* blend, and 0.3366 and 0.000821, respectively, for the unbalanced molecular weight *aPP2/aEPR7* blend. The critical conditions are marked by dotted lines in Figure 5-12a and 5-12b. From Figure 5-12a, the value of $\chi_{aPP/aEPR7}$ which would lead to phase separation of the 50:50 weight percent *aPP1/aEPR7* blend is evaluated to be 0.00145. Because this blend is *miscible* by DSC it follows that 0.00145 is a maximum value of $\chi_{aPP/aEPR7}$. From Figure 5-12b, the value of $\chi_{aPP/aEPR7}$ which would lead to phase separation of the 50:50 weight percent *aPP2/aEPR7* blend is evaluated to be 0.00087. Because this blend is *immiscible* by DSC it follows that 0.00087 is the miminum value of $\chi_{aPP/aEPR7}$.

We can further estimate $\chi_{aPP/aEPR7}$ by noting that the glass transition temperatures of the immiscible blend in Figure 5-3c are shifted relative to the pure components. The T_g of the *aEPR7*-rich phase is -43.0°C relative to -46.2°C for the pure *aEPR7* component. Similarly, the T_g of the *aPP2*-rich phase is -10.6°C relative to +0.2°C for the pure *aPP2* pure component. Mixing of the minority component in both phases causes an elevation of the T_g for the *aEPR7*-rich phase and a decrease of the T_g for the *aPP2*-rich phase. For the individual copolymers and the miscible *aPP1/aEPR7* blend, the Gordon-Taylor correlation described very well the composition dependence on the glass transition temperature.[27] Using this correlation, the compositional changes associated with the observed glass transition shifts in the 50:50 weight percent *aPP2/aEPR7* blend could be estimated, and the associated $\chi_{app/aEPR7}$ is calculated from Figure 5-11b to be 0.00102±0.00010 (the error reflects the different result calculated from the *aEPR7*-rich and *aPP2*-rich portions of the phase diagram) without any further correction for

97

temperature. This assignment also predicts that the aPP-rich phase is the dominant component relative to the aEPR7-rich phase in roughly a 60:40 ratio, which is in qualitative agreement with the smaller heat capacity change observed for the aEPR7-rich phase in Figure 5-2b.
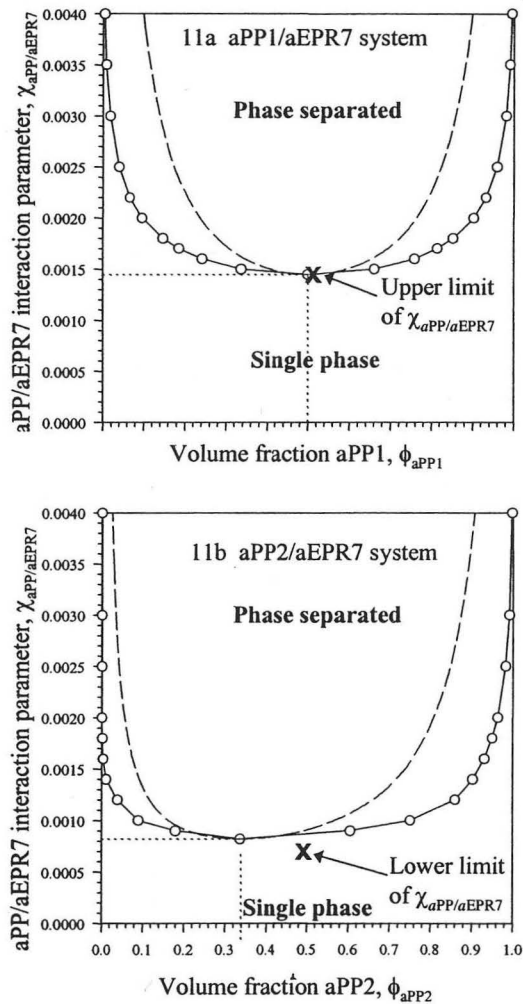
Figure 5-11: Calculated bulk phase diagrams for the blend systems (300K): (a) Phase diagram for aPP1/aEPR7 blend system. (b) Phase diagram for the aPP2/aEPR7 blend system.

5.10 Appendix 2: Extension to atactic polybutene (*a*PB) blends

In addition to *a*PP/*a*EPR blends, we have also studied the surface compositions of atactic polybutene blends (*a*PB). The *a*PB component has a lower surface tension than *a*PP and *a*EPR, thus is blends of these components *a*PB is expected to be enriched at the air interface. SFG and XPS are both capable of distinguishing *a*PB from *a*PP and from *a*EPR. The SFG spectrum of *a*PB, presented in Chapter 1, showed a significantly different $CH_3(s):CH_3(a)$ mode strength ratio and a broader $CH_2(s)$ vibration region, relative to aPP and aEPR, due to the orientation of the ethyl side branch at the interface. The valence band XPS spectrum of *a*PB is shown in Figure 5-12. The spectrum qualitatively contains the same features as the *a*PP and *a*EPR valence band spectra, however, the contribution from the peak associated with CH_2 (~20eV) is larger. Additionally, the peak associated with the sidebranch (~16eV) is shifted to lower binding energy relative to the *a*PP and *a*EPR side branch peak.
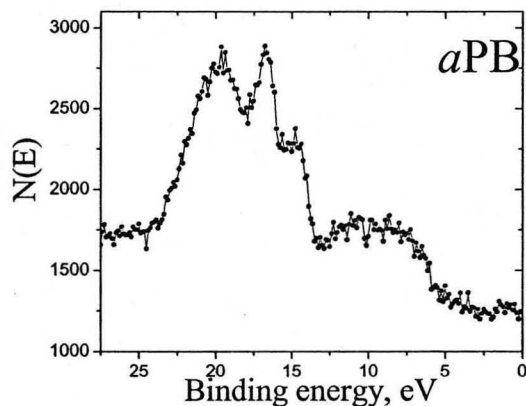
Figure 5-12: Valence band XPS spectrum obtained from an atactic polybutene (*a*PB) film.

Figure 5-13 shows an AFM image, SFG spectrum, and XPS spectrum obtained from a 50:50 weight percent *a*PB:*a*EPR7 blend annealed at 70C for 48 hours. The blend

is bulk-immiscible. The SFG and XPS spectra are similar to those obtained from the *a*PB film, suggesting enrichment of *a*PB at the air interface. The AFM image, however, shows that small circular domains cover ~5% of the surface. These domains display high friction against the sliding of the AFM tip, suggesting that they are *a*EPR, the softer component. This set of data shows that the surface morphology of bulk immiscible films is complex and that the complete wetting of the lower surface tension component observed in *a*PP/*a*EPR films *should not* be expected in all polyolefin blends. In blends of *a*PP and *a*PB (also immiscible) significant quantities of both components are measured at the air interface.
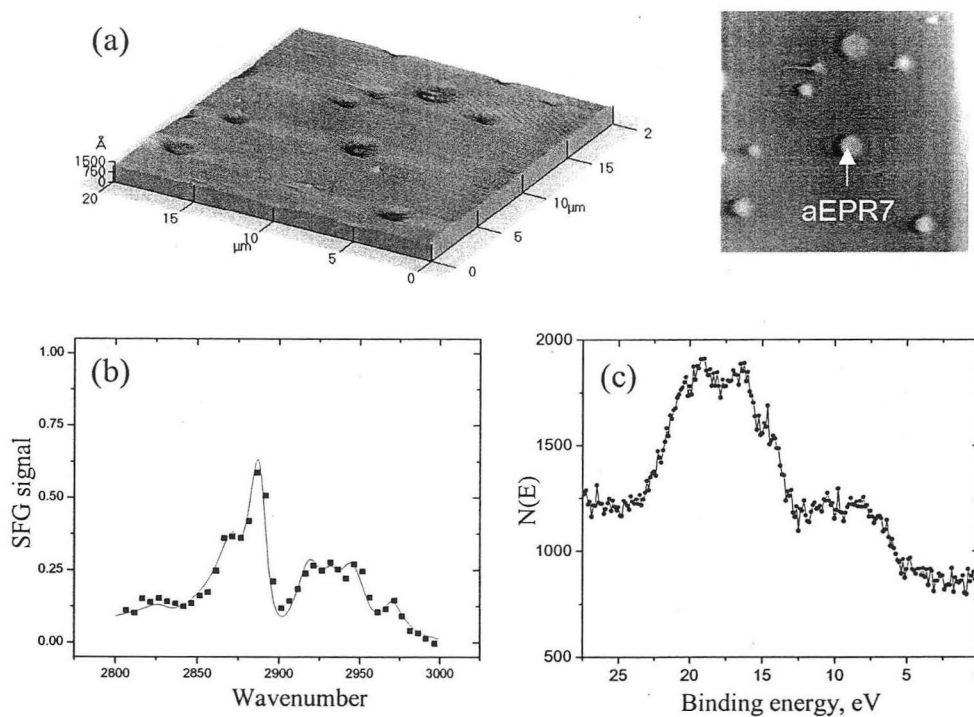
Figure 5-13: (a) AFM topography and lateral force (friction) images, (b) SFG spectrum, and (c) valence band XPS spectrum obtained from a 50:50 weight percent *a*PB:*a*EPR7 blend film annealed at 70C for 48 hours. This set of data suggests enrichment, but not complete wetting, of the *a*PB component.

100

References

[1] Scheffold, F.; Budkowski A.; Steiner U.; Eiser E.; Klein J.; Fetters L.J. *J. Chem. Phys.* **1996**, *104*, 8795.

[2] Klein, J.; Kerle, T.; Zink, F.; Eiser, E. *Macromolecules* **2000**, *33*, 1298.

[3] Budkowski, A.; Rysz, J.; Scheffold, F.; Klein, J.; Fetters, L.J. *J. Poly. Sci. B – Poly. Phys.* **1998**, *36*, 2691.

[4] Schmidt, I.; Binder, K. *J. Phys. (Paris)* **1985**, *46*, 1631.

[5] Wu, D.T.; Fredrickson, G.H. *Macromolecules* **1996**, *29*, 7919.

[6] Donley, J.P.; Wu, D.T.; Fredrickson, G.H. *Macromolecules*, **1997** *30*, 2167.

[7] Kokkinos, I.G.; Kosmas, M.K. *Macromolecules* **1997**, *30*, 577.

[8] Zink, F.; Kerle, T.; Klein, J. *Macromolecules* **1998**, *31*, 417. (ps)

[9] Zhao, X.; Zhao, W.; Sokolov, J.; Rafailovich, M. H.; Schwarz, S. A.; Wilkens, B. J.; Jones, R. A. L.; Kramer, E. J. *Macromolecules* **1991**, *24*, 5991.

[10] Jones, R.A.L.; Kramer, E.J.; Rafailovich, M.H.; Sokolov, J.; Schwartz, S.A. *Phys. Rev. Lett.* **1989**, *62*, 280.

[11] Zhang, D; Shen, Y.R.; Somorjai, G.A. *Chem. Phys. Lett.* **1997**, *281*, 394.

[12] Gracias, D.H.; Zhang D.; Lianos, L.; Ibach, W.; Shen, Y.R.; Somorjai, G.A. *Chem. Phys.* **1999**, *245*, 277.

[13] Opdahl, A.; Phillips, R.A.; Somorjai, G.A. *J. Phys. Chem B* **2002**.

[14] Jones, R.A.L. *Polymer* **1994**, *35*, 2160.

[15] Galuska, A.A.; Halverson, D.E. *Surface and Interface Analysis* **1998**, *26*, 425.

[16] Wei, X.; Hong, S.C.; Zhuang, X.W.; Goto, T.; Shen, Y.R. *Phys. Rev. E*, **2000**, *62*, 5160.

[17] Miranda, P.B.; Shen, Y.R. *J. Phys. Chem. B* **1999**, *103*, 3292-3307.

[18] Roberts, R.F.; Allara, D.L., Pryde, C.A., Buchanan, D.N.E.; Hobbins, N.D. *Surf. Interface. Anal.* **1980**, *2*, 5.

[19] Briggs, D. Surface Analysis of Polymers by XPS and Static SIMS, Cambridge University Press, **1998**, Chapter 2.2, pages 27-46.

[20] Briggman, K.A.; Stephenson, J.C.; Wallace, W.E.; Richter, L.J. *J. Phys. Chem. B* **2001**, *105*, 2785.

[21] Wang, J; Chen, C.Y.; Buck, S.M.; Chen, Z. *J. Phys. Chem. B* **2001**, *105*, 12118.

[22] Oh-e, M.; Lvovsky, A.I.; Wei, X.; Shen, Y.R. *J. Chem. Phys.* **2000**, *113*, 8827.

[23] Mansfield, K.F.; Theodorou, D.N. *Macromolecules* **1990**, *23*, 4430.

[24] Clancy, T.C.; Jang, J.H.; Dhinojwala, A.; Mattice, W.L. *J. Phys. Chem B*, **2001**, *105*, 11493.

[25] Segment length is defined here as $a = \dfrac{R_{g,w}}{(N_w/6)^{1/2}}$ where $R_{g,w}$ is the radius of gyration and N_w is the degree of polymerization. The weighting of component a-values in the blend is according to reference 8.

[26] Strobl, G. The Physics of Polymers, Springer-Verlag, Berlin, **1996**.

[27] Gordon, M.; Taylor, J.S. *J. Appl. Chem.* **1952**, *2*, 493: and Wood, L.A. *J. Polym. Sci.* **1958**, *28*, 319.

Chapter 6

Solvent and interface induced surface segregation in blends of isotactic polypropylene with poly(ethylene-co-propylene) rubber

6.1 Introduction

The equilibrium surface compositions of polymer blends have been extensively studied, both experimentally[1,2,3,4,5] and theoretically[6,7,8,9], as demonstrated in the previous Chapter. In practical applications, however, a polymer blend may be far from equilibrium, and factors related to the processing conditions may dictate the surface composition. In this Chapter, the surface composition and morphology of a model immiscible blend of isotactic polypropylene (*i*PP) with aspecific poly(ethylene-co-propylene) rubber (aEPR), whose structure facilitates experimentation while simulating the important class of commercial isospecific PP/EPR blends, has been characterized.[10]

A specific motivation for studying the surface compositions of iPP/EPR blends is that iPP and iPP/EPR blends are difficult to paint and require extensive pretreatment with either flame treatment or solvent-based adhesion promoter.[11,12,13] Blending EPR with iPP increases the paintability, presumably due to a high concentration of low crystallinity/highly permeable EPR in the near surface region – although the true role of EPR is uncertain. In solvent-based systems, the solvent used to carry the adhesion promoter also tends to be a good solvent for the EPR phase and consequently may affect the surface composition after application. Additionally, surface hardness, scratch resistance, printability, and optical properties may be influenced by surface composition/morphology. Knowledge of how various processing conditions affect the surface morphology and chemical composition may give insight into these types of problems.

For mixtures of polyolefin copolymers, the copolymer with lower surface tension has a tendency to segregate to the air/polymer interface. In general, however, immiscible blends can exhibit a variety of complex morphologies at interfaces, and complete wetting of the lower surface tension component at the open interface is not always observed for phase separating systems (see, e.g. refs 14,15 and references therein). The behavior is even more complicated for thin spin cast films, where the underlying substrate plays a role in directing the morphology at both interfaces. Additionally, in spin cast films, the casting solvent can affect the initial surface morphology of immiscible blends - and the surface tension, miscibility, and solubility of the blend components have been observed to influence the surface morphology.[16]

104

In this chapter, atomic force microscopy (AFM), optical microscopy, and x-ray photoelectron spectroscopy (XPS) have been used to characterize the surface morphologies of relatively thick iPP/aEPR wafers prepared under different conditions. The previous chapter examined single phase and two phase amorphous atactic polypropylene (aPP)/aEPR miscible and immiscible blends and showed that aPP, the lower surface tension component, wet the open interface in both systems. In the iPP/aEPR blend, the crystalline nature of the iPP traps, via crystallization on cooling, surface morphologies prepared in the melt state that vary depending on the processing conditions. The surfaces of iPP/aEPR blends melt-processed in open air are compared to the surfaces of melt-pressed samples and to the surfaces of samples exposed to a post-melt treatment of n-hexane vapor, which is a good solvent for aEPR at room temperature, but not for the iPP component.

6.2 Experimental procedures

Polymers Table 6-1 summarizes the relevant physical properties of the iPP and aEPR samples used in the blend. Dibutylsilylbis(9-fluorenyl)zirconium dichloride catalyst was used to prepare the aEPR copolymer in hexane with a methylaluminoxane (MAO) activator at 70°C polymerization temperature and a molar [Al]/[Zr] ratio of 2000-3000. Closely related analogs to this aspecific catalyst have been published previously.[17] The aEPR copolymer is amorphous and completely soluble in hexane at room temperature. While the molecular weight of the aEPR copolymer is much lower than commercial EPR rubber, the low molecular weight facilitates experiments by greatly increasing mobility and rates of phase growth in the immiscible blend.

Table 6-1: Structural characteristics of the *i*PP and the *a*EPR copolymer used in the 50:50 wt. % iPP/*a*EPR blend.

Sample	M_w	M_w/M_n	wt. % ethylene	$[CH_2]/[CH_3]_{bulk}$	Sequence parameter[b]
*i*PP	220,000	4.0^a	0	1	-
*a*EPR	54,000	1.91	29.7	1	1.4

[a] rheological index: generally less than true Mw/Mn
[b] The sequence parameter, determined by NMR, is a measure of the randomness of the copolymer. It is 1 for a completely *random* distribution of comonomers, 2 for complete *alternation* of comonomers, and 0 for complete *block*-like sequencing.

The *i*PP component is based on Ziegler-Natta technology and has a broad molecular weight distribution. The 50:50 wt. % *i*PP/*a*EPR blend was prepared in a stabilized 3% xylene solution under a nitrogen environment at 130°C. Blends were precipitated in dry-ice chilled methanol, washed, and vacuum dried at 75°C. The blend with iPP is closely analogous to a previous model aspecific immiscible blend.[5] The tacticity of the homopolymer and the composition of the *i*PP/*a*EPR blend was verified by ^{13}CNMR using a Varian UNITY-300 spectrometer at 75.4 MHz in 10% orthodichlorobenzene solutions at 130°C. Ethylene content of the *a*EPR copolymer was determined from the compositional triads.

Wafers that were ~1mm thick were prepared by melting the blend in a nitrogen rich atmosphere at 200°C on a homebuilt temperature controlled heating stage. For the air-melted samples, the blend was first melt-pressed for 30s in order to produce a flat sample. The blend is highly unstable and rapidly phase separates at longer melt times, suggesting that 200°C is below the critical temperature.[18] After melt pressing, the wafer was quenched in liquid nitrogen and the top plate was removed for a subsequent melt in air (5, 10, and 20 min melt). Samples with this

history are referred to as "air-melt" samples. Other samples were pressed for longer periods of time (5, 10, and 20 min) and quenched in liquid nitrogen with subsequent removal of the top substrate. Samples with this history are referred to as "melt-pressed" samples. Two types of pressing substrates were used: (1) hydrophilic glass - ordinary glass cleaned in piranha solution (9 parts concentrated H_2SO_4: 1 part 20% H_2O_2) and (2) hydrophobic glass – ordinary glass which has a hydrophobic octadecyl silanol self-assembled monolayer (SAM) bound to the surface.[19] The RMS roughness of the clean glass is typically <2nm (measured by AFM on 15x15μm areas). The glass has no discernable texture except for occasional scratches and chips.

To simulate how a solvent-based adhesion promoter, which can preferentially solvate the aEPR component, affects the surface composition, some of the iPP/aEPR samples were exposed to n-hexane vapor after melt pressing. Blend wafers melt pressed for 30s at 200°C were placed inside a sealed dish containing a small amount of liquid n-hexane (Aldrich, 98%) - a good solvent for the aEPR component but not for the iPP component at room temperature. The sample rests on a shelf in the dish and is not directly exposed to liquid n-hexane but is exposed to n-hexane vapor. After the n-hexane vapor treatment, the blend wafers were oven dried at 50°C for 3 hrs to remove residual solvent.

Atomic Force Microscopy (AFM) AFM measurements were made using a Park AFM fitted with an M5 head, capable of scanning 100μmx100μm regions. Cantilevers with force constants ranging from 0.03 to 1N/m (NT-MDT) were used to obtain topographic images of the surfaces under low contact loads. Higher force constant cantilevers (2 N/m, NT-MDT) were used to obtain images using the non-

contact scanning mode. The photodiode detector was calibrated to the cantilever by collecting force vs. distance curves on silicon and using the nominal value of the cantilever force constant given by the manufacturer. A video microscope attached to the AFM, was used to characterize larger scale phase separation. The illumination and camera objective are both focused on the topside of the polymer film. The camera collects the light reflected off the sample and is sensitive to the reflectivity and roughness of the surface region. The microscope was focused on the sample surface using the AFM cantilever as a reference point.

X-Ray Photoelectron Microscopy (XPS) XPS experiments were performed using the instrument described in Chapter 5. The sampling depth of the XPS experiments is based on an attenuation length of 2.9±0.4nm measured by Roberts et al. for photoelectrons ejected from polymethylmethacrylate (PMMA) having a kinetic energy of 1200eV.[20] Using this value as an approximation for the attenuation length of valence band photoelectrons generated by the Kα x-ray source (kinetic energy of photoelectrons ~1240eV) leads to a 95% sampling depth of 6.1±0.8nm.[21]

6.3 Results

Distinguishing iPP and EPR by AFM Tomasetti et al. have previously shown that AFM is sensitive to the difference in mechanical properties between a crystalline *i*PP phase and a nearly amorphous EPR phase, and can readily distinguish the two at the surface.[22,23] An optical microscope image and corresponding AFM images taken in contact imaging mode of our *i*PP/*a*EPR blend sample which was melt-pressed at 200°C for 30s between hydrophobic treated glass are shown in Figure 6-1. The optical image in Figure 6-1a shows that the surface is heterogeneous and is

comprised of small clusters of crystalline spherulitic structures characteristic of *i*PP (light) and an amorphous phase (dark). In the AFM topography image in Figure 6-1b, the amorphous regions are depressed by the AFM cantilever load and have dark contrast while the crystalline phase are not depressed and show up as light regions. The AFM lateral force image shown in Figure 6-1c indicates that the two phases have different friction properties – the amorphous phase displays higher friction (is lighter) than the crystalline phase.
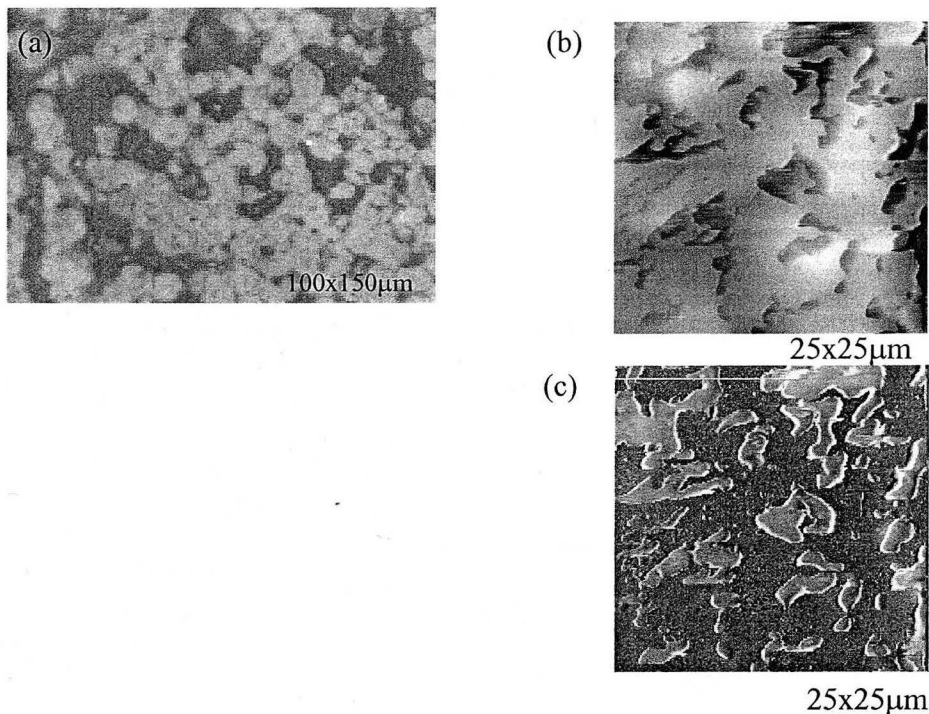
Figure 6-1: (a) 100x150μm optical image of *i*PP/*a*EPR melt pressed between hydrophobic glass 30 s at 200°C and quenched in liquid nitrogen showing crystalline *i*PP spherulites and an amorphous phase (dark). (b) 25x25μm AFM contact mode topography image and corresponding (c) 25x25μm AFM lateral force (friction) image. The high friction regions (light) correspond to depressed regions on the topography image (dark) and are assigned as *a*EPR.

AFM scans taken over the same line at loads of 1.25, 2.5, and 5nN are shown in Figure 6-2a. As the tip scans from left to right it first passes over a crystalline phase, and then a soft phase - where the tip sinks into the surface at a constant rate as it scans across, until it encounters a second crystalline phase and rises up. Scanning across the surface with higher load increases the rate at which the tip sinks into the soft phase, but does not affect the topology of the crystalline phase.

The rate that the AFM tip sinks into the surface as it slides across an amorphous region under a given load (z-strain) can be quantified by measuring the distance that the tip sinks into the surface, Δz (μm), and dividing by the time that it took the tip to sink that distance (Figure 6-2b). The time, Δt, is the x-scan distance (μm) divided by the scan rate (μm/s). A plot of the z-strain rate as a function of the scanning load is given in Figure 6-3a, and shows that the strain rate responds linearly under the loading conditions of the AFM. Figure 6-3b is a plot of the sinking rate as a function of the scan rate for two fixed loads, 2.5nN and 5nN, that shows there is no dependence of the tip sinking rate on the scan rate. From these observations it is concluded that the soft phase is aEPR and can be correlated to the dark regions in the optical image of Figure 6-1a and that the crystalline phase is iPP and can be correlated to the light regions in the optical image.
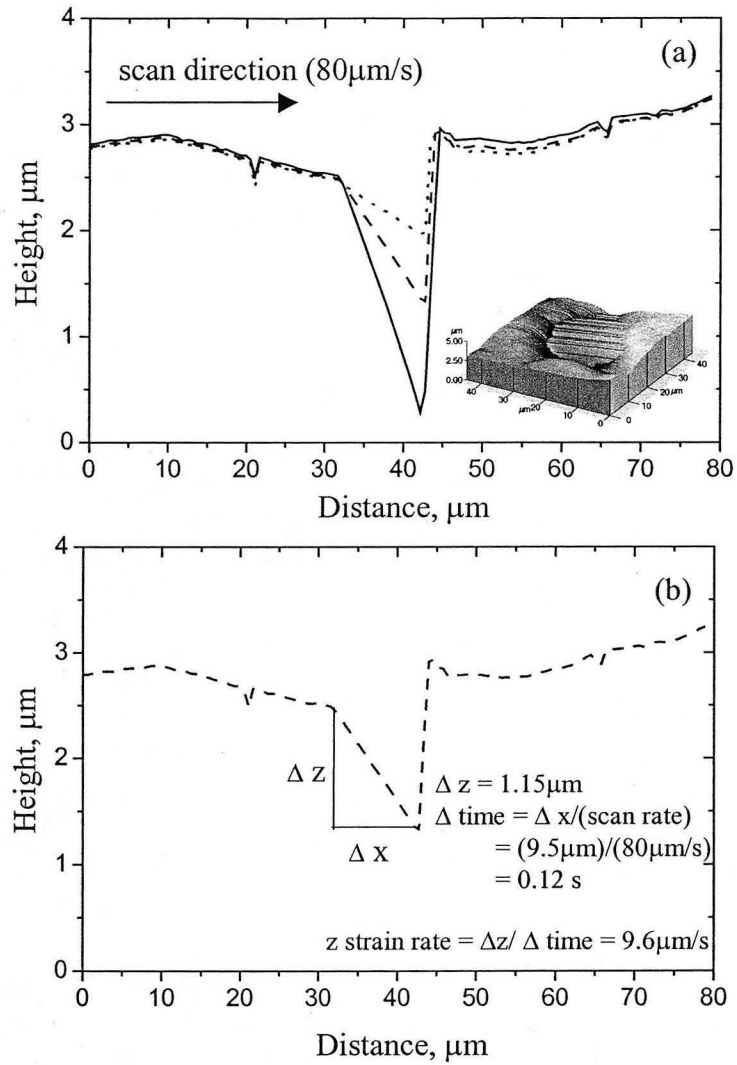
Figure 6-2: (a) AFM topography linescans showing (left to right) a crystalline, amorphous, and a second crystalline phase. The amorphous phase is distinguished from the crystalline phase by scanning at different loads: (dotted) 1.25nN load, (dashed) 2.5nN load,(solid) 5nN load. Scan direction is left to right at 80μm/s. (b) Schematic of the method used to quantify the sinking rate (~z-strain rate) of the AFM tip into the soft *a*EPR phase under a fixed load.

111
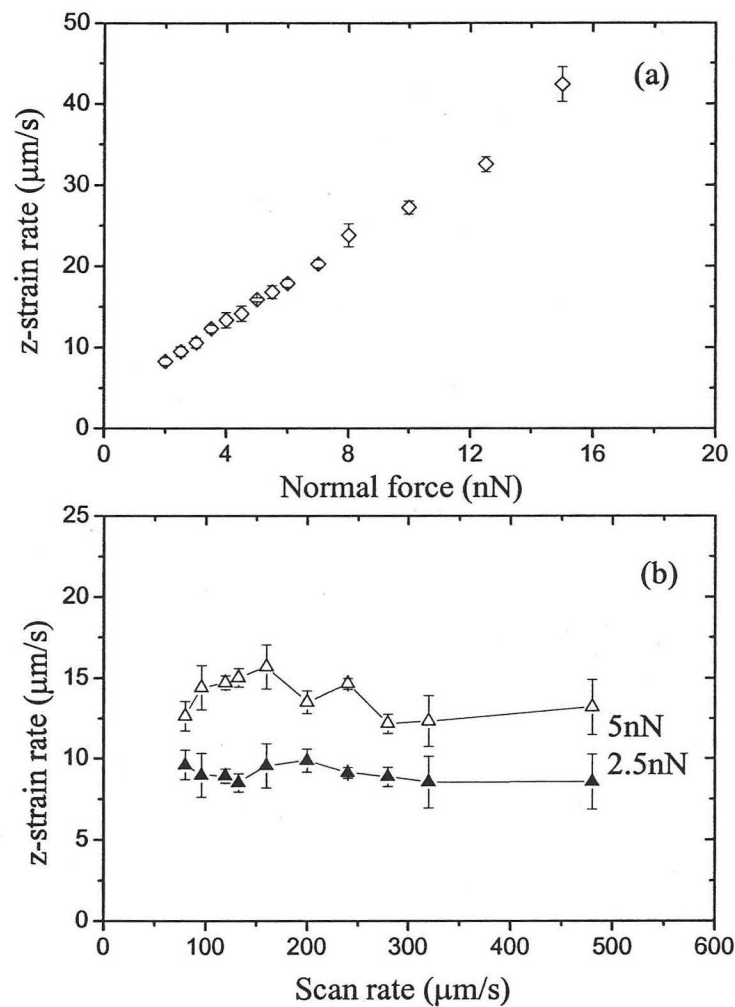
Figure 6-3: (a) Load dependence of the z-strain rate (sinking rate) of the AFM tip into the soft phase. The linear relationship between the scanning load and the sinking strain rate indicates that the soft phase behaves in the linear viscoelastic regime and that it is *a*EPR. (b) AFM scan rate dependence of the strain rate (sinking rate) of the cantilever into the soft *a*EPR phase, (▲) 2.5nN load, (△) 5nN load.
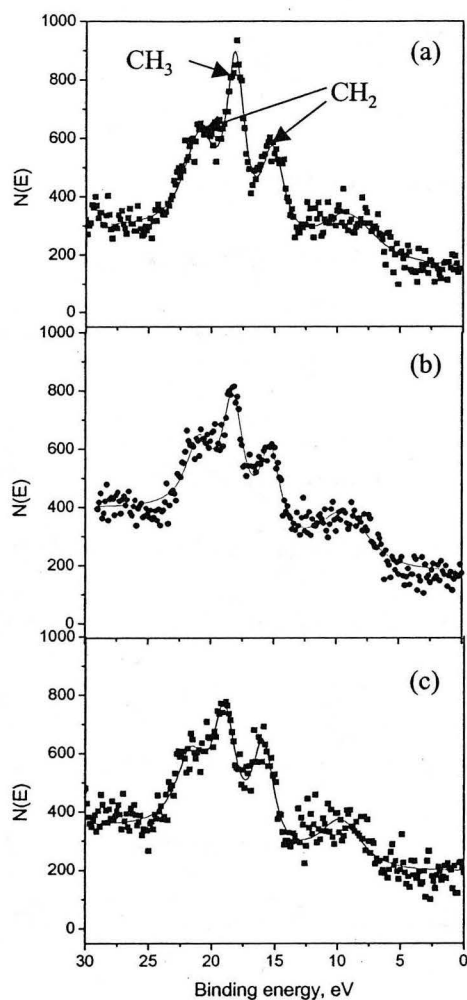
Figure 6-4: Carbon 2s valence XPS spectra of (a) *i*PP, (b) 50:50 wt. % *i*PP/*a*EPR blend melt pressed for 30 s, (c) *a*EPR. The CH_2:CH_3 peak intensity ratio of the *i*PP/*a*EPR blend is intermediate to the two pure components indicating that after a 30s melt press, both *i*PP and *a*EPR are present at the surface.

Distinguishing *i*PP and *a*EPR by XPS XPS has been used to identify the composition of the top 6.1±0.8nm of the films. Carbon valence band XPS spectra of *i*PP, the *a*EPR copolymer, and the 50:50 wt% *i*PP/*a*EPR blend which was melt-pressed for 30s are shown in Figure 6-4. In Chapter 5, carbon valence band spectra

were shown to be sensitive to differences in CH_2:CH_3 surface content of polyolefin blends and copolymers.[5,24] Valence XPS spectra of both iPP and aEPR have peaks at 15eV and at 21eV that are assigned to the 2s bonding and antibonding orbitals from the -CH_2- backbone units of the polymers. Both iPP and aEPR have an additional feature at 18eV that is two overlapping peaks, assigned to the 2s bonding and antibonding orbitals of the pendant CH_3 group. The broad feature at 9eV arises from the carbon 2p band.

The valence band XPS spectra of aEPR has smaller CH_3 features relative to the CH_2 features, compared to the valence band spectra of iPP, consistent with the lower methyl content of the aEPR copolymer. The melt pressed blend has features that are intermediate to iPP and aEPR indicating that after a brief melt press, both components are at the surface. To quantify the CH_2:CH_3 peak area ratio, after background subtraction, each valence band spectra has been fit to four peaks. The best-fit spectra for iPP and aEPR are represented by the solid lines, which are also presented in Figure 6-4.

The aspecific random aEPR copolymers, described in Chapter 5, were used as a calibration series for the XPS experiments. The calibration plot of the ratio of the CH_2:CH_3 fitted peak areas as a function of the bulk ethylene content (CH_2:CH_3 ratio), yields a linear relationship for the aEPR copolymer series and is presented in Figure 6-5. The calibration plot is used in these experiments to characterize the iPP and aEPR composition of the top few nanometers of the 50:50 wt% iPP/aEPR blend films. Due to the random nature of the aEPR copolymers and the relatively deep penetration depth of the XPS experiments, no significant surface segregation of

propylene monomers is observed. The XPS CH_2:CH_3 peak area ratios are also shown in Figure 6-5 for the air-melt, melt-presses, and solvent vapor treated blend surfaces.
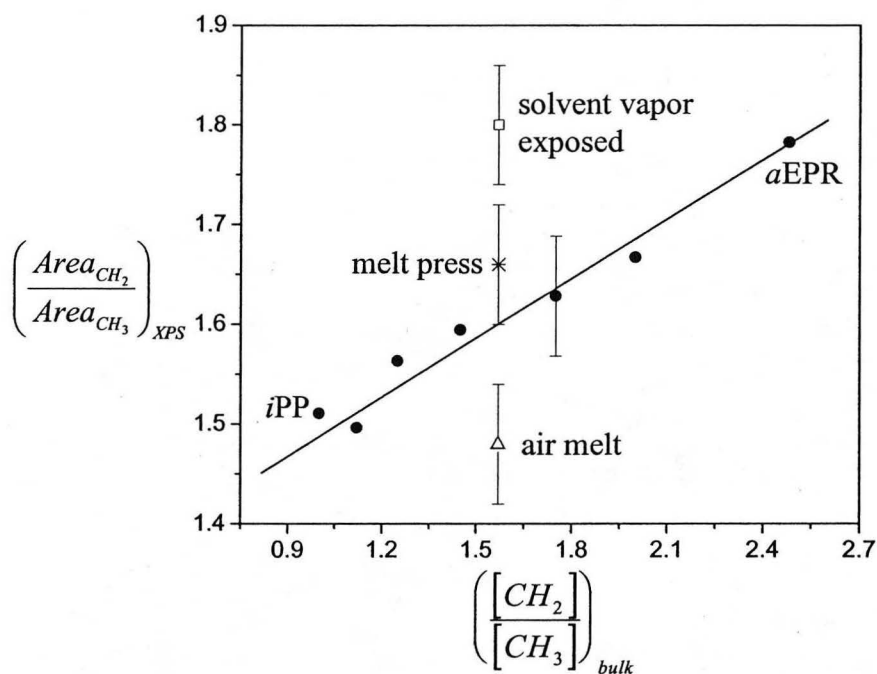
Figure 6-5: Valence XPS calibration curve (●) generated from the *a*EPR samples descibed in Chapter 2. The CH_2:CH_3 XPS peak area ratio increases as the ethylene content of the surface region increases. CH_2:CH_3 XPS peak area ratios for the (Δ) 5 min air melt sample showing an *i*PP rich surface (*) 5 min melt press sample showing a mixed iPP: *a*EPR composition and (□) after exposure to n-hexane vapor showing an *a*EPR rich surface. The point labeled '*a*EPR' refers to the *a*EPR copolymer used in the blend.

Surfaces of blends melted in air (air/polymer interface) Optical microscope images of *i*PP/*a*EPR blends melted under a nitrogen rich atmosphere for 5

and 20 minutes are shown in Figure 6-6a and 6-6b, respectively. AFM topographic and lateral force images of the blend are shown in Figure 6-6c and 6-6d(20 min melt). After the 5 min melt, the optical image shows that the crystalline iPP domains seen in Figure 6-1a have coalesced and appear to be the dominant phase. Using the AFM as a probe, the dark regions on the optical image in Figure 6a can be correlated to aEPR and the light regions to iPP - as in Figure 6-1a.
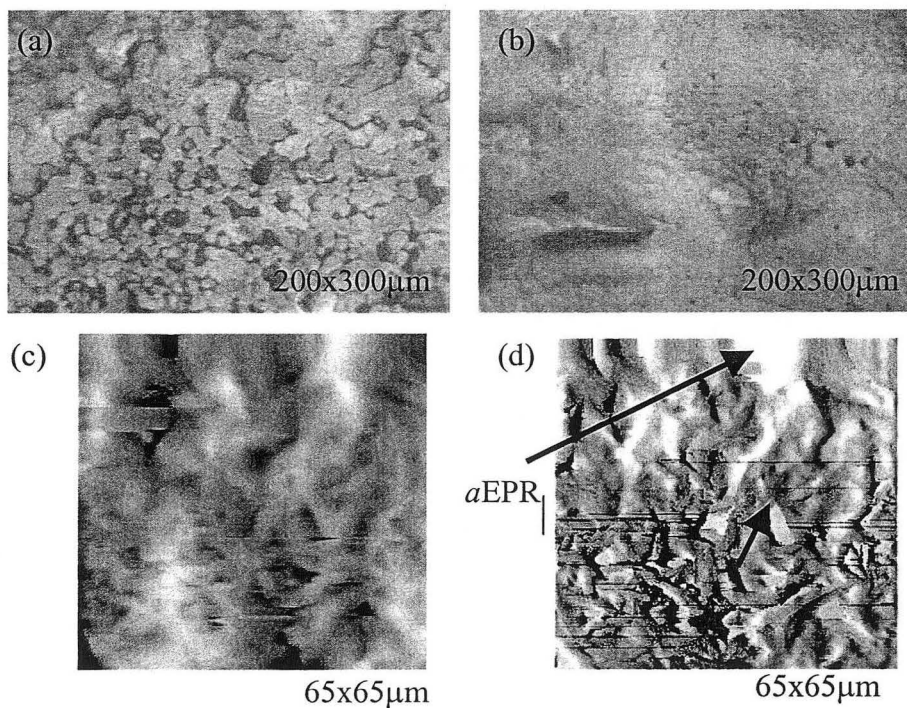
Figure 6-6: (a) 200x300μm optical image of the iPP/aEPR blend melted in air for 5 minutes at 200°C and (b) 20 minutes. (c) 65x65μm AFM topography image and (d) lateral force image of the blend melted in air for 20 minutes at 200°C. The crystallinity of the surface increases with melt time indicating that iPP segregates to the air-melt interface.

116

The XPS valence band spectrum taken after a 5 min melt is shown in Figure 6-7a. The CH_2:CH_3 peak area ratio determined from the XPS spectra is plotted on the calibration curve in Figure 6-5 and confirms an *i*PP rich surface after the brief melt period. The ratio of the CH_2:CH_3 peak areas for the air melt blend is similar to that of pure polypropylene and indicates that there is not a thin overlayer of *a*EPR, which the AFM experiments may be insensitive to. After a 20 min melt, the surface is nearly completely covered by *i*PP. The AFM images show that the majority of the surface is rough and crystalline, indicating that *i*PP segregates to the air surface. Although the surface is largely crystalline, a few small domains that display high friction are discernable in the AFM topography and lateral force images in Figure 6-6c and 6-6d. The high friction regions show up as depressed regions in the topography images, are smooth (no evidence of crystallinity), have the same load dependent behavior as the domains in Figure 6-1b - and are therefore assigned as *a*EPR.
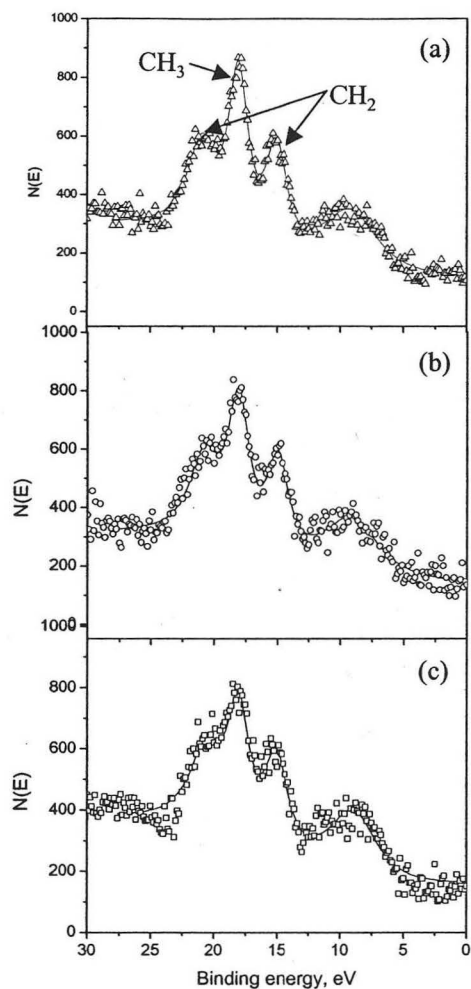
Figure 6-7: (a) Valence band XPS spectra of the *i*PP/*a*EPR blend after a 5 minute melt in air at 200C showing that the surface is enriched in iPP (b) Valence band XPS spectra of the blend after melt pressing for 5 minutes at 200°C showing that both *i*PP and *a*EPR are present and (c) Valence band XPS spectra of the blend after melt pressing for 30s and then exposing to n-hexane vapor for 15 minutes indicating that the surface is enriched in *a*EPR.

Melt-pressed blends (polymer/substrate interface) Optical images of the
*i*PP/*a*EPR melt pressed for 5 and 20 minutes between hydrophobic treated glass are
shown in Figure 6-8a and 6-8b. These images show a different surface phase behavior
than the samples with the "air melt" history and indicate that both *i*PP and *a*EPR
phases are present at the surface. However, the light and dark contrast used to
distinguish the *i*PP and *a*EPR phases in Figure 6-1a is not observed in the Figure 6-8a
and 6-8b, where the melt-press time is longer and the degree of phase separation is
larger. Specifically, Figure 6-8a shows a heterogenerous surface that contains liquid-
like droplets and crystalline regions at the surface. The droplets coalesce into larger,
laterally phase separated droplets as the melt time increases and cover roughly half of
the surface.

An AFM topography image and corresponding lateral force image taken of
the 5 min melt-press sample are shown in Figure 6-8c and 6-8d. By AFM, it can be
shown that the *a*EPR domains are the smooth and light colored regions in the optical
image in Figure 6-8a,b. When AFM scans are taken under low loads (<0.1nN) and
rapid scanning rates (>80μm/s), the tip does not significantly sink into the soft *a*EPR
phase. The AFM images shown in 6-8c and 6-8d show a region that contains a large
droplet and several smaller droplets. The large droplet appears smooth, amorphous,
and is raised from than the surrounding material. The friction image shows that the
droplets have higher friction than the surrounding material. Scanning under higher
load, the droplets compress into the surface, and display mechanical behavior like that
seen in Figure 6-2a. Thus, it is concluded that the droplet-like regions are *a*EPR and
that both *i*PP and *a*EPR are the surface. The contrast between *i*PP and *a*EPR in the

optical images is likely a result of differences in height and surface texture between the amorphous and surrounding crystalline phase. After the 20 min melt, the individual phases are generally too large to be completely imaged by the AFM.
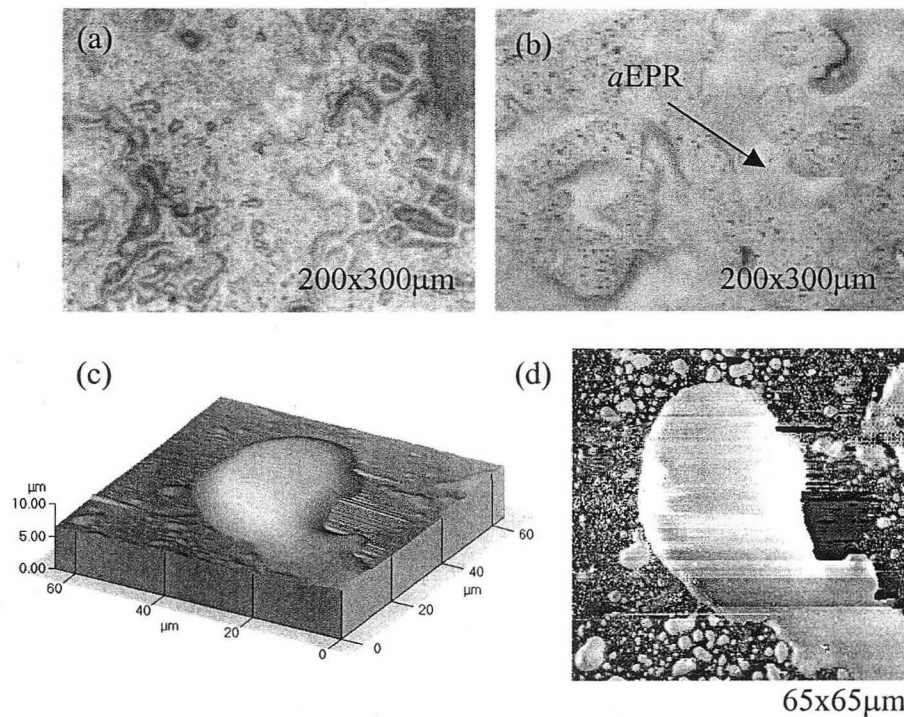
Figure 6-8: (a) 200x300μm optical image of *i*PP/*a*EPR blend melt pressed between hydrophobic glass for 5 minutes at 200°C and (b) 20 minutes (c) 65x65μm AFM topography and (d) lateral force image of the blend melt pressed for 5 minutes at 200°C. The images show that both *i*PP and *a*EPR are present at the surface and that lateral phase separation increases with melt time. The topography image shows that the *a*EPR domains are raised out of the surface

The valence band XPS results confirm a mixed iPP/aEPR surface composition for the melt pressed samples. An XPS spectrum taken after a 5 min melt press is shown in Figure 6-7b. The spectrum is similar to the spectra in Figure 6-4b taken of the blend sample that was melt-pressed for 30 s. The CH_2:CH_3 peak area ratio is plotted on the calibration curve in Figure 6-5 and is intermediate to the pure components. Both phases are present at the interface in roughly equal proportion. The valence XPS spectrum after a 20 min melt press is virtually indistinguishable from the valence XPS spectrum of the sample melt pressed for 5 min indicating that neither component segregates to the hydrophobic interface.

Similar results are obtained using hydrophilic treated glass. Using hydrophilic treated glass, however, there is much stronger adhesion between the blend and the substrate, which is not observed for melt pressed iPP but is observed for melt pressed aEPR. Blend samples melt pressed under hydrophilic glass can only be removed at liquid nitrogen temperature, hence the blends do not exhibit iPP segregation. This indicates that the suppressed segregation of iPP to the confined interface is not related to hydrophobic/hydrophilic interactions between the blend and the substrate, but may be related to packing at the polymer/solid interface.

Effect of solvent vapor To determine how preferential solvation affects the surface composition of the iPP/aEPR blend, samples melt pressed for 30s were exposed to a post-melt n-hexane vapor treatment by placing a blend wafer inside a sealed dish containing a small amount of liquid n-hexane, where the surface is exposed to vapor but not directly exposed to the liquid n-hexane. Optical images of a sample exposed to saturated n-hexane vapor for 15 minutes and a sample treated for

121

30 minutes are shown in Figures 6-9a and 6-9b, respectively. A non-contact AFM image is shown in Figure 6-9c.

The color contrast in the optical image after the 15 min exposure is similar to the contrast in Figure 6-8c, where the aEPR domains appeared liquid-like and smooth. After a 30 min exposure, the surface of the sample is flat and featureless, indicating that the amorphous aEPR totally coats the surface. An AFM topography image taken using the non-contact (zero load) imaging mode is shown in Figure 6-9c shows an amorphous and featureless surface.

(a)

aEPR

200x300μm

(b)

200x300μm

(c)
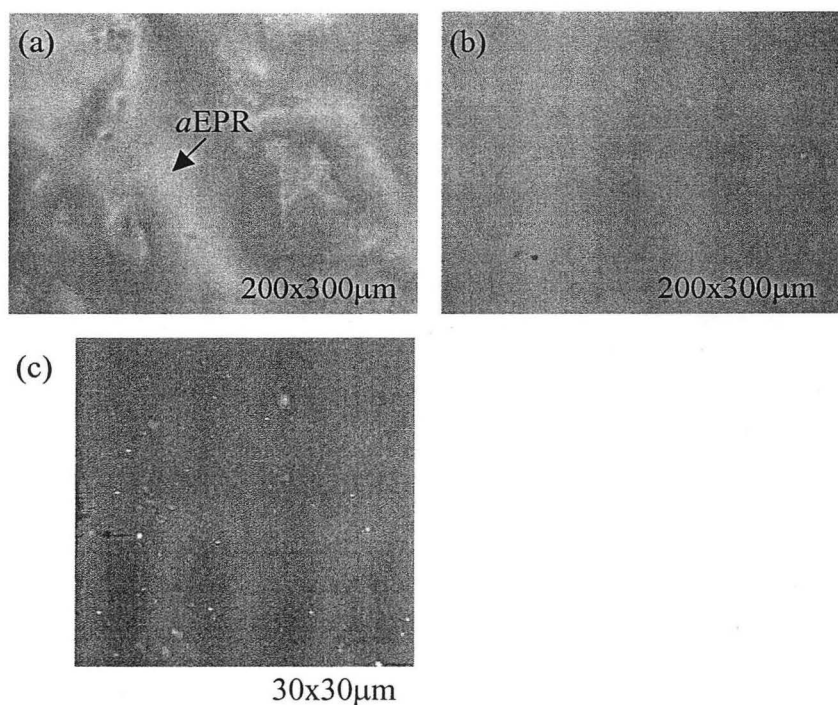
30x30μm

Figure 6-9: (a) 200x300μm optical image of the iPP/aEPR blend melt pressed between for 30s and then exposed to n-hexane vapor for 15 minutes (b) 200x300μm optical image and (c) 30x30μm AFM non-contact topography image of the iPP/aEPR blend melt exposed to solvent vapor for 30 minutes. The images show that the surface becomes amorphous indicating aEPR is preferentially solvated by the n-hexane and is drawn to the surface.

122

The valence band XPS spectrum taken of the sample exposed for 30 min is shown in Figure 6-7c and is qualitatively similar to the XPS spectra of aEPR shown in Figure 6-4c. The CH_2:CH_3 peak area ratio determined from the XPS spectrum is plotted in Figure 6-5 and is similar to the ratio determined for pure aEPR, confirming an aEPR rich surface. These results indicate that the aEPR in the blend is preferentially swollen or solvated by the hexane, and drawn onto the surface.

6.4 Discussion

In commercial applications, blends of iPP and EPR are most often injection molded. In these cases, it is well known that the iPP/EPR moldings show highly striated two-phase morphologies near the mold surface, the orientation of which is highly dependent on resin structure.[10] There is no preference for either component in the macroscopic "skin" layer,[10] though the composition in the near surface regions is not clear. Tomasetti et al. have shown that injection molded iPP/EPR blends are enriched in iPP at the surface while compression molded blends contain both iPP and EPR.[23] In those experiments, the enrichment of iPP in the oriented injection moldings was explained in terms of the lower melt flow viscosity of iPP compared to EPR. Transmission electron microscopy (TEM) evidence disputes claims of a near surface iPP overlayer in injection molded iPP/EPR blends though the resin structure wasn't specified.[25] The present results show that even for a highly idealized system in the absence of flow, that the surface morphology of iPP/aEPR blends is complex and is strongly dependent on processing conditions and surface environment.

The different surface compositions and phase behaviors observed in this study (in the absence of flow) for the air melt, melt pressed, and solvent vapor exposed *i*PP/*a*EPR blend samples are summarized in Table 6-2. When the *i*PP/*a*EPR blend is processed in open air, *i*PP segregates to the air interface. Segregation of *i*PP to the air interface is consistent with previous observations on the completely amorphous atactic polypropylene(*a*PP)/*a*EPR blend system.[5] Those results showed that *a*PP preferentially segregated to the air/polymer interface for low molecular weight miscible systems and also for high molecular weight immiscible systems. For the bulk immiscible *a*PP/*a*EPR blend, which had similar molecular weight characteristics as the *i*PP/*a*EPR blend used in this study, it was shown that *a*PP completely wetted the surface at the air interface and that the enrichment layer was at least 6-8 nm deep.

Processing Condition	Optical Microscope	AFM	XPS
air melt	single phase	crystalline	*i*PP
melt press	phase separated	crystalline and amorphous phases	mixed *i*PP and *a*EPR
solvent exposed	single phase	amorphous phase	*a*EPR

Table 6-2: Summary of surface morphologies observed by optical microscopy and atomic force microscopy and the surface compositions measured by XPS for the *i*PP/*a*EPR blend system.

The surface segregation tendency of *i*PP is suppressed at solid interfaces. Both *i*PP and *a*EPR components are present at the interface for melt-pressed samples. Entropy and enthalpy arguments have also been used to explain the behavior of polymer blends at confined interfaces.[4,9] Packing entropy is an important variable[9] and

124

it has been argued that although chain backbones tend to lie parallel to the surface at both open and confined interfaces, the tendency for backbones to be parallel to the surface is much stronger at the higher density solid interface. This may favor enrichment of the high ethylene content EPR component, which may have more backbone bonds in trans conformations - leading to better packing against the interface. An enthalpy argument suggests that many of the interchain interactions that are lost at the open interface are partially compensated for by interactions with the solid substrate, leading to a reduced segregation tendency of the more branched component.[4] The observation that both hydrophilic and hydrophobic substrates, which should have different affinities for the iPP and aEPR components, suppress the segregation of iPP suggests that packing forces may be the dominant mechanism for the iPP/aEPR blend.

After melt pressing, the surface of the blend can be enriched in aEPR by exposing the sample to a vapor that is a good solvent for the aEPR phase. The results of Chapter 2 suggests that when the blend is exposed to n-hexane vapor, which has a lower surface tension than both the iPP and aEPR components, that the surface is coated by n-hexane. The n-hexane rich surface solvates/swells the more permeable aEPR and draws it to the surface. This process requires the presence of aEPR at the surface, further supporting the morphological observations in the melt pressed samples. The aEPR domains were shown to "stick out" of the surface for the melt pressed blends. Extending these idealized studies to the problem of paintability of iPP/aEPR blends, the results indicate that solvent-based adhesion promoters, which generally contain more aggressive solvents than those investigated here, may have the

ability to "reconstruct" the near-surface regions by drawing the aEPR out onto the surface. In the present case, the ability of our low molecular weight aEPR to flow on the surface may be facilitated by the observation that it sticks out of the surface prior to application of the solvent vapor.

6.5 Conclusion

The surface compositions of melt-quenched blends of isotactic polypropylene (iPP) with aspecific poly(ethylene-co-propylene) rubber (aEPR) were studied by atomic force microscopy (AFM), optical microscopy, and x-ray photoelectron spectroscopy (XPS). Blend surfaces can be prepared that are enriched in iPP, enriched in aEPR, or that contain a phase separated mix of the two components. For blends melted in open air, iPP preferentially segregates to the air/polymer interface. At confined interfaces, surface segregation of iPP is suppressed. Blends melt-pressed between hydrophilic and between hydrophobic substrates have both iPP and aEPR phases present at the surface, which phase separate with increasing lateral domain size as the melt time increases. After melt-pressing, the more soluble aEPR component can be enriched at the interface by exposing the blend to n-hexane solvent vapor.

References

[1] Jones R.A.L.; Norton L.J.; Kramer E.J.; Bates F.S.; Wiltzius P. *Phys. Rev. Lett.,* **1991**, *66,* 1326.

[2] Scheffold, F.; Budkowski A.; Steiner U.; Eiser E.; Klein J.; Fetters L.J. *J. Chem. Phys.* **1996**, *104,* 8795.

[3] Klein, J.; Kerle, T.; Zink, F.; Eiser, E. *Macromolecules* **2000**, *33,* 1298.

[4] Zhao, X.; Zhao, W.; Sokolov, J.; Rafailovich, M. H.; Schwarz, S. A.; Wilkens, B. J.; Jones, R. A. L.; Kramer, E. J. *Macromolecules* **1991**, *24*, 5991.

[5] Opdahl, A; Phillips, R.A.; Somorjai, G.A. *Macromolecules* **2002**, *35*, 4387.

[6] Wu, D.T.; Fredrickson, G.H. *Macromolecules* **1996**, *29*, 7919.

[7] Donley, J.P.; Wu, D.T.; Fredrickson, G.H. *Macromolecules*, **1997** *30*, 2167.

[8] Kokkinos, I.G.; Kosmas, M.K. *Macromolecules* **1997**, *30*, 577.

[9] Kumar S.K.; Yethiraj A; Schweizer K.S.; Leermakers F., J. Chem. Phys., **1995**, *103*, 10332.

[10] Phillips, R.A.; Wolkwoicz, M.D., in Polypropylene Handbook, E.P.Moore Jr., ed., Hanser, Munich, 1996.

[11] Clemens, R.J.; Batts, G.N.; Lawniczak, J.E.; Middleton, K.P.; Sass, C. *Prog.Organic Coatings*, **1994**, *24*, 43.

[12] Garbassi, F.; Occhiello, E.; Polato, F., *J. Mat. Sci.* **1987**, *22*, 207.

[13] Lawniczak, J.; Sass, C.; Stoffer, J.O.; Dechent, W.L., *Polym. Mater. Sci. Eng.* **1993**, *68*, 28.

[14] Krausch G., *Mat. Sci. Eng. Rev.*, **1995**, 14, 1.

[15] Wang, H.; R. J. Composto, *Macromolecules*, **2002**, *35*, 2799.

[16] S. Walheim; M. Böltau; J. Mlynek; G. Krausch; U. Steiner, *Macromolecules*, **1997**, *30*, 4995.

[17] Resconi, L.; Jones, R.L.; Rheingold, A.L.; Yap, G.P. *Organometallics* **1996**, *15*, 998.

[18] Based on estimates of the Flory-Huggins χ-parameter for iPP/aPP blends (Phillips, R. A., *J. Poly. Sci. B - Poly. Phys.*, **2000**, *38*, 1947), we infer that χ for the iPP/aEPR7

blend must be greater than the value published in reference 5 for the *a*PP/*a*EPR7 blend. This conclusion is supported by the fact that for the molecular weights chosen here (same as those in ref. 5), a one-phase blend would be predicted if the opposite conclusion were true. Since this is not observed, we conclude that the phases in the bulk must be closer to the pure component compositions than those previously published for the *a*PP/*a*EPR7 blend.

[19] Glass slides were treated with an octadecyltriethyloxysilanol solution in order to create hydrophobic surfaces using the method outlined in Xiao, X.D.; Liu, G.; Charych D.H.; Salmeron, M. *Langmuir*, **1995**, *11*, 1600.

[20] Roberts, R.F.; Allara, D.L., Pryde, C.A., Buchanan, D.N.E.; Hobbins, N.D. *Surf. Interface. Anal.* **1980**, *2*, 5.

[21] Briggs, D. Surface Analysis of Polymers by XPS and Static SIMS, Cambridge University Press, **1998**, Chapter 2.2, pages 27-46.

[22] Tomasetti, E; Legras, R; Nysten, B. *Nanotechnology* **1998**, *9*, 305.

[23] Tomasetti, E; Nysten, B; Rouxhet, PG; Poleunis, C; Bertrand, P; Legras, R. *Surface and Interface Analysis*, **1999**, 27, 735.

[24] Galuska, A.A.; Halverson, D.E. *Surface and Interface Analysis* **1998**, *26*, 425.

[25] Mirabella, F.M.; Dioh, N.; Zimba, C.G. *Polym.Eng.Sci.*, **2000**, *40*, 9.

Chapter 7

Stretched Polymer Surfaces: AFM Measurement of the Surface Deformation and Surface Elastic Properties of Stretched Polyethylene

7.1 Introduction

Many polymers are highly extensible and behave elastically. Polyethylene exhibits an unusually wide range of mechanical behaviors when it is extended - due to its complicated microstructure.[1-4] Polyethylene contains an amorphous fraction, which is rubbery at room temperature (Tg ~220 K). Depending on length and branching ratio, a large fraction of polyethylene may form crystalline lamella at room temperature (Tm ~390 K).[2] Chain architecture influences the microstructure of polyethylene, as do the melt processing conditions.[4] Both chain architecture and processing conditions are responsible for the wide range of common physical forms of polyethylene: from waxy to rubbery to hard plastic. The grades of polyethylene studied in the experiments presented here are high and low density polyethylene, HDPE and LDPE, which differ in their crystalline

content and exhibit bulk mechanical behavior intermediate to the rubbery and plastic states.[1]

The bulk morphological changes that occur when HDPE and LDPE are stretched have been characterized at many structural levels. At a molecular level, vibrational spectroscopy has been used to characterize the changes in bulk orientation of both crystalline and amorphous chain segments.[6,7,8] In general, Raman spectroscopy and polarized infrared vibrational spectroscopy show that as a polymer is stretched, chain backbones align in the direction of that stretch. For polyethylene, Pezolet reported that at draw ratios of 7 the amorphous chains show stronger alignment in the strain direction than the crystalline chains – the flexible amorphous domains are more easily deformed thatn the crystalline component.[6] At higher draw ratios, the original crystalline lamellae begin to break down, and the crystalline chains also orient in the stress direction.

For HDPE, up to the yield point, x-ray scattering data has indicated that the predominate crystallographic deformation mechanisms involve the rotation of blocks of lamellae facilitated by the flexible amorphous regions.[2] Beyond the yield point, irreversible crystalline deformations begin to dominate with the principle deformation mechanisms being chain slip processes within the lamellae. Data from x-ray scattering has been directly correlated to images collected from electron microscopy techniques, including SEM and TEM.[2,5,9] In addition to electron microscopy, changes in microstructure are also observable by light scattering[1,3,4] and optical microscopy.[2] The most common microstructure for polyethylene cooled from the melt is the spherulite morphology, where lamellae radiate from a central core.[2] Mandelkern has developed a phase diagram of polyethylene microstructure as a function of chain length and

crystallization conditions showing that, while spherulites are common for HDPE, smaller axialitic structures (precursors to spherulites) are the dominant morphology at high crystallization temperatures.[4]

A qualitative observation for spherulitic morphologies is that as the spherulite deforms from tensile stretching, it is transformed into an ellipsoid.[2] At low elongation, where primarily the amorphous regions deform, this transformation is reversible. At elongation above the yield strain there is a reduction in the recovery as the crystallographic deformations observed by x-ray scattering begin to dominate. At high elongation, spherulites typically transform into a fiber-like morphology. Ward et al. have examined the continuity of the transformation from spherulite to fiber-like structure.[9]

While the bulk molecular structure and deformation of polyethylene have been characterized by these and other complementary techniques, there is very little information detailing the response of the polymer surface to stretching. This chapter explores the morphological changes and corresponding mechanical properties of stretched polyethylene from the perspective of the surface, by atomic force microscopy, AFM. AFM has previously been used to study polyethylene surfaces.[10-15] AFM has also been used to examine the effect of stretching on polymer surfaces, focusing being on changes in morphology. Hild et al. used AFM in conjunction with a small tensile device to quantify lamellar separation in hard elastic polypropylene (HEPP) as a function of elongation.[16] AFM has also been used to observe the orientation changes of the hard and soft components of a PTMO/PA copolymer as the polymer is stretched.[17]

In the experiments reported here, AFM allows direct visualization of the deformation processes at the polyethylene surface. In the same experiments, the local

mechanical properties of the surface layer are probed. Shown in Figure 7-1, the bulk and surface of the polymer are stretched in the x-direction while the surface mechanical properties are probed by applying an extremely local stress in the 'z' direction with the AFM tip - without disrupting the bulk. In this way we have used the AFM tip to probe the surface elasticity of polyethylene as it is stretched and correlated this with changes in the microscopic morphology of the surface.
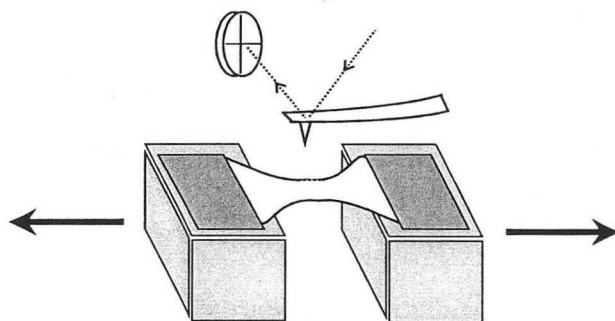
Figure 7-1 Schematic of the experimental setup.

7.2 Experimental procedures

Instrument. AFM measurements were made using a ParkAFM fitted with an M5 head, where cantilever bending is measured by reflecting a diode laser off of the backside of the cantilever and onto a position sensitive photodiode (Figure 7-1). Cantilevers with low force constants (0.5N/m, NT-MDT) were used to obtain topographic images of the surfaces under low contact loads. Higher force constant cantilevers (48 N/m, NT-MTD) were used to measure the stiffness and elastic modulus of the surface through force vs. distance interaction curves. The photodiode detector was calibrated to each cantilever by collecting force vs. distance curves taken on silicon and using the nominal value of the cantilever force constant given by the manufacturer. The AFM tip radius was estimated

by imaging a calibration grating with a smaller radius of curvature than the AFM tip, ~10nm (NT-MDT calibration grating TGT01).

Samples. Low and high density polyethylene were obtained in pellet form from Aldrich Chemical. Films (1mm thick) were prepared by melt pressing the pellets at 130C under glass. After heating, the films were slowly cooled to room temperature. Crystallinity of the pressed samples was measured by Differential Scanning Calorimetry (DSC) assuming an enthalpy of fusion of 295.8 J/g for a perfect PE crystal.[14] Bulk measured properties are given in Table 7-1. Bulk elastic modulus was determined from the initial slope of a tensile stress vs. strain test (strain rate=1cm/minute). Yield stress was estimated from the maximum stress in the stress vs. strain curve. Yield strain is the corresponding value of the strain.

Table 7-1: Material properties of LDPE and HDPE

	LDPE	HDPE
Crystallinity	25%	60%
Elastic Modulus	0.2 GPa	1 GPa
Yield Strain	10%	6%
Tensile Strength at Yield	10 MPa	25 MPa

XPS was used to ensure that the surfaces were not oxidized or otherwise contaminated during sample preparation. Bulk microstructure was characterized by light scattering and optical microscopy. A light scattering setup comprised of a 5mW HeNe laser and crossed polarizers was used to collect scattering patterns of the melt pressed samples using the Hv polarization combination. A Zeiss optical microscope was used to characterize the bulk microstructure of thinner samples (500μm) in transmission geometry.

133

Dumbbell shaped test pieces with a gauge length of 25 mm and width of 6 mm were cut from the films. A schematic of the AFM experimental setup is shown in Figure 7-1. Test pieces were elongated at room temperature on a homemade tensile tester at a rate of ~1 cm/min up to a specific strain. After stretching, the AFM head was positioned near the center of the neck region.
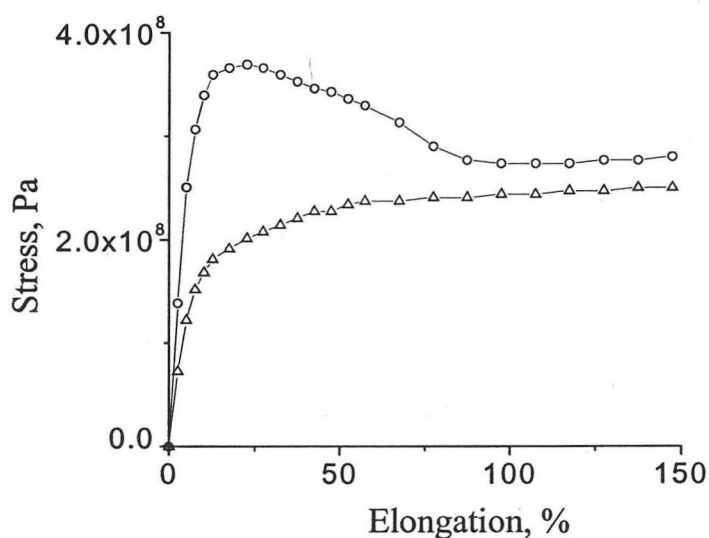
Figure 7-2 Tensile stress vs. strain curves for LDPE($\triangle$) and HDPE($\diamondsuit$).

Relaxation processes, lasting for several minutes, begin immediately after stretching and decrease the overall thickness of the sample. To account for these processes, after each stretching increment, the samples were allowed to relax to an equilibrium stress before AFM measurements were made. Equilibrium tensile stress vs. strain curves, where the sample was strained incrementally and was allowed to relax for 5 minutes before recording the stress, for HDPE and LDPE are shown in Figure 7-2. Under these stretching conditions, the stress vs. strain curve for HDPE can roughly be divided into three regions: (1) an initial elastic region where the stress increases with the strain up to the yield strain, (2) a region of tensile strain softening occurring after the yield strain,

134

and finally (3) a region where the polymer is drawn into a thin neck and the stress remains fairly constant as the strain is increased. LDPE behaves similarly, however, the yield point is not well defined and there is no strain-softening region. This difference in bulk behavior of the two materials is consistent with the differences in crystallinity as described by Popli and Mandelkern.[1]

Texture. AFM topography images were flattened (2nd order) using a Park software routine. The RMS roughness (defined by equation 1a where $z_{i,j}$ is the height of the i x j pixel in an image, z is the average height of the pixels in an image, and n is the number of pixels in the image) was calculated on 100 μm^2 areas using the Park software.

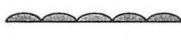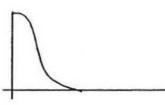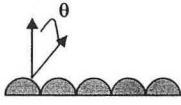$$\text{RMS roughness} = \sum_{i,j} \frac{\left(z_{i,j} - \bar{z}\right)^2}{n} \qquad (7\text{-}1a)$$
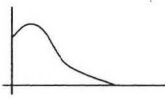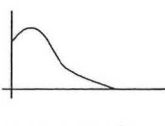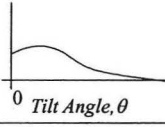
The surface gradient, defined as the angle between the local surface normal and the macroscopic surface normal, was used to describe anisotropy in roughness. Images were imported into a mathematical software routine and gradient was decomposed using Equations 7-1b and 7-1c for a component parallel with the strain (along the columns of an image) and a component perpendicular to the strain (along the rows of an image).

$$\theta_{parallel} = \arctan\left(\frac{z_{i,j+1} - z_{i,j}}{L}\right) \qquad (7\text{-}1b)$$

$$\theta_{perpindicular} = \arctan\left(\frac{z_{i+1,j} - z_{i,j}}{L}\right) \qquad (7\text{-}1c)$$

Histograms of the parallel and perpendicular components of the tilt angle were compiled from all of the pixels in an image. Selected surface textures and the RMS roughness values and tilt angle histograms associated with them are shown in Figure 7-3.

135

RMS roughness defines how deep features are on a surface. In conjunction with the tilt angle histogram, the periodicity of regular repeating features can be estimated.

Surface texture	Tilt Angle histogram	RMS roughness
		small
		small
		large
		large

Figure 7-3 Surface textures and the corresponding tilt angle histograms and RMS roughness values.

Stiffness and Elastic Modulus. Stiffness (S) was measured directly from the slope of the AFM force vs. distance interaction curve. Shown in Figure 7-4, the force vs. distance curve measures the dependence of the cantilever deflection, y, on the motion of the driving z-piezo, z, as the tip is pressed directly against the surface. Curves were collected at loading/unloading rates of 100 nm/s with a maximum load of 400nN for LDPE and 1000nN for HDPE corresponding to penetration depths of less than 40nm. The stiffness is defined in this paper as the slope of that curve, dy/dz.[20] A surface which does not deform when the cantilever presses against it yields a stiffness value equal to the

cantilever force constant (48N/m in this case) while a totally compliant surface would yield a stiffness value of zero (no cantilever bending).
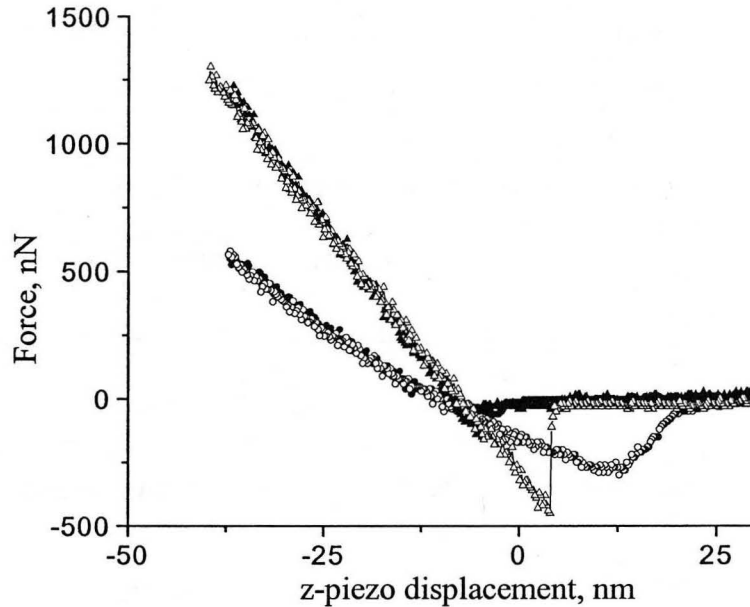
Figure 7-4 AFM force vs. distance curves for HDPE (▲ loading , △unloading) and LDPE (● loading, O unloading).

In indentation experiments, the stiffness is commonly taken as the initial slope of the retracting curve, where all of the deformation is assumed to be elastic and the nanoindentor tip movement is purely in the z-direction.[20] If there is significant plastic deformation of the sample, it manifests itself as hysteresis between the tip approach and tip retract curves. Nanoindentation using the AFM is problematic, as AFM tip shapes are generally less defined than diamond tips used in nanoindentors. Thus we have chosen to present the slope of the *approach* curve as our stiffness measurement. As a check though,

the slopes of the approach and retract curves are generally identical for all of the measurements presented here, indicating that are indentations are primarily measuring an elastic response of the surface.

To calculate the elastic modulus, the relationship that the sum of the two deformation components (deformation of the cantilever and of the polymer) must equal the total displacement of the driving z-piezo has been used.[18,19]

$$z_{(\text{drive})} = (load/k)_{(\text{cantilever})} + d_{(\text{material})} \qquad (7\text{-}2)$$

Several models exist that describe the penetration, d, of an indentor into a surface (Sneddon, Hetrz, JKR, etc.).[21] For AFM experiments, since properties such as the tip shape function and radius of curvature are estimates and because polymeric materials tend to be compliant leading to relatively deep indentations, it is not immediately obvious which model of contact is appropriate. Tsukruk et al. have performed a detailed comparison of the elastic moduli calculated from the loading portion of force vs. distance curves using the Hertz model, the JKR model, and Sneddon's model for several types of polymers.[18,19] They found that in the loading regime, where all of the deformation is elastic, all three models give reasonable values of elastic modulus. The highest precision was obtained with the JKR model, which accounts for interfacial energy between the tip and indentor. As we are primarily interested in presenting relative values and not the absolute values of elastic modulus, we have used the simpler Hertz contact for describing the depth of penetration of the tip into the surface. This approximation neglects adhesive interaction between the probe and sample as well as the viscous response of the polymer and as a result underestimates the real contact area and overestimates the true value of elastic modulus.[18]

$$d_{(pen.)} = 0.82(load)^{2/3} R^{-1/3} \left(\frac{E}{1-v^2} \right)^{-2/3}$$

(7-3)

In Equation 7-3, R is the tip radius of curvature, v is the Poisson ratio for the polymer, and E is the elastic modulus of the polymer. Substituting Equation 7-3 into Equation 7-2 the slope of the approach curve, *d(load)/dz* (the stiffness), can be solved.[22] An important note is that *both* the cantilever and the polymer surface must deform. Each cantilever is only sensitive to a small range of elastic moduli which typically spans 2-3 orders of magnitude on a Pascal scale.[18,19] After each experiment the tip was scanned over a calibration grating to check that the tip had not been blunted and additional reference force curves were taken on silicon substrates to ensure that the cantilever properties remained constant throughout the experiment. In order to approach a macroscopic average of the surface stiffness and elastic modulus, over 100 force vs. distance curves were collected at unique points near the center of the polymer test piece for each value of tensile strain.

7.3 Results and discussion

Bulk morphology Light scattering patterns were collected on undeformed HDPE and LDPE in order to characterize the bulk structure. Under the heating and cooling conditions we have used, the most common morphologies expected for bulk HDPE are spherulites and axialites (rodlike structures which may have length equal to width)[4,9] For LDPE the most common morphologies are spherulitic or indeterminate. Light scattering yielded cloverleaf scattering patterns, consistent with a spherulite morphology.[4] For LDPE, the scattering angle between the incident beam and the brightest spot on the scattered pattern, the average size of structures is estimated to be 1–2 microns.[23] For

139

HDPE, the scatter patterns are similar in shape to the LDPE patterns, however the scatter angle is about twice the magnitude as that measured on LDPE (the limit of our light scattering setup) indicating that the bulk spherulites are roughly $0.5 - 1$ micron diameter. Optical microscopy shows space filling granular structures in both polymers that are near the edge of the microscope resolution (~1 micron). Both samples show evidence of birefringence in polarized light indicating crystalline structures.

Surface Texture AFM topography images taken in contact imaging mode with *low* applied pressure are shown in Figures 7-5 and 7-6. They show that the surfaces of LDPE and HDPE are made up of a random distribution of circularly symmetric nodular structures that are similar in size to the bulk spherulites. Films prepared without a pressing substrate yield structures similar in size to those prepared by pressing with glass, showing that the nodular features are not simply artifacts of the pressing substrate. The glass pressed features are, however, flatter than the open air crystallized features. The size of the surface nodules varies with the size of the bulk spherulites - AFM images show that the LDPE nodules are approximately twice as large as the HDPE structures and are typically less defined. Very little fine structure is apparent at the surface of these nodular structures, making an assignment of the nodular morphology speculative. However, since the size is similar to the bulk spherulitic structures and varies with the size of bulk structures, it is likely that the surface nodules are closely related to the bulk spherulites.

The surface textures of both HDPE and LDPE at low, intermediate, and high elongation are shown in Figures 7-5 and 7-6. Qualitatively, the surfaces become rougher as a result of deformation of the nodular structures. The nodular structures at the surface lengthen in the direction of the stretch and contract perpendicular to the stretch until the

140

polymer is stretched up to the neck propagation region. Stretching into the neck propagation region, the nodular structures break down and are transformed irreversibly into microfibers (Figure 7-7). The RMS roughness, tilt angle histograms, and topographic images quantify these texture changes.

During the stretching process, the difference in height between the center and edge of a nodular structure increases. As each nodule contracts laterally, the material in the center of the nodule is pushed upward relative to the edge of the nodules. The RMS roughness factor quantifies this effect. Figure 7-8a shows a direct dependence between RMS roughness and elongation for LDPE and for HDPE. At elongation less than 10% (within the initial elastic region) the surface roughness increases when the polymer is elongated and decreases when the strain is decreased. On the first stretching cycle, the dependence is linear and is completely reversible within our experimental error for both HDPE and LDPE.
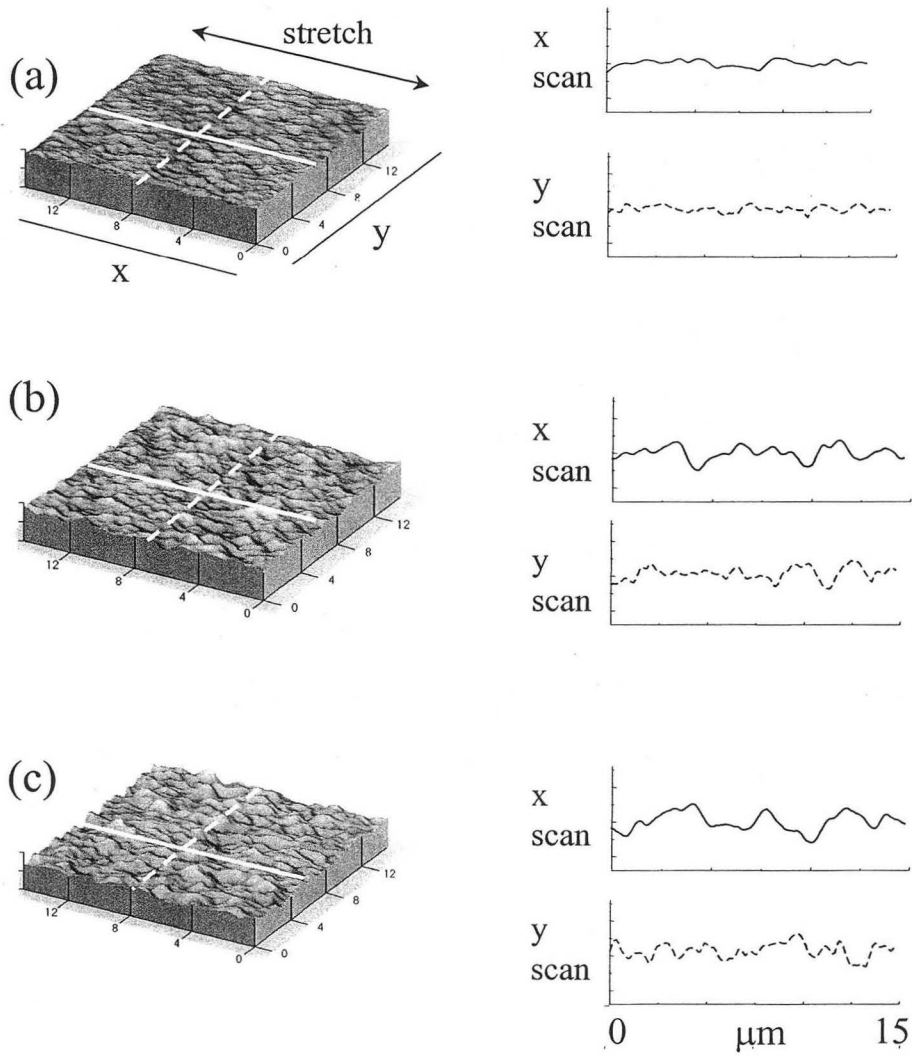
Figure 7-5: 15x15μm AFM images of stretched HDPE (a) 4% elongation (b) 15% elongation (c) 30% elongation (150nm z-scale).
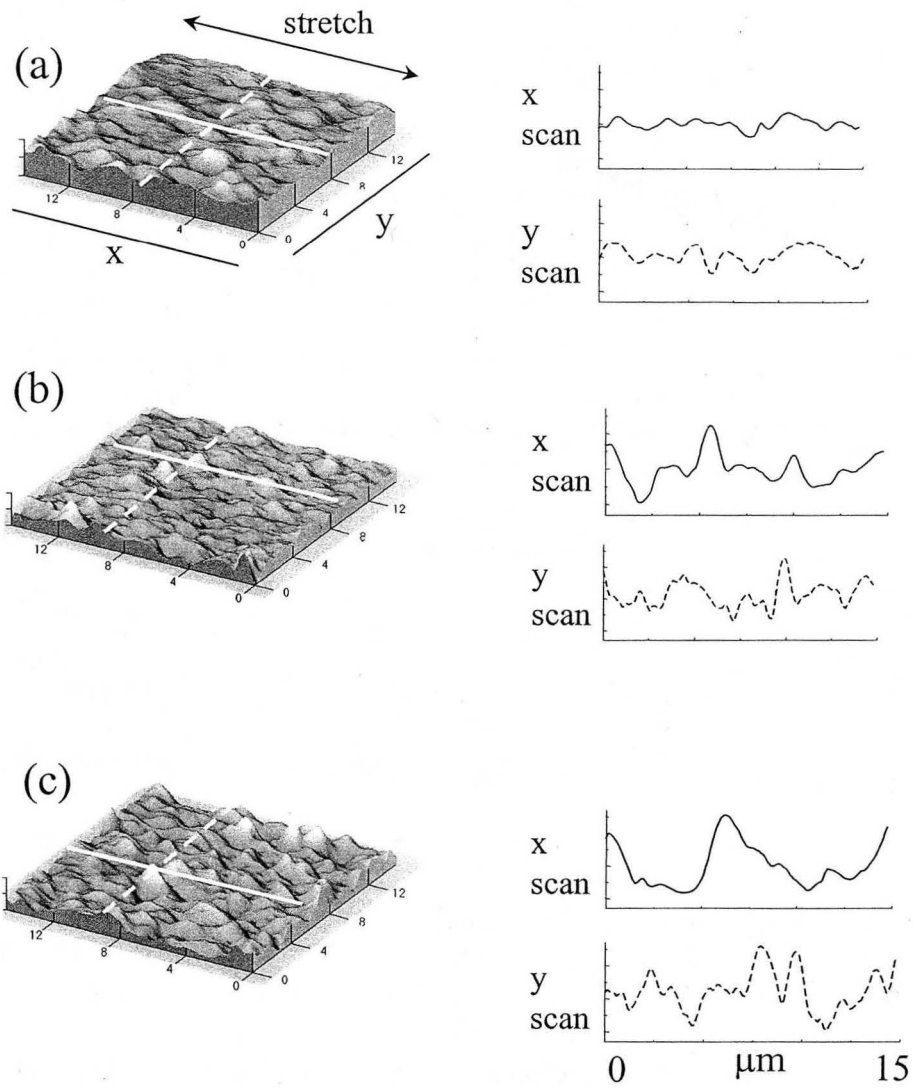
Figure 7-6: 15x15μm AFM images of stretched LDPE (a) 7.5% elongation (b) 17.5% elongation (c) 27.5% elongation (150nm scale).
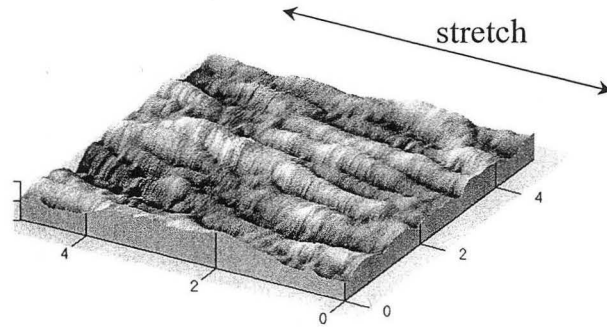
Figure 7-7 5x5μm AFM Image of HDPE microfibers (80% elongation).

To check for fatigue and other processes which may generate defects in the surface structure and increase the roughness, LDPE was cyclically stretched from 5 to 10% elongation and then released to 5% elongation 100 times. The roughness as a function of stretching cycle is shown in Figure 7-8b. The surface behaved elastically throughout the process – i.e. the roughness recovered to its original value on each stretching cycle. The final surface roughness value at 10% elongation after 100 stretching cycles is identical to the initial surface roughness value at 10% elongation. Irreversible defect and void generation are not the primary cause of the roughening effect – elastic microstructure deformation is the primary contributor at low strains. The high reversibility is consistent with the bulk behavior of polyethylene at low elongation where bulk superstructures show immediate recovery after the removal of stress. The surface nodules behave similarly to bulk spherulites, which respond elastically to low tensile stresses.[2]
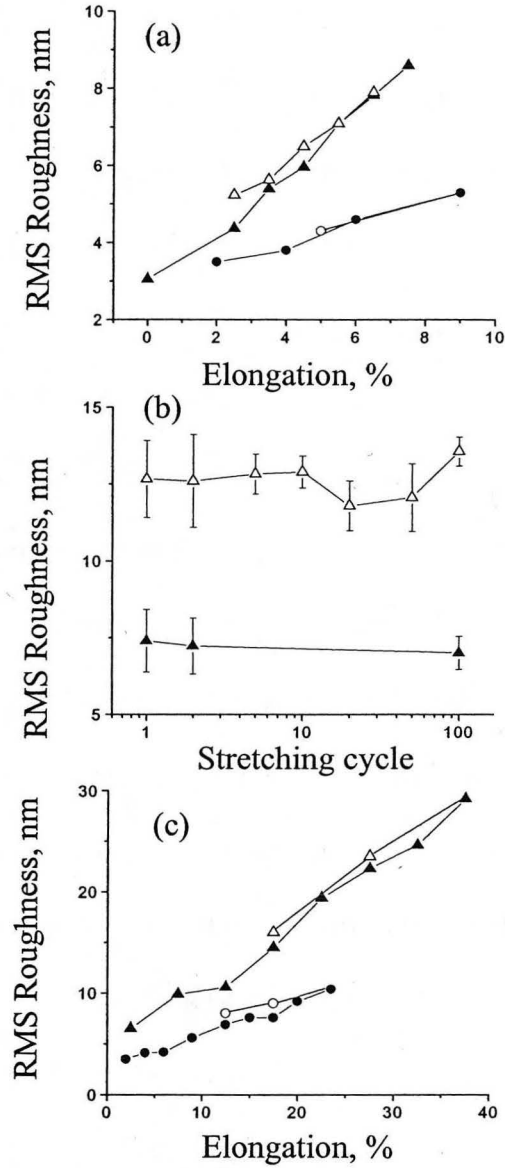
Figure 7-8 (a) RMS roughness vs. elongation for LDPE(▲ loading , △ unloading) and HDPE(● loading, ○ unloading) at low *elastic* strains. (b) RMS roughness vs. stretching cycle for LDPE cyclically strained from 5% (▲) to 10% (△) elongation. (c) RMS roughness vs. elongation for LDPE(▲loading , △ unloading) and HDPE(● loading, ○ unloading) at *intermediate* strains.

The AFM images in Figures 7-5 and 7-6 show that the roughness is anisotropic. The nodular structures contract perpendicular to the stretching direction and develop higher curvature. Histograms of the tilt angles parallel and perpendicular to the stretching direction are shown in Figures 7-9a and 7-9b. Prior to stretching, histograms of the surface gradient parallel to and perpendicular to the stretching direction are nearly identical, indicating an isotropic rough surface. For the stretched case, anisotropy develops between the parallel and perpendicular components. Relative to the tilt angles parallel to the direction of stress, the distribution of the perpendicular tilt angles is much wider. This shows that as the nodular structures compress perpendicular to the strain, the nodule radius of curvature decreases more quickly than the nodule radius of curvature in the direction of the strain does– consistent with a transformation to an elliptical structure.

The relationship between roughness and elongation continues up to neck propagation for both polymers, around 70% for HDPE and 50% for LDPE. Figure 7-8c compares the roughening effect on the HDPE and LDPE surfaces. The slope of the RMS roughness vs. elongation curve is two times smaller for HDPE than for LDPE. That is, for a given elongation, HDPE roughens less than LDPE. The change in height between the center and edge of a nodule is more pronounced on large structures than on small structures. Since the structures on the LDPE surface are generally larger than the structures on the HDPE surface, LDPE should be expected to roughen more than HDPE – leading to a steeper slope on the roughness vs. elongation plot.
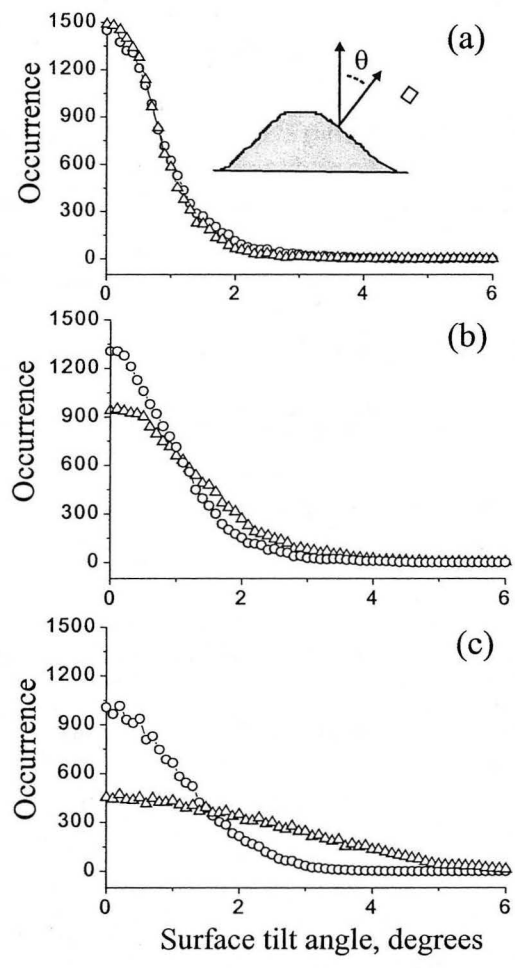
Figure 7-9 Tilt angle histograms for HDPE (a) no elongation (b) 37% elongation (c) 80% elongation (O is tilt parallel to strain direction and △ is tilt perpendicular to strain direction).

The roughness is partially reversible on the first stretching cycle for both polymers at intermediate strains (between yield strain and the neck propagation region). The time scale for the roughness recovery, however, is much longer than the initial elastic region where the surface roughness was immediately reversibly. At high elongation, it takes

147

several minutes for the polymer to recover (decrease in length) when the stress is removed. The recovery on repeated stretching cycles from 15 to 30% elongation is also slow, but generally reversible, after the first stretching cycle.

When HDPE and LDPE are strained into the neck propagation region, a stable neck is created and the nodular structures are irreversibly transformed into fibers. The fibers are ~500nm in width for HDPE and several microns long at the surface. The fibers are similar to fibers reported by Maganov[11] and by Vansco[13] by AFM. The roughness anisotropy, shown by the difference in tilt angle histograms in Figure 7-9c, is very large as should be expected for a fiber morphology.

Initially, the surface consists of nodular structures flattened from the pressing substrate. As the test piece is stretched, each individual domain elongates in the direction of the stress and contracts perpendicular to the stress. The contraction of an initially flat domain leads to the development of curvature and roughness (an increase in height between the center and edge of a nodule).

Surface stiffness As the surface structure changes, the mechanical properties of the polymer surface also change. In particular, the stiffness and elastic modulus of the surface change are presented in Figures 7-10a and 7-10b as a function of polymer elongation. The stiffness (S) represents the simple measurement of the slope of the force vs. distance interaction curve while the elastic modulus represents a projection of that stiffness value onto a calculated contact area using the Hertz model.
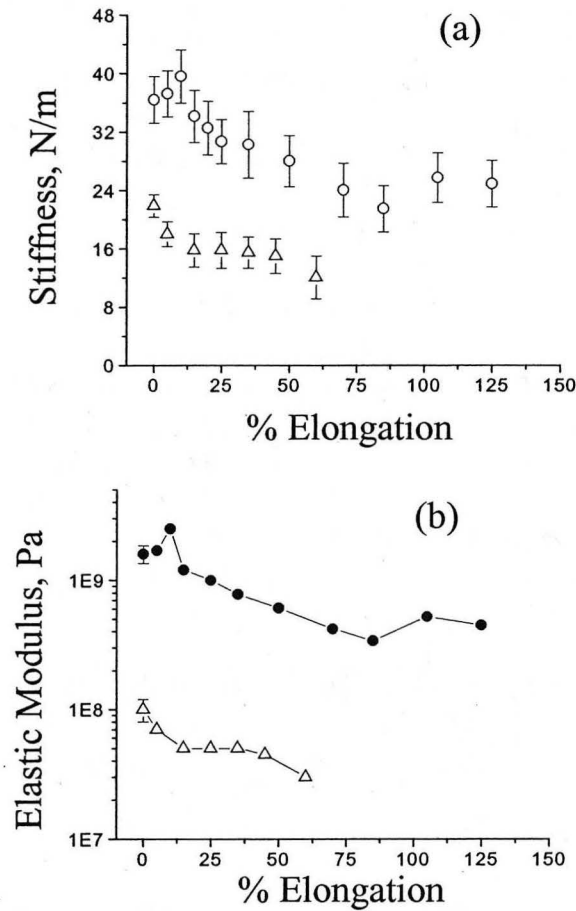
Figure 7-10 (a) Surface stiffness vs. elongation for LDPE(O) and HDPE(△). (b) Surface elastic modulus vs. elongation for LDPE(●) and HDPE(▲).

Force vs. distance interaction curves collected on unstressed HDPE and LDPE are shown in Figure 7-3. From these curves, the initial surface elastic modulus of HDPE is estimated to be ~1.6GPa, the same magnitude as the bulk elastic modulus determined from the macroscopic tensile stress-strain curve. The initial modulus of LDPE using the same cantilever is estimated to be 0.1 GPa, again similar to the bulk value. At ~30-40% elongation, the surface stiffness of both materials has decreased significantly from the initial value. Figure 7-10 shows that, in general, the surface stiffness and elastic modulus

149

for both materials decreases on stretching. There is, however, an initial increase of the surface elastic modulus for HDPE in the region 0-10% elongation (the elastic portion of the tensile stress vs. strain curve). The maximum value of the elastic modulus is ~3 GPa at 10% elongation (near the macroscopic tensile yield point). Beyond the tensile yield point, the elastic modulus decreases with the stretch.

For HDPE, the decrease continues up to 120% elongation, where the test piece begins to form a neck. In the neck propagation, region the surface modulus stabilizes at around one third of its original value, 0.5 GPa. This result is also consistent with the macroscopic behavior of the polymer. In this region, there are significant amorphous and crystalline components in the deformation process.[2] The amorphous regions are preferentially orientated and as the lamellae are deformed they also begin to assume a preferred orientation. In fiber technology, orientation effects typically enhance the elastic modulus in the draw direction and reduce the modulus in the transverse direction. While the polymer has certainly not been drawn into a fiber at this point, it is likely that the decrease in modulus is related to preferential chain orientation. These orientation effects may also explain the decrease in modulus of LDPE.

7.4 Conclusion

These results show that when polyethylene is stretched, the surface structure and surface mechanical properties are affected. Many of these surface measurements are consistent in the context of the well-studied bulk properties of stretched polyethylene. Qualitatively, the HDPE and LDPE surfaces behave similarly. At low strains, the bulk deformation of both grades of polyethylene is reversible. The surface nodules on both grades also exhibit immediate reversibility when stretched and released. This is reflected

150

in the measurements of RMS roughness at low strains. Nodular domains expand in the direction of the stretch as strain is increased and contract when strain is decreased.

Stretching beyond the tensile yield strain, the nodules continue to elongate in the direction of the stress and compress perpendicular to the stress. However, the roughening effect, and therefore the deformation of the microstructure, is no longer immediately reversible. There is a decrease in the surface stiffness and elastic modulus for HDPE and LDPE consistent with the development of a fiber-like morphology. Both the slow reversibility of the roughening and the decrease in elastic modulus are associated with crystalline deformation of the polymer. Finally, for both HDPE and LDPE, the nodular microstructure breaks down and the morphology becomes fiber-like.

These results have a general applicability to the friction and wear properties of polymers in real situations. It has been previously shown that contact pressure and contact area are important parameters in determining the dominant friction mechanisms of polymers.[14,15] We have shown here that external stress also changes the surface texture and surface mechanical properties of a polymer. Changes in mechanical properties induced through external stress will directly affect the contact pressure and contact area and may alter the predominant friction and wear mechanisms operating at the surface. Additionally, the roughness results show that for external stresses can dramatically change the surface texture. In some applications, this may change the nature of the contact area between the polymer surface and the pressing substrate and directly affect the wear of the polymer. Since the roughening effect in these cases appears to be related to the microstructure, particularly the size of individual features, this effect should be predictive.

References

[1] Popli, R.; Mandelkern, L. *J Polym Sci Polym Phys Ed*, **1987**, *25*, 441.

[2] Brooks, N.W.J.; Unwin, A.P.; Duckett, R.A.; Ward, I.M. *J Macromol Sci Phys*, **1995**, *B34(1&2)*, 29.

[3] Lin, L.; Argon, A.S. *J Mat Sci*, **1994**, *29*, 294.

[4] Maxfield, J.; Mandelkern, L. *Macromolecules*, **1997**, *10*, 1141.

[5] Bassett, D.C. *Principles of Polymer Morphology*, Chapter 9, Cambridge University Press, **1981**.

[6] Pigeon, M.; Prud'homme, R.; Pezolet, M. *Macromolecules*, **1991**, *24*, 5687.

[7] Lafrance, C.P.; Chabot, P.; Pigeon, M.; Prud'homme, R.; Pezolet, M. *Polymer*, **1993**, *34*, 5029.

[8] Hendra, P.J.; Maddams, W.F. *Polymer Spectroscopy*, Chapter 7, ed. By Allan H. Fawcett, John Wiley and Sons Ltd., **1996**.

[9] Amornsakchai, T.; Olley, R.H.; Bassett, D.C. Al-Hussein, M.O.M.; Unwin, A.P; Ward, I.M. *Polymer*, **2000**, *41*, 8291.

[10] Viswanathan, R.; Marr, D.W.M *Langmuir*, **1996**, *12*, 1087.

[11] Wawkushewski, A.; Cantow, H.J.; Magonov, S.N. *Advanced Materials*, **1994**, *6*, 476.

[12] Magonov, S.N.; Reneker, D.H. *Annual Review of Materials Science*, **1997**, *27*, 175.

[13] Schoenherr, H.; Vansco, G.J.; Argon, A.S. *Polymer* 1995, *36*, **1995**.

[14] Gracias, D.H.; Somorjai, G.A. *Macromolecules*, 31, **1998**, 1269.

[15] Niederberger, S.; Gracias, D.H.; Komvopoulos, K.; Somorjai, G.A. *J Applied Phys*, **2000**, *87*, 3143.

[16] Hild, S.; Gutmannsbauer, W.; Luth, R.; Fuhrmann, J.; Guntherodt, H.J. *J Polym Sci Polym Phys Ed*, **1996**, *34*, 1953.

[17] McLean, R.S.; Sauer, B.B. *J Polym Sci Polym Phys Ed*, **1999**, *37*, 859.

[18] Chizhik, S.A.; Huang, Z.; Gorbunov, V.V.; Myshkin, N.K.; Tsukruk, V.V. *Langmuir*, **1998**, *14*, 2606.

[19] S.A. Chizhik, Z. Huang, V.V. Gorbunov, N.K. Myshkin and V.V. Tsukruk, *Langmuir*, **1998**, *14*, 2606.

[20] G.M. Pharr and W.C. Oliver, *MRS Bulletin*, **1992**, *17*, 28.

[21] K.L. Johnson, *Contact Mechanics*, Cambridge University Press, **1989**.

[22] The slope of the approach curve was determined using mathematical software to solve Eq. 3 for y and then dy/dz.

[23] R.S. Stein and M.B. Rhodes, *J. Applied Physics*, **1960**, *31*, 1873.

[24] Amitay-Sadovsky, E.; Ward; B.; Somorjai, G.A.; Komvopoulos, K. *J. Appl. Phys.*, **2001**, *91*, 375.

Chapter 8

Surface deformation of a triblock poly(styrene-butadiene-styrene) copolymer as it is stretched

8.1 Introduction

In this chapter, the surface morphology of a poly(styrene-butadiene-styrene) triblock has been characterized it is elongated. As noted in the previous chapter, the elastic properties exhibited by polymer systems have been extensively studied from a bulk material perspective. Elastic polymer systems are usually crosslinked networks or are comprised of interconnected rigid and flexible phases. The flexible phase is a polymer that is rubbery at room temperature and that absorbs most of the strain under low deformations. Shape memory is retained though interconnections with the rigid phase, which is either crystalline, as in polyethylene, or a polymer that is glassy at room temperature.

From a surface perspective, stretching increases the overall surface area of a material. In a multi-component polymer system, one of the components will usually be

enriched at the surface (see Chapters 5 and 6), due to differences in the surface energies of the individual components. Thus for blends, copolymers, and filled polymers, a change in surface area may also be expected to lead to a change in surface composition as the polymer is elongated. This has been demonstrated, for example, in segmented polyurethanes, comprised of short rubbery and glassy chain segments. Segmented polyurethanes are often used in biomedical applications and can exhibit elastic behavior up to several hundred percent elongation. Investigations have shown that the surface is predominantly covered by the rubbery phase, which has lower surface energy than the glassy phase.[1,2] When the polyurethane is elongated, the rubbery segments expand, exposing the underlying high surface energy glassy segments.

Atomic force microscopy (AFM) can be used to study deformation processes at surfaces, and besides the above-mentioned polyurethanes, the surfaces of thermoplastic elastomers,[3,4] elastic polypropylene,[5] polyethylene,[6] styrene-rich SBS copolymers,[7,8] and blends[9] have been studied as a function of elongation. This investigation is focused on a polystyrene(butadiene)styrene ABA triblock copolymer (SBS), where polybutadiene is the majority component, and the block lengths are long compared to segmented polyurethane. AFM friction and topography images show that when the copolymer is stretched, the deformation is highly localized. Deformation zones develop at the surface, perpendicular to the stretching direction. The deformed regions, covering a larger percentage of the total surface area as the polymer is elongated, are expected to be rich in polybutadiene.

8.2 Experimental

Polymer films Polystyrene(butadiene)styrene ABA triblock copolymer was purchased from Scientific Polymer (styrene content 30%, Mw 140,000) and dissolved in toluene (Aldrich, 99.5% spec grade). Films were prepared by slow solvent evaporation into Teflon dishes. After the solvent was evaporated, the films were annealed at 110°C for 24 hours and cooled at ~1°C/min back to room temperature. "Dogbone" shaped specimens, suitable for stretching, were cut from the films and had a neck length of 2.54 cm, width of 0.63 cm, and were ~0.15 cm thick. Only the surface prepared in contact with air was analyzed (not the polymer/Teflon interface).

SBS copolymers have been extensively studied. These materials form bulk morphologies that are dependent on the relative lengths of the styrene and butadiene segments. For the SBS block copolymer used in this study (butadiene rich), the bulk is expected to have a phase-separated morphology, where the polystyrene blocks are organized as spheres (20-50nm) embedded in a polybutadiene matrix.[10] Our AFM images of the undeformed SBS generally showed featureless images on a 3x3μm image scale, possibly due to the low modulus of the polybutadiene matrix.

Atomic Force Microscopy (AFM) AFM measurements were made using a ParkAFM fitted with an M5 head, capable of scanning 100μmx100μm regions. Cantilevers with 0.1 N/m force constants (NT-MDT) were used to obtain topographic and lateral force images of the surfaces in contact scanning mode. Specimens were elongated at room temperature on a homemade tensile tester at a rate of ~1 cm/min up to a specific strain and held at that strain while the surface was imaged by AFM, as described in Chapter 7.

SFG vibrational spectroscopy Surface vibrational spectra were obtained using the experiemental setup described in Chapter 1, respectively, and the induced sum-frequency signal was measured in the reflected direction. The intensity of the sum-frequency signal is described by Eq. 8-1 and is proportional to the square of the second order non-linear susceptibility of the excited medium, $\chi^{(2)}$ (Eq.1).[11] Spectra were collected using the $s_{sum}s_{vis}p_{ir}$ polarization combination.

$$I(\omega_{sum}) \propto \left|\chi^{(2)}\right|^2 = \left|\chi_{NR} + \sum_q \frac{A_q}{\omega_{IR} - \omega_q + i\Gamma_q}\right|^2 \tag{8.1}$$

8.3 Results

SBS surface prior to elongation An SFG spectrum collected from the surface of an SBS film is shown in Figure 8-1a (ssp polarization combination). For comparative purposes, an SFG spectrum of a polystyrene film spin cast from toluene and then annealed at 110°C for 12 hours is shown in Figure 8-1b. This SFG spectrum of polystyrene has been previously described in Chapter 3 (and ref. 12) and is similar to those presented by Zhang[13], Gautam[14], Briggman[15], and Oh-e[16] where the dominant feature is the symmetric $\nu2$ stretch from the aromatic side group at ~3060cm^{-1}. At a basic level this SFG spectrum indicates that the phenyl side branches are preferentially oriented at the polymer surface.

The dominant feature in the SFG spectrum of the SBS copolymer is also the symmetric $\nu2$ aromatic stretch associated with the polystyrene component. The measured intensity of this vibrational mode is significantly weaker than that measured from the polystyrene film. SFG vibrational mode strengths are proportional to the order, orientation, and surface concentration of a surface species. Under the assumption that the

average orientation of the phenyl groups is similar for the SBS copolymer and the polystyrene homopolymer, then the SFG mode strengths are roughly proportional to concentration.[17] The fitted mode strength, A_q, for the $v2$ stretch from the SBS copolymer is less than half as large as the $v2$ mode strength from the polystyrene film. This result qualitatively indicates that prior to stretching, the surface of the SBS copolymer is likely a mixture of polystyrene and polybutadiene blocks – and that a percentage of the surface contains rigid polystyrene domains. Spectra collected from polybutadiene homopolymer films generate a very small amount of SFG signal in the CH_2 stretching region.
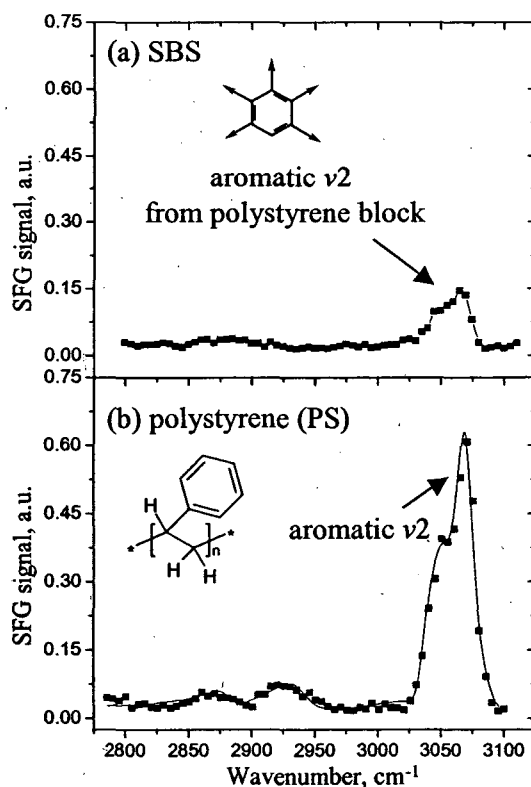

Figure 8-1: (a) SFG spectrum of SBS rubber prior to elongation and (b) SFG spectrum collected from the surface of a polystyrene film (*ssp* polarization combination).
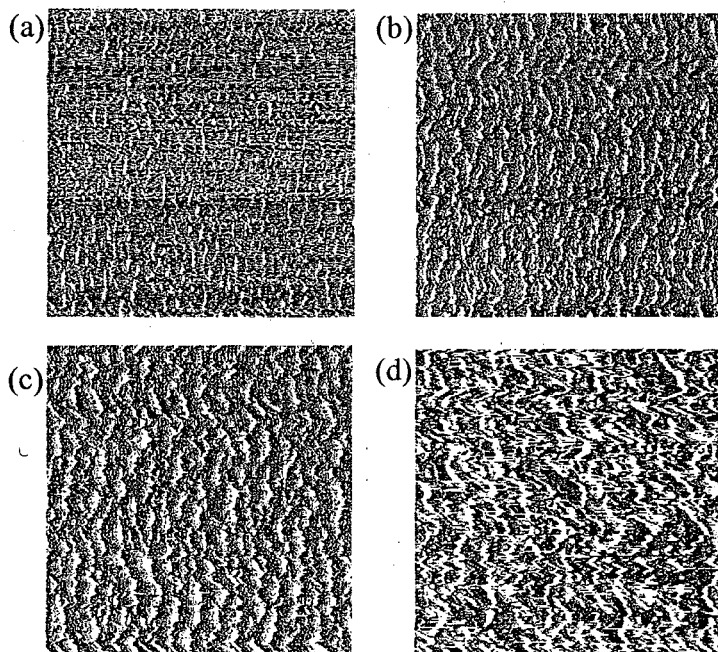
Figure 8-2: 30x30μm AFM lateral force (friction) images taken from the SBS surface (a) prior to elongation and at (a) 20% (b) 40% (c) 60% and (d) 100% elongation. Elongation is left/right.

AFM images of SBS rubber as is it elongated A series of 30x30μm AFM lateral force (friction) images of the SBS rubber surface is shown in Figure 8-2 and were collected at various stages of elongation between 20% and 100%. Prior to elongation, the image of the SBS surface appears homogeneous on a 30x30μm scale image. When the SBS is elongated by <10%, deformation zones initiate in the SBS surface. These deformation zones display high friction against the sliding of the AFM tip and appear as white regions in the lateral force images. The deformation zones are oriented transverse to the stretching direction and are several microns long. An AFM friction image and a corresponding topography image of SBS elongated by 30% are shown in Figure 8-3.

These two images show that the high friction regions (several hundred nanometers wide) can be correlated to depressions in the topography images that are only a few nanometers deep.
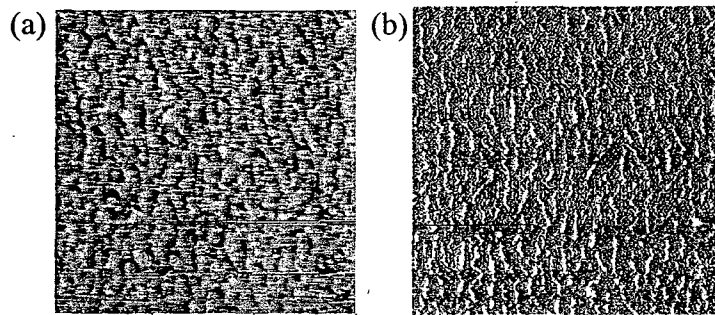
Figure 8-3: 30x30μm AFM (a) topography and (b) lateral force (friction) images taken from the SBS surface at 30% elongation

At higher elongation, the deformed regions propagate/expand and cover a higher fraction of the surface area. Figure 8-4a is a plot of the percentage of surface area covered by high friction regions as a function of elongation. The surface coverage was determined from image histograms generated from the lateral force images. When the SBS is elongated by 100% (when the length doubles), high friction areas cover roughly 35% of the total surface area. This indicates that the development of cracks accounts for most of the deformation in the surface.

The overall change in surface texture associated with the development of cracks can be characterized by the RMS roughness factor, defined in the previous chapter, which is extracted from the topography images. The relationship between the RMS roughness and elongation of the SBS sample is plotted in Figure 8-4b. The RMS roughness increases as the SBS is elongated, showing that the development and widening of

deformation zones leads to an increase in the overall surface roughness. Like the surface coverage age of high friction regions, the increase in surface roughness is approximately linear with elongation. Linear roughening behavior was also observed on elongated polyethylene – presented in the previous chapter. In that case, the roughening was associated with the deformation of micron size nodular structures at the surface.
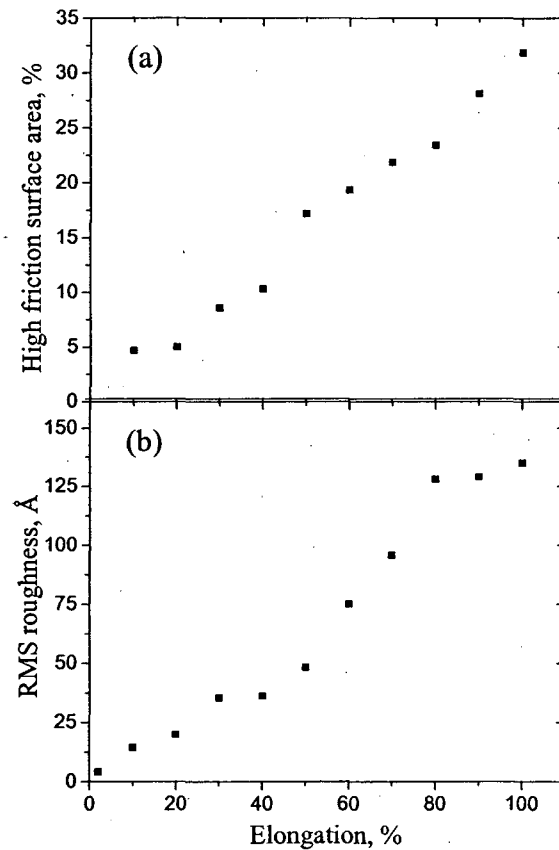
Figure 8-4: (a) Percentage of surface area covered by high friction regions as a function of elongation of the SBS sample (b) Plot of RMS surface roughness as a function of elongation of the SBS sample.

SFG spectra of SBS rubber as it is elongated SFG spectra of the SBS block copolymer as it is elongated, show that the $v2$ symmetric stretch associated with the

polystyrene blocks decreases in intensity. No other vibrational feature increases in intensity in the spectra. The decrease in intensity of the aromatic $v2$ mode could indicate that less surface area is covered by polystyrene when the SBS is elongated. As mentioned in Chapter 1, however, in addition to concentration the SFG signal intensity also depends on the ordering and on the orientation of the phenyl groups at the surface. Thus a decrease in intensity of the $v2$ mode could indicate that the phenyl groups are at the surface, but are no longer ordered at the interface, or that the phenyl groups are in an orientation at the surface that the SFG experiment is not sensitive to measuring (lying flat). Finally, a part of the overall decrease in the measured SFG signal is certainly due to the increased roughness of the surface – which tends to scatter the reflected SFG signal.
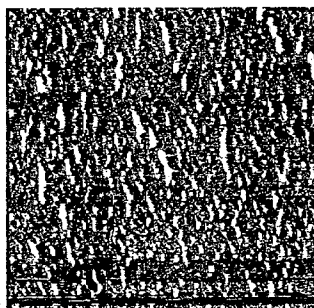
Figure 8-5: 30x30µm AFM lateral force (friction) images taken from the SBS surface after removal of strain. High friction cracks are still evident, indicating permanent deformation.

SBS surface after elongation An AFM friction image obtained from the SBS surface after allowing the polymer to relax from 100% elongation is shown in Figure 8-5. Several high friction deformation zones are still evident, but the width of the deformed regions has decreased. However, the overall surface coverage of cracks only reduces to

15%. This suggests that the deformed regions display a certain amount of elastic behavior. Because the deformation zones are still evident, though, shows that irreversible deformation was done to the polymer surface and that the surface composition and texture was irreversible altered by the stretching process.

SEBS Copolymer For comparative purposes, the surface of an ABA triblock polystyrene(ethylene-butylene)styrene copolymer (SEBS, Scientific Polymer, styrene content 30%, M.W. 90,000) was studied as it was elongated. In the SEBS copolymer, the ethylene-butylene block is more flexible than the polystyrene blocks and also has significantly lower surface tension than the polystyrene blocks.[18] In comparison to the SBS copolymer, the SEBS copolymer is more rigid than the SBS copolymer. SFG spectra of a SEBS copolymer film prior to elongation and during elongation (after the formation of a neck) are shown in Figure 8-6. The peak at $2850cm^{-1}$ can be assigned as the $CH_2(s)$ stretch, the peak at $2880cm^{-1}$ can be assigned as the $CH_3(s)$ stretch arising from the ethylene-butylene fraction of the copolymer. The SFG spectrum shows no evidence of the aromatic mode from the polystyrene segment at $3060cm^{-1}$. This result suggests that there is not a measurable quantity of ordered polystyrene at the surface and that the ethylene-butylene component, which has a lower surface tension than the styrene component, is the dominant component at the surface prior to elongation.

When the SEBS copolymer is elongated, the SFG spectra indicate that the ethylene-butylene component remains at the surface. No SFG signal is measured in the aromatic region suggesting that there is not a significant quantity of polystyrene ordered at the surface. Additionally, AFM images of the SEBS under elongation do not show localized deformation at the surface. This indicates that, in contrast to the SBS polymer,

163

which shows localized deformation, the ethylene-butylene component maintains a high surface coverage as the polymer is elongated and that the surface deformation is more uniform.
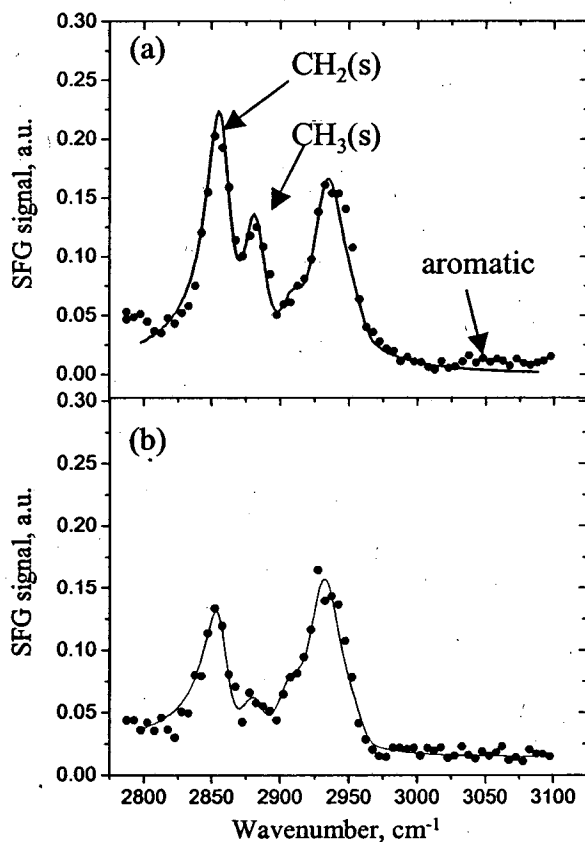
Figure 8-6: SFG spectra (ssp polarization combination) of SEBS film (a) prior to elongation and (b) at 100% elongation. There is no contribution from the polystyrene component, indicating that the flexible ethylene-butylene block covers the surface

8.4 Discussion

The results of these experiments show that the surface of *butadiene-rich* SBS copolymer does not deform homogeneously as it is elongated. At the surface, the strain is locally absorbed by zones that develop perpendicular to the stretching direction. The width of the deformation zones and the spacing between deformation zones is

inconsistent with the deformation of individual domains of polybutadiene or polystyrene. The width and spacing are more consistent with micron sized "grains" of organized styrene and butadiene domains.[19]

The deformed regions are spaced by several microns, a distance that contains several styrene domains, which are expected to be <50nm in diameter. Since the region between two cracks remains relatively undeformed at low elongation, parts of the polybutadiene matrix must also remain relatively undeformed. The deformed regions are 1-2 microns wide when the SBS is elongated by only 10%. Although the deformed regions are initially submicron in width – the deformation zone probably contains both components. Even though the deformed region probably contains both component, it is likely that most of the strain is absorbed by the rubbery polybutadiene matrix. Thus we suggest that the polybutadiene matrix exists in two states at the surface (1) relatively undeformed and (2) highly deformed.

The deformed regions display higher friction against the AFM tip. It is not clear why this is so. One possible explanation is that the freshly exposed material is simply tackier (stickier) than the material that has been exposed at the surface for several hours. However, AFM images collected several hours after deforming the SBS polymer still show the presence of high friction material. The higher friction may also be related to the orientation/microstructure of the material in the deformation zone. As mentioned in the previous chapter, highly oriented materials tend to have reduced modulus/stiffness in the direction perpendicular to the orientation. A reduced modulus may lead to relatively higher friction against the sliding of the AFM tip.

The surface roughness increases in an approximate linear fashion with elongation. This can easily be explained by the inhomogeneous nature of the deformation processes occurring at the surface. Typically, when a polymer is stretched in one direction, it contracts in the two perpendicular directions (the Poisson ratio). The deformed regions are highly elongated in the direction of the stress, and thus are compressed (sink) sink into the surface. Further expansion/propagation of the deformed regions increases this effect.

Michler has extensively studied the bulk and surface deformation of several grades of SBS copolymers.[8,9,20,21] In contrast to the SBS grade studied here which is butadiene rich, most of those were styrene rich and had a lamellar morphology. Mechanically, these grades of SBS are more rigid and behave similar to the SEBS copolymer described above. The most styrene-rich polymers initially deform by forming a neck region. For all of the samples studied by Michelieu, the butadiene-rich regions were shown to absorb most of the stress first, and expand at relatively low elongation (at or less than the 100% maximum elongation conditions used in these experiments). At the surface, this manifested itself as a widening of the interlamellar distance. Deformation/crazing of the polystyrene component was not observed until higher elongations.

Similar 'stretching' experiments were performed using segmented polyurethanes, comprised of much shorter rubbery and glassy chain segments than the SBS and SEBS copolymers.[1,2] The hard and soft segments phase separate, but on a much smaller length scale than the domains in the SBS or the SEBS copolymers. Those experiments showed that the surface was coated by the soft phase at prior to elongation. When the

polyurethanes were elongated, the soft segments expanded, exposing the underlying hard segments. In that polymer, the deformation was much more homogeneous, at least on a micron scale, and the polymers remained smooth at elongation up to 100%. The polyethylene samples presented in the previous chapter had micron-scale morphology and showed significant surface roughening as the microstructure deformed. Thus it is clear that the surface texture changes that occur when a polymer is elongated are intimately connected to the degree of phase separation, and to the microstructure of the block components.

The combination of data obtained from SBS, SEBS, and polyurethanes suggest that, in addition to changing the texture, stretching is capable of changing the surface composition of block copolymer. Stretching may provide a unique method for controlling the surface composition of a copolymer in an application. For example, a related study by Genzer takes advantage of the decrease in surface area of a polymer when it is contracted.[22] Hydrophobic chains can be grafted to PDMS surfaces while the PDMS is elongated, and when the PDMS contracts, the surface area decreases, leading to increased packing density of the hydrophobic chains. Similar scenarios can be envisioned were an active component is buried in the polymer bulk but is brought to the surface as a result of stretching.

8.5 Conclusion

The surface composition and morphology of a polystyrene(butadiene)styrene triblock copolymer has been studied by AFM and SFG as it is elongated. AFM friction and topography images indicate that when the copolymer is stretched, the deformation at the surface is highly localized by 'cracks', which become deeper and wider as the

polymer is elongated. The deformation zones likely contain highly deformed polybutadiene. The inhomogeneous deformation process leads to roughening of the surface.

References

[1] Amitay-Sadovsky, E.; Ward; B.; Somorjai, G.A.; Komvopoulos, K. *J. Appl. Phys.*, **2001**, *91*, 375.

[2] Amitay-Sadovsky, E.; Komvopoulos, K.; Tian, Y.; G.A. Somorjai, G.A. *Appl. Phys. Lett.*, **2002**, *80*, 1829-1831.

[3] McLean R.S.; Sauer, B.B. *J. Poly. Sci. B - Poly. Phys.*, **1999**, *37*, 859.

[4] Sauer, B.B.; McLean, R.S.; Brill, D.J.; Londono, D.J. *J. Poly. Sci. B – Poly. Phys.*, **2002**, *40*, 1727.

[5] Hild S. Gutmannsbauer W. Luth R. Fuhrmann J. Guntherodt HJ. *J. Poly. Sci. B – Poly. Phys.* **1996**, *34*, 1953.

[6] Opdahl, A.; Somorjai, G.A. *J. Poly. Sci. B- Poly. Phys.*, **2001**, *39*, 2263.

[7] Huy, T.A.; Adhikari, R.; Michler, G.H. *Polymer* **2003**, *44*, 1247.

[8] Godehardt, R.; Rudolph, S.; Lebek, W.; Goerlitz, S.; Adhikari, R.; Allert, E.; Giesemann, J.; Michler, G.H. *J. Mac. Sci. – Phys.* **1999**, *38*, 817.

[9] Adhikari, R.; Godehardt, R.; Lebek, W.; Weidisch, R.; Michler, G.H.; Knoll, K *J. Mac. Sci. – Phys.* **2001**, *40*, 833.

[10] van Djik, M.A.; van den Berg, R. *Macromolecules,* **1995**, *28*, 6773.

[11] Wei, X.; Hong, S.C.; Zhuang, X.W.; Goto, T.; Shen, Y.R. *Phys. Rev E* **2000**, *62*, 5160.

[12] Opdahl, A.; Somorjai, G.A. *Langmuir,* **2002**, *18*, 9409.

[13] Zhang, D.; Dougal, S.M.; Yeganeh, M.S. *Langmuir,* **2000**, *16*, 4528.

[14] Gautam, K.S.; Schwab, S.D.; Dhinojwala, A.; Zhang, D.; Dougal, S.M.; Yeganeh, M.S. *Phys. Rev. Lett.*, **2000**, *85*, 3854.

[15] Briggman, K.A.; Stephenson, J.C.; Wallace, W.E.; Richter, L.J. *J. Phys.Chem. B*; **2001**, *105*, 2785.

[16] Oh-e, M.; Hong, S.C.; Shen, Y.R. *Appl. Phys. Lett.*, **2002**, *80*, 784.

[17] The ratio of the aromatic modes that have different symmetry has previously been used to qualitatively show changes in orientation of the phenyl group. The ratio of the $v2(3060cm^{-1})$ and $v20(3025cm^{-1})$ modes is similar for the SBS sample and polystyrene homopolymer films, indicating that there is no measurable change in orientation of the phenyl groups contributing to the SFG signal.

[18] We do not know the percentage of butylene in the ethylene-butylene block of the SEBS copolymer. However, the surface tension of polyethylene and polybutylene homopolymers are 35N/m and 31N/m respectively (*Polymer Handbook*, Brandup et al.) and are both lower than the surface tension of polystyrene 38N/m.

[19] Pakula, T; Saijo, K; Kawai, H; Hasimoto, T. *Macromolecules,* **1985**, *18*, 1294.

[20] Michler, G. *J. Mac. Sci. – Phys* , **1999**, *38*, 787.

[21] Huy, T.A.; Hai, L.H.; Adhikari, R.; Weidisch, R.; Michler, G.H.; Knoll, K. *Polymer* **2003**, *44*, 1237.

[22] Genzer, J.; Efimenko, K. *Science*, **2000**, *290*, 2130.

Chapter 9

Surface mechanical properties of pHEMA contact lenses: Viscoelastic and adhesive changes on exposure to controlled humidity

9.1 Introduction

Hydrogel soft contact lenses have been used for vision correction for over 30 years. In spite of the many advances that have been made to improve the comfort and biocompatibility of contact lenses, the interfacial properties of contact lenses are not well understood. An example is the hydration state of the surface region of a contact lens.[1] It is commonly observed that the bulk water content affects both the oxygen permeability and the mechanical properties of the lens – and consequently affects the overall comfort of the lens.[2] At the contact lens surface, it is believed that a high water content and high surface hydrophilicity are desirable properties, in order to increase the wettability of tear films.[3] Many strategies have been developed to increase surface hydrophilicity,[2] however, measurements of the water content of the

surface region have not been made and the concentration of water at the surface, relative to the bulk water content, is uncertain.

The surface water content is particularly important for understanding comfort of poly(hydroxyethyl)methacrylate (pHEMA) based contact lenses, where oxygen permeability increases as the bulk water content increases.[2] These types of lenses tend to dehydrate when they are on the eye,[4] and if the water content at the contact lens/air interface is significantly less than the bulk water content due to dehydration, then oxygen diffusion may be limited at the interface. The water content of the near-surface region also affects the surface mechanical properties, including the viscoelastic and friction properties, of pHEMA, which is rigid and glassy in its dry state but is soft and flexible in its fully hydrated state.

This chapter presents a method for characterizing the surface water content of pHEMA contact lenses, by measuring changes in the surface mechanical properties as a function of humidity, at the air/contact lens interface. Atomic force microscopy (AFM) is used to probe the surface adhesive and viscoelastic properties to a depth of up to 150nm - using the experimental setup shown in Figure 9-1. Air exposed surfaces of pHEMA lenses under ambient humidity are shown to be dry and rigid, relative to the bulk material. The balance between the rate of dehydration from the lens and the rate that water diffuses to the interface from the contact lens bulk is shown to control the thickness of the dehydrated interfacial region. As the relative humidity of the air increases, the rate of dehydration from the contact lens decreases, leading to higher water content and softer mechanical properties in the near surface region.

9.2 Experimental Procedures

Poly(hydroxethyl)methacrylate based contact lens

The commercial hydrogel contact lenses used in this study were made of a homopolymer of 2-hydroxyethyl methacrylate, pHEMA, (Polymacon[TM], Ocular Sciences, FDA Group-I) and were crosslinked using ethylene glycol dimethacrylate as the crosslinking agent. The lenses were polymerized in a polypropylene mold. When swollen in saline solution (0.15M NaCl, buffered at pH=7), the pHEMA lens contains 38% water (wt/wt). The lenses received no further surface treatment and were thoroughly washed with fresh saline solution prior to AFM measurements.

Atomic Force Microscopy (AFM)

The AFM experimental setup is shown in Figure 9-1 and is designed to mimic, as closely as possible, an ocular environment.[5] The homebuilt walking-style AFM scanning head, controlled by RHK electronics, has been previously described and is enclosed within a 30L glass bell jar.[6] The contact lens is supported on a polypropylene mold, immersed in saline solution, and covered by a stainless steel cover plate. The cover plate was machined to have an inside curvature of 8.6 mm and an outside orifice diameter of 4mm. The inside curvature secured the contact lens without distortion and the outside orifice allowed AFM measurements of the contact lens surface exposed to air.

The air-exposed surface region of the contact lens reaches a steady-state condition, where water evaporation from the lens surface is equilibrated with water replenishment by diffusion from the bulk. In subsequent discussion, this type of lens

172

is referred to as "bulk hydrated". For comparative purposes, AFM experiments were also performed on dehydrated contact lenses – where there is no saline solution in the reservoir. For these experiments, the contact lens was placed on a polypropylene mold and allowed to dry overnight under ambient conditions prior to AFM measurement. This type of lens is referred to as "bulk dehydrated".
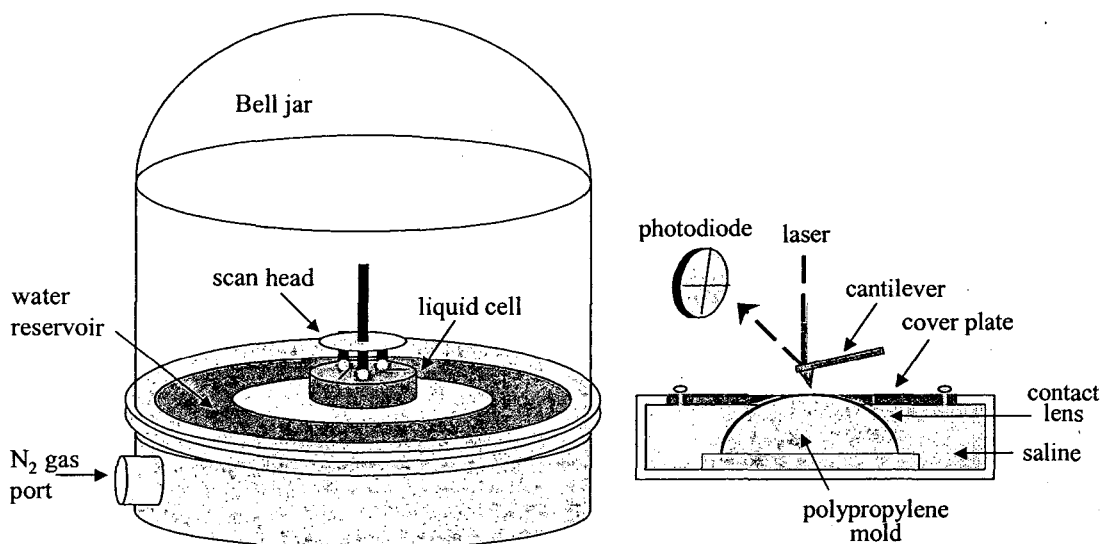
Figure 9-1: (a) Schematic view of the AFM instrument used to measure the surface mechanical properties of bulk-hydrated and bulk-dehydrated soft contact lenses. Relative humidity inside the bell jar increases as water evaporates from the reservoir and is maintained by adjusting the flow rate of low-humidity nitrogen gas through the bell jar. (b) Close-up view of sample stage showing polypropylene contact lens holder, saline reservoir, and stainless steel cover plate.

Relative humidity was controlled by competition between the evaporation of water from a secondary reservoir in the bell jar and the flow of low humidity nitrogen gas through the bell jar. After adjusting the humidity, the contact lenses were allowed to stabilize for 30 minutes prior to AFM measurement. Measurements were performed using silicon nitride cantilevers (ND-MDT) with a force constant of 1N/m.

Force vs. distance (f-d) curves were obtained by recording the normal deflection signal of the cantilever during the tip approach (loading) and retraction (unloading). The detector signal was calibrated by adjusting the slope of the f-d curve measured against a reference surface to the nominal spring constant of the cantilever. A hydrophilic glass surface was used as a reference and was prepared by treating a glass slide with Piranha solution (9 parts of conc. H_2SO_4 and 1 part of 30% H_2O_2).

Typical force (load) vs. distance curves are shown in Figure 9-2 and measure the dependence of the AFM cantilever bending on the motion of the piezoelectric actuator. The force vs. distance curve contains information related to the elastic, viscous, and adhesive properties of the contact lens surface. As the piezoelectric actuator presses the AFM tip against the contact lens surface, there are three major deformation components: bending of the cantilever (the load), elastic strain of the contact lens, and viscous strain of the contact lens. When the cantilever is initially retracted from the surface, the viscous strain component is minimized and the primary deformation components are recovery of the cantilever bending and elastic recovery of the contact lens. Thus the difference between the loading and unloading curves qualitatively reflects the magnitude of the viscous strain component.
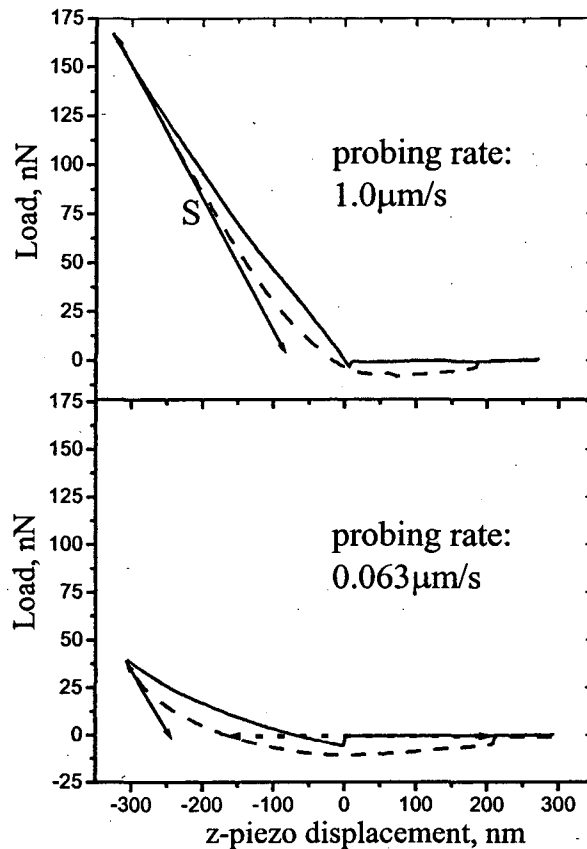
Figure 9-2: Comparison of AFM force vs. distance curves collected at 0.063μm/s and 10μm/s probing rates on the bulk-hydrated pHEMA contact lens (75% relative humidity). The solid line is the approach (loading) curve, the dashed line is the retraction (unloading) curve, and the solid arrow represents the best-fit slope of the initial part of the retraction curve (the stiffness).

The stiffness, S, is defined here as the initial slope of the unloading curve and contains all of the elastic deformation information (from both the cantilever and the contact lens recovery).[7] If a contact model is assumed, then the elastic modulus can

be estimated from the stiffness value. In this paper, we have used the Hertz model as a first approximation to describe the contact area in our calculation of elastic modulus.[7] Since this type of contact model neglects adhesive effects and underestimates the true contact area, the elastic modulus values reported are overestimates of the true values and are presented only to show the approximate magnitude of the surface elastic modulus. Additional details of the procedure used for transforming stiffness values into elastic modulus can be found in reference 8.

The measurement of the viscous component has a strong time dependence associated with it, whereas the contact lens elastic strain and cantilever bending have little or no time dependence.[9] The contribution of the viscous strain component to the deformation process can be assessed as a function of piezoelectric actuator driving rates. Force vs. distance curves were collected at actuator drive rates from 0.06μm/s to 20μm/s. The two force curves in Figure 9-2 were collected at actuator rates of 0.06μm/s and 10μm/s and highlight the time dependence of the viscous strain component. The loading curve collected at 0.06μm/s reaches a lower maximum load than the curve collected at 10μm/s, indicating that the cantilever bends less and the tip sinks deeper into the surface under slow probing rates. Collecting force curves at faster and faster rates decreases the magnitude of the viscous component in the deformation process, until it is not detectable in the force vs. distance measurement.

9.3 Results

Stiffness and Elasticity as a function of humidity

Loading and unloading slopes extracted from the force vs. distance curves of

the bulk-hydrated and bulk-dehydrated contact lenses at probing rates between

$0.06\mu m/s$ to $20\mu m/s$ are shown in Figures 9-3a and 9-3b, respectively. The average

stiffness, S, as a function of humidity for the bulk-hydrated lens and the bulk-

dehydrated lens is presented in Table 9-1. The corresponding elastic modulus values

calculated from the stiffness values are also presented in Table 9-1. A stiffness value

of 1N/m represents the highest value that can be measured with the 1N/m cantilever

used in the experiments and indicates that the contact lens surface was not

measurably deformed. A stiffness value of zero reflects complete compliance of the

contact lens (no cantilever bending). Using the procedure outlined in reference 8,

these stiffness limits of the 1N/m cantilever translate into a sensitivity range of elastic

modulus values that are between 10 and 70MPa.

The stiffness is independent of the measurement rate for both bulk-hydrated

and bulk-dehydrated contact lenses. Additionally, the stiffness of the bulk-dehydrated

lens remains relatively constant as the humidity is increased. Since the stiffness

values of the bulk-dehydrated lens saturate the scale at ~1N/m, the calculated

minimum surface elastic modulus is at least 70MPa. The elastic modulus is likely

much greater than this and is probably similar to the bulk value obtained from dry

pHEMA, ~1Gpa, suggesting that the surface of bulk-dehydrated pHEMA exposed to

moderate humidity is in a glassy state.
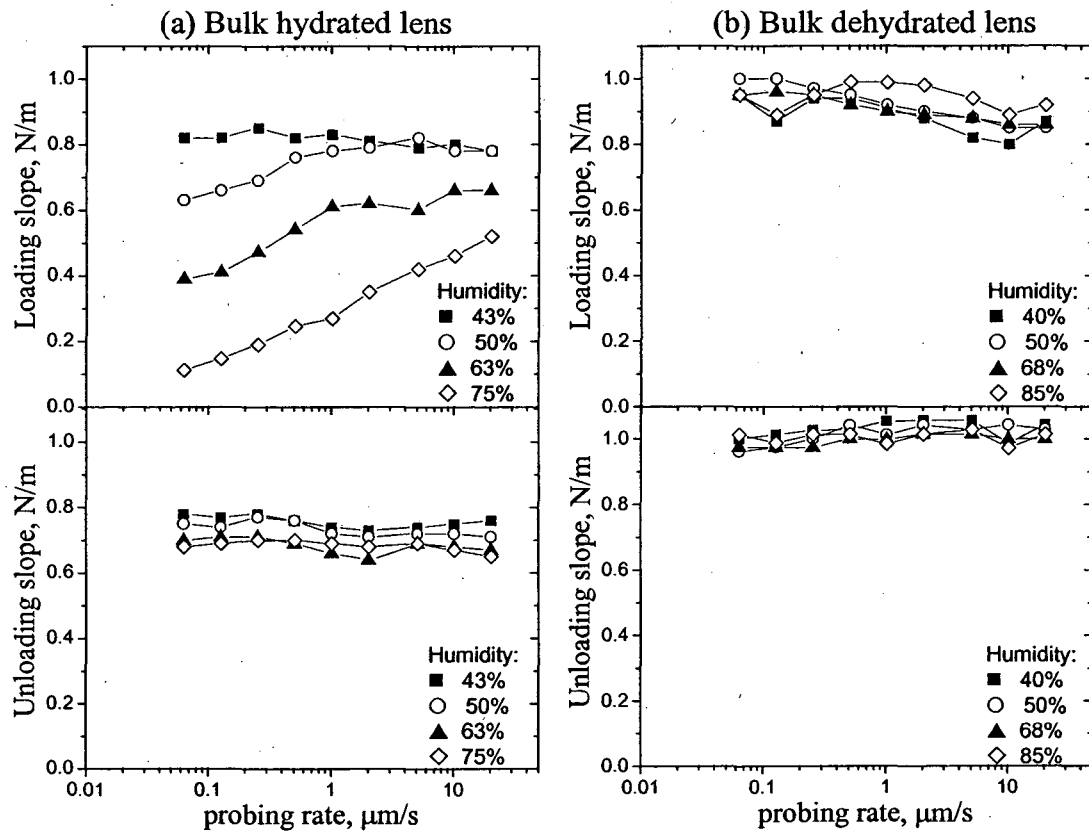
Figure 9-3: Comparison of the loading curve slopes and unloading curve slopes for the bulk-hydrated lens and the bulk dehydrated lens collected at various probing rates and humidity (1N/m cantilever). The loading curve slope contains contributions from both elastic and viscous deformations while the unloading curve slope contains mainly elastic contributions. The loading curve slope of the bulk-hydrated decreases and has a strong dependence on probing rate at high humidity, indicating an increased presence of water in the surface region.

Bulk hydrated lens (bulk mod. 0.3MPa)			Bulk dehydrated lens (bulk mod. 1 GPa)		
Rel. humidity	Surface stiffness N/m	Surface elastic modulus, MPa	Rel. humidity	Surface stiffness N/m	Surface elastic modulus, MPa
43%	0.76±0.02	45±7	40%	1.03±0.02	>70
50%	0.73±0.02	35±7	50%	1.02±0.03	>70
63%	0.68±0.03	25±7	68%	0.99±0.02	>70
75%	0.68±0.02	25±7	85%	1.01±0.02	>70

Table 9-1: Average stiffness (S) and elastic modulus values at various relative humidity values measured for bulk hydrated and dehydrated lenses. A stiffness value of 1N/m represents the limiting value that can be measured with a 1N/m cantilever.

In contrast, the stiffness of the bulk-hydrated lens at 45% relative humidity is measurably lower than the stiffness of the bulk-dehydrated lens at 45% relative humidity. At low relative humidity, 45%, the surface stiffness is 0.76N/m, and the calculated surface elastic modulus is 45MPa, intermediate to the elastic modulus of totally dehydrated pHEMA and totally hydrated pHEMA. This indicates that at low humidity, dehydration from the surface is still a significant factor and that the air exposed surface is stiffer that the bulk of the contact lens.

As the humidity increases, there is a slight decrease in the stiffness of the surface. At 75% relative humidity, the stiffness decreases to 0.68N/m, which corresponds to an elastic modulus of 25MPa. This behavior is consistent with an increase in the water content at the surface, which softens the lens. At room temperature dry pHEMA is below its glass transition temperature, 50-80°C,[10] and is in a mechanically rigid state. Water acts as a solvent and plasticizes the surface of the

contact lens. Even though the surface softens as the humidity increases, it is still much stiffer than the surface of the totally hydrated contact lens, which has been measured by AFM to have a value ~ 1.3MPa.[5] This indicates that even at high humidity, the dehydration rate of the interface is sufficient to affect the mechanical properties of the contact lens surface.

Viscous behavior as a function of humidity

The viscous behavior of the bulk-hydrated lens surface, qualitatively assessed from the slopes of the loading curves presented in Figure 9-3, also suggests that the concentration of water in the near surface region increases as the humidity increases. A smaller value of the loading curve slope, and larger differences between the slopes of the loading and unloading curves at a particular probing rate, indicate larger viscous effects.

The loading curve slope is extremely sensitive to changes in humidity. At 45% humidity, there is no measurable difference between the loading slope and the unloading slopes, indicating little viscous deformation of the surface. When the relative humidity is increased above 60%, the magnitude of the viscous deformation increases. The AFM tip sinks farther into the surface to reach a given load. This effect is most noticeable at the slower probing rates, which give the contact lens more time to relax, and are more sensitive to the viscous deformation component. The increased viscous behavior indicates that the near surface region retains more water at high humidity and is consistent with the stiffness measurement, which showed that the surface region softens at high humidity.

In contrast, the loading and unloading slopes presented in Figure 9-3 are very similar for the bulk dehydrated lens, indicating that the dehydrated lens undergoes little viscous deformation as a function of humidity. This is consistent with the data for the elastic behavior of the dehydrated lens, which showed that the dehydrated lens remained rigid as the humidity increased. The combination of elastic and viscous data are a strong indication that very little water is present at the surface of the bulk-dehydrated lens, even at high humidity.

It is noted that a detailed calculation of the surface viscosity is not possible using the type of data presented in this paper. In a typical viscosity measurement, the material is held under a fixed loading rate or a fixed strain rate. The AFM force vs. distance measurement is neither a fixed load nor a fixed strain experiment. Although the piezoelectric actuator moves at a fixed rate, the material strain rate varies throughout the experiment.

Adhesive behavior as a function of humidity

When the cantilever retracts from the surface, there is an adhesive interaction between the AFM tip and the contact lens. Figure 9-4a and 9-4b show plots of the adhesive snap-out interaction distances as a function of humidity for the bulk dehydrated and bulk hydrated lenses, collected at a probing rate of 5μm/s. For force curves collected at slower rates, the snap-out adhesion values are larger, for faster rates they are lower. The same behavior is observed for the adhesive jump to contact force on the loading curve, and is consistent with the work done by Basire et al. on styrene-butadiene copolymers showing that, for soft viscoelastic materials, snap-in adhesive interactions increase as function of measurement time.[11]
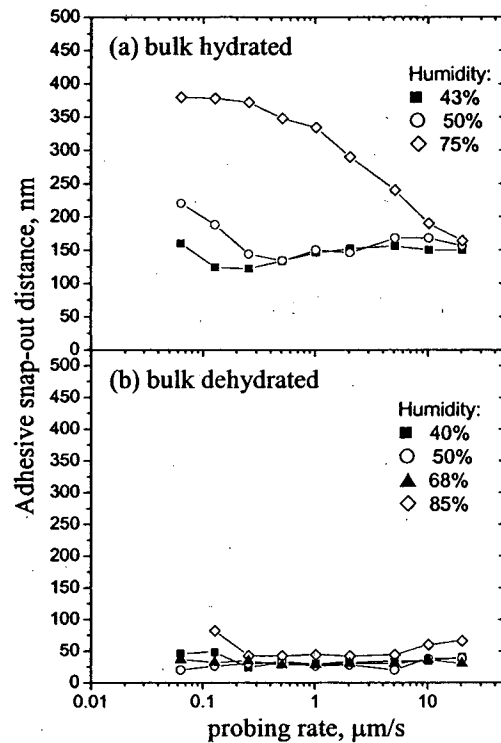
Figure 9-4: Adhesive snap out distance vs. loading rate for: (a) bulk-hydrated and (b) bulk-dehydrated contact lenses. The snap-out distances measured on the bulk dehydrated lens are small for all humidity values and probing rates. The snap out distances increases as humidity increases for the bulk hydrated lens.

The adhesive interactions have no measurable dependence on humidity for the bulk-dehydrated lens. However, the snap-out adhesive interactions increase in magnitude as the humidity increases for the bulk-hydrated lens. As the lens becomes softer at high humidity, the tip probes deeper into the surface and there may be an enlarged contact area between the tip and the lens. Additionally, the AFM tip may be

pulling material out from the surface as it retracts.[12] That the adhesive properties of the bulk-dehydrated lens show no humidity dependence confirm that there is very little water in the surface region. It also indicates that there is not a layer of water condensing at the surface of the bulk-dehydrated lens at high humidity – which would lead humidity dependent adhesive behavior due to capillary interactions between the AFM tip and the adsorbed water.

9.4 Discussion

The adhesive and viscoelastic properties reported here suggest that the surface mechanical properties and surface water content of pHEMA contact lenses are strongly dependent on the bulk hydration state and on the relative humidity of the environment. The surface region of a bulk-dehydrated contact lens remains stiff and dry at all values of humidity measured in these experiments. The surface region of a bulk-hydrated contact lens is dry under ambient humidity, but becomes softer and contains more water as the humidity is increased – due to a decrease in the rate of dehydration.

Figure 9-5 presents the humidity dependences of the surface viscoelasticity for the bulk hydrated and bulk dehydrated lenses. This plot shows the minimum rate that the AFM loading curves need to be collected at in order to be insensitive to viscous strain effects as a function of humidity. The "minimum actuator rate" is taken as the rate at which the loading curve slope no longer increases - where there is no apparent viscous deformation of the lens surface. For the bulk dehydrated lens, the surface viscoelastic behavior has no measurable dependence on humidity. In order to be sensitive to possible changes in surface viscoelasticity of the dehydrated lens, force

curves would need to be collected at much slower rates or the temperature of the sample would need to be raised.
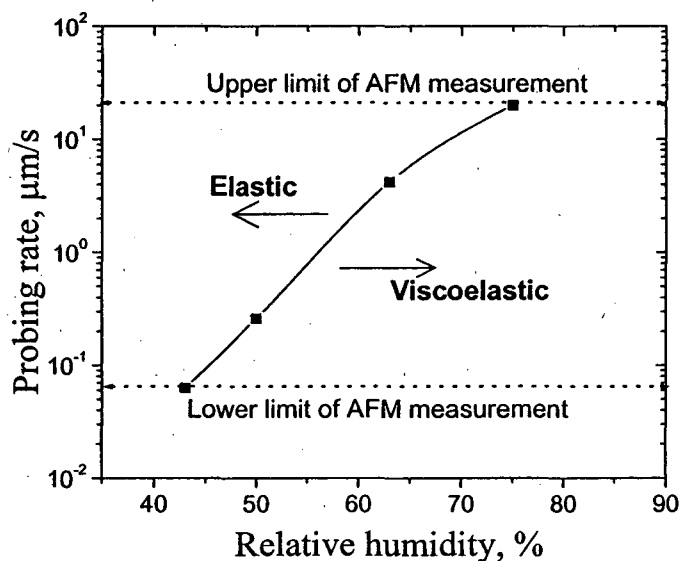
Figure 9-5: Plot of the minimum probing rate needed to remove viscous strain effects from the force curves of the bulk hydrated (▲) and bulk dehydrated (△) lenses as a function of humidity. The results indicate that the surfaces of bulk dehydrated lenses are rigid at all measured humidity values and that the surfaces of bulk hydrated lenses are rigid at ambient humidity but soften when the humidity increases above ~60%.

The stiff surface region measured at all humidities is consistent with water absorption measurements made on pHEMA as a function of humidity, which suggest that although increasing the humidity of the air increases the bulk water content, the largest increases in absorbed water occur do not occur until the relative humidity is above 80-90%.[13]

For the bulk-hydrated lens, at low relative humidity, the surface behaves much like the bulk-dehydrated lens. As the humidity increases, however, the AFM measurement must probe the surface faster and faster in order to be insensitive to the viscous relaxation of the bulk-hydrated lens surface. The greatest change in the viscous behavior is measured between 60% and 85% relative humidity. This suggests that a decreased rate of dehydration increases the water content of the surface region and softens the pHEMA surface.

From a practical standpoint, these results indicate that the air-exposed surfaces of contact lenses are likely to be quite dry and rigid, and are also stiffer than the bulk material. The increased stiffness may affect the interaction between the contact lens and the eyelid and may affect the overall lens movement on the eye. It should be noted that these experiments do not take into account important biological factors such as the presence protein material at the surface, which have been shown to change the wettability of the surface,[14] or the presence of rewetting tear films. In spite of this, dehydration from the lens has been shown to be a significant factor in controlling the mechanical properties of the surface region of the lens.

9.5 Conclusion

Changes in the surface viscoelastic and adhesive properties of bulk hydrated and dehydrated pHEMA-based contact lenses were monitored as a function of humidity by atomic force microscopy (AFM). Stiffness, elastic modulus, viscous deformation, and adhesion properties were extracted from AFM force vs. distance interaction curves and indicate that the surfaces of bulk-dehydrated lenses are dry at humidities up to 85% and that there is very little net diffusion of water into the bulk.

For the bulk-hydrated lens, the surfaces are rigid and dry under ambient humidity and soften dramatically at ~60% relative humidity, indicating an increased presence of water, which plasticizes the surface layer. This method can be used to compare surface water content of various classes of hydrogel and to test the effectiveness of various surface treatments hydrogel material in enhancing the water content of the surface region.

References

[1] McConville, P.; and Pope, J.M. *Polymer*, **2001**, *42*, 3559.

[2] Lai, Y.C.; and Friends, G.D. *J. Biomed Mat Res*, **1997**, *35*, 349.

[3] Lopez-Alemany, A.; Compan, V.; and Refojo, M.F. *J. Biomed Mat Res (Appl Biomater)*, **2002**, *63*, 319.

[4] Pritchard, N.; and Fonn, D. *Opthal. Physiol. Opt.*, **1995**, *15*, 281.

[5] Kim, S.H.; Marmo, C; and Somorjai, G.A. *Biomaterials*, **2001**, *22*, 3285, and Kim, S.H.; Opdahl, A.; Marmo, C; and Somorjai, G.A. *Biomaterials*, **2002**, *23*, 1657.

[6] Gracias, D.H; Zhang, D.; Lianos, L.; Ibach, W.; Shen, Y.R.; and Somorjai, G.A. *Chemical Physics*, **1999**, *245*, 277.

[7] Pharr, G.M.; and Oliver, W.C. *MRS Bulletin*, **1992**, *17*, 28.

[8] Opdahl A.; and Somorjai, G.A. *J. Polymer Science B-Polymer Physics*, **2001**, *39*, 2263.

[9] Ferry, J.D. *Viscoelastic properties of polymers*, 3rd edition, New York, Wiley, **1980**.

[10] Peyser, P. in *Polymer Handbook*, ed. by J. Brandup, Wiley, New York, **1989**.

[11] Basire, C.; and Fretigny, C. *Tribology Letters*, **2001**, *10*, 189.

[12] Bliznyuk, V.N.; Assender, H.E.; and Briggs, G.A.D. *Macromolecules*, **2002**, *35*, 6613.

[13] Refojo, M.F. in *Hydrogels for Medical and Related Applications*, ed. by Robert. F. Gould, American Chemical Society, **1976**, 37-51.

[14] Holly, F.J.; and Refojo, M.F. in *Hydrogels for Medical and Related Applications*, ed. by Robert. F. Gould, American Chemical Society, **1976**, 267-282.

ERNEST ORLANDO LAWRENCE BERKELEY NATIONAL LABORATORY
ONE CYCLOTRON ROAD ｜ BERKELEY, CALIFORNIA 94720